

The Pennsylvania State University

The Graduate School

College of Engineering

**AN INVESTIGATION INTO THE TEMPERATURE EFFECT ON THE
PERFORMANCE OF ULTRASONIC TRANSDUCERS FOR HIGH
TEMPERATURE AND HARSH ENVIRONMENT APPLICATIONS**

A Thesis in

Engineering Science and Mechanics

by

Andrew D. Suprock

©2016 Andrew D. Suprock

Submitted in Partial Fulfillment
of the Requirements
for the Degree of

Master of Science

December 2016

The thesis of Andrew Suprock was reviewed and approved* by the following:

Bernhard R. Tittmann
Schell Professor and Professor of Engineering Science and Mechanics
Head of Engineering Nanostructure Characterization Center
Thesis Advisor

Clifford J. Lissenden III
Professor of Engineering Science and Mechanics

Albert E. Segall
Professor of Engineering Science and Mechanics

Judith A. Todd
Professor of Engineering Science and Mechanics
Head of the Department of Engineering Science and Mechanics

*Signatures on file in the Graduate School

Abstract

Transducer technology is an in-demand resource particularly in the fields of ultrasonic non-destructive evaluation (UNDE), structural health monitoring (SHM), and biomedical ultrasound. For years, transducers have been used to characterize various types of materials, ranging from metals to composites (interwoven conglomeration of various materials) and even organics as well as to establish the integrity of structural components such as bridge struts, subterranean pipelines, and vehicle bodies. Transducers can even be used to find defects, cracks, delaminations, etc on the micro- and nano-scales. Most of these processes occur at room temperature or only slightly elevated temperatures (<100 °C). This means that the physical components have little to fear from the stress and strain of thermal expansion as well as the process of oxidation. However, when higher temperature (>400 °C) capabilities are necessary, only a select few piezoelectric materials can make the cut. The piezoelectric material must be combined with the right components from the casing, to the waveguide, to the coupling, to the matching layer, as well as the backing material and work together cohesively with a lead wire to produce the most consistent and cleanest acoustic signals and data possible for their particular application.

The objective of this thesis is to investigate the influence of the temperature effect on ultrasonic transducers based on a comparison of the effects of high temperature conditions versus those of high temperature and irradiation on the transducer system. There will also be a preliminary move towards the establishment of the means for optimizing the bulk single crystal transducer fabrication process in order to achieve peak efficiency and maximum effectiveness in both irradiated and non-irradiated high temperature applications. Optimization of the material components within the transducer will greatly increase non-destructive testing abilities for industry, structural health monitoring, and so much more.

The following research involves testing several different piezoelectric materials under high temperature conditions. The viability of aluminum nitride (AlN) as a transducer material in high temperature conditions has been previously explored [1] (Parks, et al, 2010) and shall be further tested to ensure reliability. Zinc oxide (ZnO) and bismuth titanate (BiT) will also be explored as they have shown promising results in the past. Data collected from the ULtrasonic TRAnsducers (ULTRA) project will also be compared to the high temperature data since the construction of the transducer was the same. A preliminary search of various combinations of

transducer material components (waveguide and backing materials in order to find the best match for a given piezoelectric material) will be conducted to find the best combination of these components for steady and strong acoustic transmission.

Contents

List of Figures	vii
List of Tables	xi
Acknowledgements	xiii
1 Introduction	1
1.1 Piezoelectric Effect	1
1.1.1 Piezoelectric Materials	3
1.1.2 Crystal Structures	4
1.2 Background and Motivation	6
1.2.1 Non-Destructive Testing versus Structural Health Monitoring	6
1.2.2 Bulk Single Crystal Transducer	8
1.2.3 Fabrication Process	10
1.2.4 High Temperature Environment	17
1.2.5 Irradiation	18
1.3 Literature Review	19
1.3.1 Materials Properties and Reactions	19
1.3.1.1 Aluminum Nitride	20
1.3.1.2 Bismuth Titanate	23
1.3.1.2.1 BiT, Sodium-modified BiT, & BNT	24
1.3.1.3 Stainless Steel (304 and 316)	25
1.3.1.4 Kovar	26
1.3.1.5 Carbon-Carbon Composite	26
1.3.2 Gold-Aluminum Boundary Interactions	28
1.4 Dissertation Scope	29
2 High Temperature Endurance Runs	30
2.1 Bismuth Titanate (Sodium-modified)	34
2.2 Aluminum Nitride	47
2.2.1 HT-series Aluminum Nitride High Temperature Viability Studies	57
2.3 Analysis/Conclusions	68
2.3.1 Bismuth Titanate Analysis	68
2.3.2 Aluminum Nitride Analysis	70

3	High Temperature Effects and Irradiation Effects Comparison	72
	3.1 High Temperature Endurance Testing Results	72
	3.2 ULTRA Irradiation Results	74
	3.3 Comparison/Conclusions	82
4	Future Work	83
	4.1 Materials Optimization	83
	4.2 Zinc Oxide Testing	89
	4.3 More Inert Environment Testing	91
5	Conclusion	91
	References	94
	Bibliography	97

List of Figures

Figure #1.1: Illustration of the factors that affect the direct piezoelectric effect, displaying the force-charge and force-voltage equations	3
Figure #1.2: Breakdown of the thirty-two crystal structure classes based on symmetry, piezoelectricity, pyroelectricity, and ferroelectricity	5
Figure #1.3: The effect of polarization in an applied electric field	6
Figure #1.4: The Van Dyke model of an equivalent circuit for the bulk single crystal transducer	9
Figure #1.5: Two separate disassembled transducer constructions with components laid out in a sequential order	12
Figure #1.6: Disassembled components of the bulk single crystal transducer assembly (from left to right) 304 stainless steel cap, nickel plunger with alumina insulation, carbon-carbon backing material, gold foil coupling, alumina insulation, aluminum nitride piezoelectric element, gold foil coupling, kovar waveguide, iron-nickel-cobalt alloy spring, 316 stainless steel casing	14
Figure #1.7: Computational model of the bulk single crystal transducer assembly	15
Figure #1.8: Rendering of the schematics sent to the machine shop	16
Figure #1.9: Fully constructed bulk single crystal transducer assembly connected to the mineral-insulated thermocoax lead wire and stabilized by the strain relief gauge	16
Figure #1.10: Close-up of the fully constructed bulk single crystal transducer assembly, illustrating the connection between the lead and the plunger	17
Figure #1.11: Microscope image of HT-2412 aluminum nitride crystal	21
Figure #1.12: Microscope image of HT-2572 aluminum nitride crystal	22
Figure #2.1: Thermolyne 21100 tube furnace used for high temperature endurance runs	31
Figure #2.2: Olympus Panametrics-NDT Model 5800 Computer Controlled Pulser-Receiver used to power the transducer	32
Figure #2.3: Example of settings used for spray-on transducers on the Olympus Panametrics-NDT Model 5800 Computer Controlled Pulser-Receiver	32
Figure #2.4: Example of settings used for single crystal transducers on the Olympus Panametrics-NDT Model 5800 Computer Controlled Pulser-Receiver	33
Figure #2.5: Monitor connected to the National Instruments NI PXI-1042Q system	33

Figure #2.6: The National Instruments NI PXI-1042Q system, with NI PXI-5122 14-bit 100 MS/s Digitizer oscilloscope card and LabView software installed, used to take acoustic data during high temperature endurance run	34
Figure #2.7: The connections made to the K15 bismuth titanate transducer for high temperature endurance and performance analysis	35
Figure #2.8: Analyzed segment of the initial pulse-echo signal amplitude response of the sodium-modified bismuth titanate transducer at room temperature	36
Figure #2.9: Plot of the FFT analysis of the initial K15 transducer signal with an arrival time of 2.7 μs within a 25 μs window length	37
Figure #2.10: Plot of the FFT analysis of the initial K15 transducer signal with an arrival time of 2.6 μs within a 25 μs window length	38
Figure #2.11: Graph of segment 1 maximum raw amplitude data (blue) and temperature (green) versus time	39
Figure #2.12: Graph of segment 1 maximum relative amplitude (blue) and temperature (green) versus time	40
Figure #2.13: Graph of segment 2 maximum raw amplitude (blue) and temperature (green) versus time	41
Figure #2.14: Graph of segment 2 maximum relative amplitude (blue) and temperature (green) versus time	42
Figure #2.15: Graph of segment 3 maximum raw amplitude (blue) and temperature (green) versus time	43
Figure #2.16: Graph of segment 3 maximum relative amplitude (blue) and temperature (green) versus time	44
Figure #2.17: Full high temperature endurance test of the K15 transducer, graphing raw amplitude (blue) and temperature (green) over time	45
Figure #2.18: Full high temperature endurance test of the K15 transducer, graphing relative amplitude (blue) and temperature (green) over time	46
Figure #2.19: Oscilloscope display showing pulse-echo amplitude signal from the aluminum nitride transducer prior to endurance testing	48
Figure #2.20: Analyzed segment of the initial pulse-echo amplitude response of the aluminum nitride transducer at room temperature	49

Figure #2.21: Plot of the resonance peak from the FFT analysis of the initial aluminum nitride transducer signal	50
Figure #2.22: Full high temperature endurance test of the aluminum nitride transducer, graphing maximum amplitude (blue) and temperature (green) versus time	51
Figure #2.23: Full high temperature endurance test of the aluminum nitride transducer, graphing maximum relative amplitude (blue) and temperature (green) versus time	52
Figure #2.24: SEM image of the aluminum nitride sample at 2000x magnification	53
Figure #2.25: SEM image of the aluminum nitride sample at 500x magnification	54
Figure #2.26: Example of a poorly triggered signal from the initial signal degradation in the aluminum nitride endurance test	55
Figure #2.27: Oscilloscope display of a poorly triggered aluminum nitride transducer signal	56
Figure #2.28: Displaying breakdown of carbon-carbon backing after long term high temperature exposure	57
Figure #2.29: APC International YE2730A Piezo d_{33} meter with test piece	58
Figure #2.30: Power supply and display for APC International YE2730A Piezo d_{33} meter	58
Figure #2.31: HT wafers in their pre-cut, pre-heat treatment form, (top) HT-2902, (bottom left) HT-2572, (bottom right) HT-2412	59
Figure #2.32: SEM image of non-heat treated HT-2902 at 2000x magnification	62
Figure #2.33: SEM image of non-heat treated HT-2902 at 500x magnification	63
Figure #2.34: SEM image of heat treated HT-2902 at 2000x magnification	64
Figure #2.35: SEM image of heat treated HT-2902 at 500x magnification	65
Figure #2.36: EDS graph of heat treated HT-2902	65
Figure #2.37: EDS graph of non-heat treated HT-2902	65
Figure #2.38: Comparison of EDS graphs of HT-2902 (non-heat treated: red; heat treated: blue)	66
Figure #2.39: HT samples post heat treatment; (from left) HT-2412, HT-2572, HT-2902	67
Figure #2.40: Plot of the resonance peak from the FFT analysis of the final signal received from the K15 transducer	69
Figure 2.41: Plot of the resonance peak from the FFT analysis of the final signal received from the aluminum nitride transducer	71

Figure #3.1: Plot of maximum relative amplitude (blue) and temperature [$^{\circ}\text{C}$] (green) versus time [hr] for the K15 sodium-modified bismuth titanate transducer high temperature endurance test	73
Figure #3.2: Plot of maximum relative amplitude (blue) and temperature [$^{\circ}\text{C}$] (green) versus time [hr] for the aluminum nitride high temperature endurance test	74
Figure #3.3: Plot of accumulated fluence (blue) and neutron power (green) against time during the beginning stage of the ULTRA irradiation	76
Figure #3.4: Plot of relative amplitude versus total fluence during the beginning of the ULTRA irradiation of the bismuth titanate transducer	77
Figure #3.5: Plot of relative amplitude (blue) and total fluence (green) versus time during the beginning of the ULTRA irradiation of the bismuth titanate transducer	78
Figure #3.6: Plot of relative amplitude versus total fluence during the beginning of the ULTRA irradiation of the aluminum nitride (ALN-2) transducer	79
Figure #3.7: Plot of relative amplitude (blue) and total fluence (green) versus time during the beginning of the ULTRA irradiation of the aluminum nitride (ALN-2) transducer	80
Figure #3.8: Temperature environment of the reactor core, measured on two thermocouples TC1 (blue) and TC2 (green) versus time at the beginning of the ULTRA irradiation	81

List of Tables

Table #1.1: Measurements of transducer assembly and component dimensions	14
Table #1.2: Mechanical, thermal, and acoustic properties of aluminum nitride	20
Table #1.3: Mechanical, thermal, and acoustic properties of bismuth titanate	24
Table #1.4: Mechanical and thermal properties of 304 stainless steel and 316 stainless steel	26
Table #1.5: Mechanical and thermal properties of kovar	26
Table #1.6: Mechanical and thermal properties of carbon-carbon composite	27
Table #2.1: Relative amplitude signal values for the K15 sodium-modified bismuth titanate transducer during the course of the high temperature endurance test	68
Table #2.2: Minimum, maximum, and average temperature values from the high temperature endurance test on the K15 sodium-modified bismuth titanate transducer	68
Table #2.3: Relative resonant frequency shift from the initial K15 transducer signal to the final transducer signal	69
Table #2.4: Relative amplitude signal values for the aluminum nitride transducer during the course of the high temperature endurance test	70
Table #2.5: Minimum, maximum, and average temperature values from the high temperature endurance test on the aluminum nitride transducer	70
Table #2.6: Relative resonant frequency shift from the initial aluminum nitride transducer signal to the final transducer signal	71
Table #3.1: Relative amplitude signals from the K15 bismuth titanate high temperature endurance test	73
Table #3.2: Relative amplitude signals from the aluminum nitride high temperature endurance test	74
Table #3.3: Relative amplitude signal values for the bismuth titanate transducer during the course of the beginning stage of the ULTRA irradiation	78
Table #3.4: Relative amplitude signal values for the aluminum nitride transducer during the course of the beginning stage of the ULTRA irradiation	80
Table #3.5: Maximum temperature recorded by each thermocouple and temperature of the thermal spike recorded by TC1	81

Table #3.6: Comparison of bismuth titanate and aluminum nitride acoustic transmission efficiencies in high temperature and irradiated conditions	82
Table #3.7: Relative efficiency differences of selected piezoelectric materials between high temperature and irradiated test conditions	82
Table #4.1: Selected piezoelectric material properties for determination of acoustic impedance	85
Table #4.2: Selected backing material properties for determination of acoustic impedance	86
Table #4.3: Transmission coefficients for selected backing materials	86
Table #4.4: Selected waveguide material properties for determination of acoustic impedance	87
Table #4.5: Transmission coefficients for selected waveguide materials	88
Table #4.6: Mechanical, thermal, and acoustic properties of zinc oxide	90

Acknowledgements

I would like to first thank my thesis advisor, Dr Bernhard Tittmann for putting up with me for my time under his supervision, not only during my graduate school years but also the two summers I spent while I was still an undergraduate, gaining a greater appreciation for the work which is Dr Tittmann's specialty. If it weren't for his welcoming and accommodating attitude, I am not certain I would have been on this particular path in my life. His call to my undergraduate advisor while I was in the midst of taking a final my junior year of my undergraduate studies set into motion of sequence of events that has led to this moment.

Next, I would like to thank my family: my mother, Susan, my father, Curt, and my sister, Stephanie, for being a never-ending source of motivation and support throughout my higher education pursuits. They have been my rock whenever I have had a decision to make about my future. They know full well that I can agonize over the smallest of decisions and knowing that they were fully supporting whatever path I chose is, was, and always will be a tremendous comfort. In my highest moments, they were there to congratulate me; in my lowest moments, they were there to build me up. Times were not always easy but I always knew I had someone who would listen to me ramble on about whatever was my latest source of angst. All of the support throughout the years has been appreciated more than I can put into words.

I would like to thank the members of my committee for taking time out of their busy schedules to read and review my thesis, providing valuable feedback.

I would also like to thank Scott Kralik for his aid in helping me gather the SEM and ESD images and plots.

Finally, I would like to thank my lab mates both present and past: Kyle Sinding, Dr. Brian Reinhardt, Alison Orr, Leland Tien, Ken Ledford, and Janet Xu in particular, for helping me by asking the questions that perhaps I had not considered or by bringing a different perspective to the task at hand.

1. Introduction

The Engineering Nanostructure Characterization Center (ENCC) is one of the few labs in the nation doing work in high temperature applications for transducer technology. It is a great privilege to be among an elite group of researchers in this field, but it is also quite daunting because the literature for our research is simply not available in abundance. In a sense, this makes us innovators in the field of high temperature transduction technology. Applications in demanding conditions/harsh environments such as nuclear reactor core characterization have been searching for a reliable methodology to analyze a structure in live time and be able to provide feedback as to whether or not the given part, support, etc. is viable for continued use. In the reactor core case, this would save valuable time and money by transferring the need for regular maintenance into maintenance when necessary. Reactor core characterization also requires a radiation tolerant system but the high temperature capabilities of the transducer cannot be overlooked given that temperatures within can reach on the order of 450-500 °C. The following experiment is meant to mimic the reactor core start up and shut down in terms of its temperature aspect and produce a comparative result to the actual reactor results to better understand the effects of temperature and radiation on the sensors. This normally would mean ramping up the temperature in a stepwise sequential fashion (thermal ratcheting) so as not to shock the transducer system. However, the lack of low temperature control on the furnace used in the experiment makes it a difficult task to accomplish. Once brought to the appropriate operating temperature, the experiment will be allowed to run over a series of weeks before shutting down.

1.1 Piezoelectric Effect

The first necessity is to delve into the piezoelectric effect which governs the interaction within and outside the transducer. The prefix piezo- originates from Greek piezein and means squeeze, push, or press. This phenomenon was first discovered by the Curie brothers, Jacques and Pierre, in the late 1800s. Therefore, the piezoelectric effect refers to the ability of a suitable material to generate an electric charge as a response to a mechanical strain/stress applied to the

material. The charge is created as the positive and negative charge centers within the material shift. This is known as the direct piezoelectric effect and is most prevalent in sensors such as the ones that are being explored in this thesis. The piezoelectric effect is most notable for the fact that it is reversible. This effect, known as the converse piezoelectric effect, is most prevalent in actuator systems. The Curie brothers only discovered the direct piezoelectric effect; it was a year after their discovery that Gabriel Lippmann discovered the converse effect. The converse effect occurs when an external electric field is applied to a suitable material which in turn causes the material to either be stretched or compressed. The constitutive piezoelectric equations are reliant on four components: stress, strain, electric field, and electric displacement. They can be written in several different forms:

Reduced matrix form under a simplified, one-dimensional assumption:

$$S_i = d_{ij}E_j \quad \text{(Eqn. 1.1)}$$

Where S_i is the strain induced by the applied electric field, E_j is the applied electric field, and d_{ij} is the piezoelectric coefficient. This is the converse piezoelectric effect.

$$D_i = d_{ij}\sigma_j \quad \text{(Eqn. 1.2)}$$

Where D_i is the dielectric displacement and σ_j is the applied stress. This is the direct piezoelectric effect.

The majority of the work done by the transducers in this research is based on direct strains on and thickness-wise expansions of the piezoelectric material (3-direction). The actual piezoelectric constitutive equations are more complex with the effects interwoven slightly as in the tensorial piezoelectric constitutive equations [2] (Giurgiutiu, 2008):

$$S_{ij} = s_{ijkl}^E T_{kl} + d_{kij} E_k \quad \text{(Eqn. 1.3)}$$

Where S_{ij} is the two-dimensional strain component, s_{ijkl}^E is the compliance at a constant electric field, T_{kl} is the two-dimensional stress component, d_{kij} is the piezoelectric strain constant, and E_k is the electric field component.

$$D_j = d_{jkl} T_{kl} + \varepsilon_{jk}^T E_k \quad \text{(Eqn. 1.4)}$$

Where D_j is the electric displacement component and ε_{jk}^T is the permittivity at a constant stress.

This is known as the tensorial representation of the strain-displacement form. The coordinate axes (i,j,k,l) are typically defined by the polarization of the piezoelectric sample which is usually in the 3-direction.

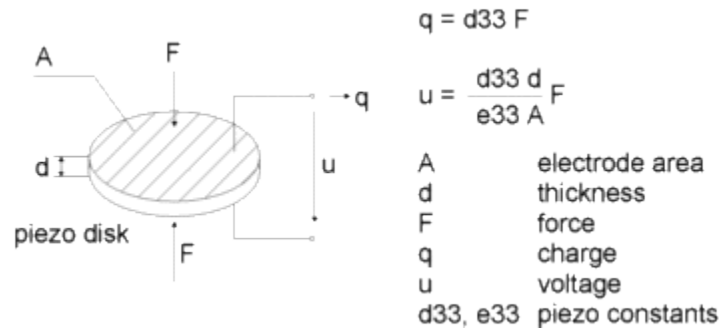


Figure #1.1: Illustration of the factors that affect the direct piezoelectric effect, displaying the force-charge and force-voltage equations [3]
http://www.new.mmf.de/piezoelectric_principle.htm

For decades after its discovery by the Curie brothers, the piezoelectric effect remained something that was only experimented on in the laboratory with further work needing to be done in order to harness the great promise that the piezoelectric effect showed. The first practical application for the piezoelectric devices was employed at the onset of World War I as a primitive form of sonar. This first broad use of piezoelectricity created developmental interest the world over, leading to the discovery of new piezoelectric materials and the exploration and development of new applications for these materials over the next several decades.

Development of piezoelectric sensors began to really take off at the onset of World War II when scientists in the United States, the Soviet Union, and Japan discovered ferroelectrics, a class of man-made piezoelectric materials with piezoelectric constants much higher than those of the natural piezoelectric materials.

1.1.1 Piezoelectric Materials

The first known piezoelectric materials, as demonstrated by the Curie brothers, were crystals of tourmaline, quartz, topaz, cane sugar, and Rochelle salt (potassium sodium tartrate). The materials which exhibited the best piezoelectric performance were the quartz, which is still relevant even today in sonar applications, and the Rochelle salt. Quartz crystals went on to become the first commercially employed piezoelectric material.

The discovery of ferroelectrics around the time of World War II really accelerated the search for higher performance materials for various applications. Some of the most prevalent piezoelectric materials forged from this research are barium titanate (BaT), a family member of the to-be-tested bismuth titanate, and lead zirconate titanate (PZT).

In recent times, there has been an initiative within the European Union to phase out the use of lead in ferroelectrics due to concerns over the toxicity levels within lead-containing devices.

1.1.2 Crystal Structures

To begin, there are thirty-two crystal structure classes that are generally accepted. Piezoelectricity is generally associated with a crystal structure having a non-centrosymmetric crystal structure, allowing the central dipole have a net dipole moment depending on which direction it is poled. In fact, this is the only crystallographic requirement for piezoelectricity to be exhibited within a material. The most common non-centrosymmetric crystal structure is the wurtzite structure as exhibited by quartz and aluminum nitride. Twenty-one of these crystal structure classes possess this non-centrosymmetric property. Of those twenty-one classes, twenty of them exhibit the piezoelectric effect. Further breakdown of the crystal class structure shows that all ferroelectric materials are pyroelectric and all pyroelectric materials are piezoelectric.

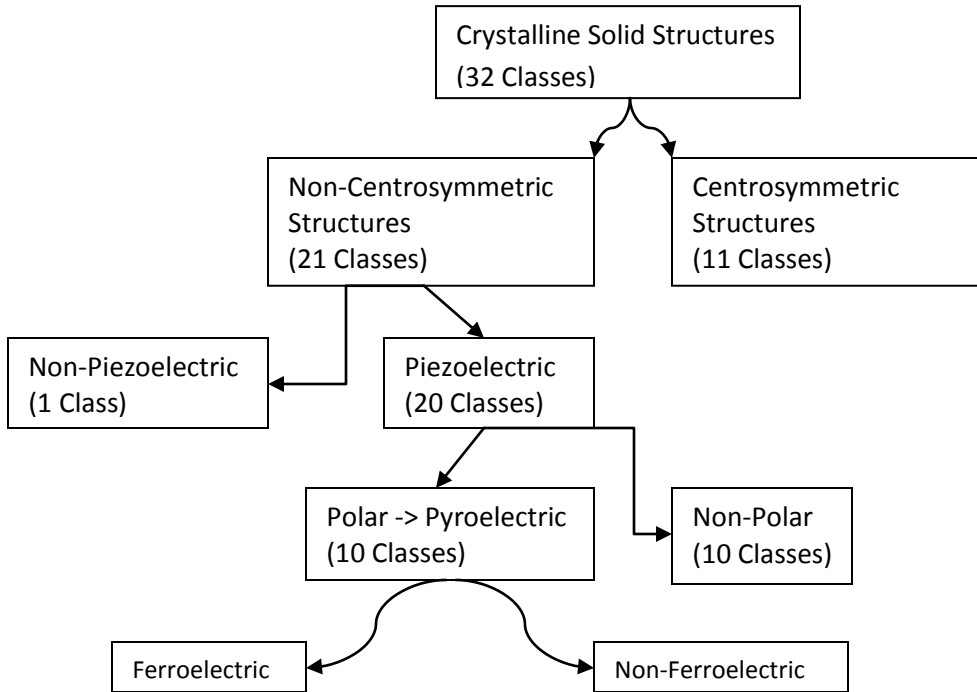


Figure #1.2: Breakdown of the thirty-two crystal structure classes based on symmetry, piezoelectricity, pyroelectricity, and ferroelectricity

Many piezoelectric materials possess a spontaneous polarization due to a separation of positive and negative charges within the crystal structure unit cell. An example that exhibits this phenomenon is the perovskite crystal structure. It occurs when the structure is cooled from the high temperature centrosymmetric cubic phase, causing a progression of phase transitions until the central atom is displaced in a non-uniform manner relative to the corner atom and therefore settling into a non-centrosymmetric structure.

Piezoelectric properties are very sensitive to temperature because the unit cell structure of the crystal dictates the properties themselves. In structures and compounds that possess a Curie temperature, the crystal lattice becomes asymmetric and distorted, causing the formation of dipoles within the lattice and therefore spontaneous polarization in piezoelectric ceramics. This process only occurs below the Curie temperature; in fact, when the temperature rises above the Curie temperature, a piezoelectric material loses its piezoelectric properties due in large part to phase transition in the crystal lattice.

As mentioned above, poling is necessary to bring the dipoles into proper alignment. Poling is the process where a directed electric field is applied to a crystal lattice structure in order to align the dipoles in a common direction to induce piezoelectric properties. Polarization is a

quantity which possesses both a magnitude and direction, therefore making it a vector quantity and is the summation of the molecular structure's individual dipoles' magnitudes and directions.

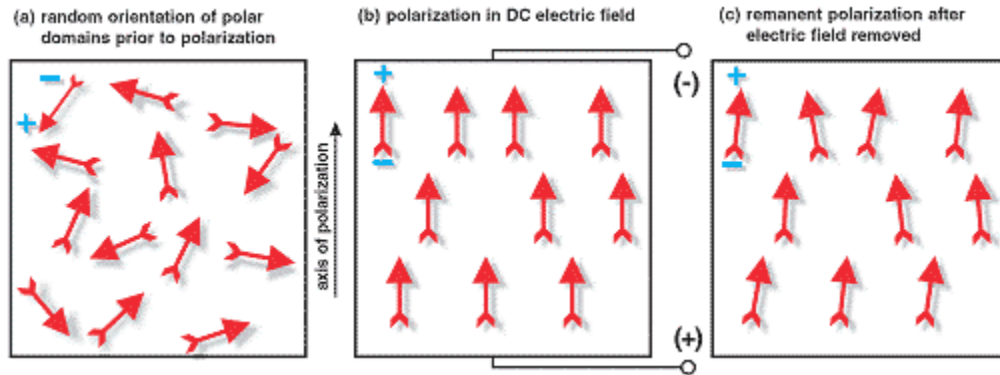


Figure #1.3: The effect of polarization in an applied electric field [4] (http://www.pc-control.co.uk/piezoelectric_effect.htm)

1.2 Background and Motivation

There is quite a bit of motivation to delve into the further development and improvement of piezoelectric sensors for a wide range of applications. In particular, the aging infrastructure in a broad range of areas has increasingly become a huge maintenance and safety concern. The infrastructure requires constant monitoring and almost as constant maintenance which can be exceedingly costly in terms of time, resources, and money. Therefore, it is important establish the means necessary for aiding industry in creating the most efficient and cost-effective method for improvement of the health of the current infrastructure in both the long and short terms.

1.2.1 Non-Destructive Testing/Evaluation versus Structural Health Monitoring

There are many methods in current use to monitor the condition of the infrastructure. The two most prevalent methods are non-destructive testing (NDT)/non-destructive evaluation (NDE) and structural health monitoring (SHM). So just what are non-destructive testing/evaluation and structural health monitoring? According to the NDT Resource Center website [5] (<https://www.nde-ed.org/AboutNDT/aboutndt.htm>),

The field of Nondestructive Testing (NDT) is a very broad, interdisciplinary field that plays a critical role in assuring that structural components and systems perform their function in a reliable and cost effective fashion. NDT technicians and engineers define and implement tests that locate and characterize material conditions and flaws that might otherwise cause planes to crash, reactors to fail, trains to derail, pipelines to burst, and a variety of less visible, but equally troubling events. These tests are performed in a manner that does not affect the future usefulness of the object or material. In other words, NDT allows parts and material to be inspected and measured without damaging them. Because it allows inspection without interfering with a product's final use, NDT provides an excellent balance between quality control and cost-effectiveness. Generally speaking, NDT applies to industrial inspections. The technologies that are used in NDT are similar to those used in the medical industry, but nonliving objects are the subjects of the inspections.

The same site also provides a definition for NDE as follows:

Nondestructive evaluation (NDE) is a term that is often used interchangeably with NDT. However, technically, NDE is used to describe measurements that are more quantitative in nature. For example, an NDE method would not only locate a defect, but it would also be used to measure something about that defect such as its size, shape, and orientation. NDE may be used to determine material properties, such as fracture toughness, formability, and other physical characteristics.

In regards to SHM, according to Chang, et al (2002) [6],

Structural Health Monitoring (SHM) is the continuous or regular monitoring of the condition of a structure or system using built-in or autonomous sensory systems, and any resultant intervention to preserve structural integrity. SHM is a broad multidisciplinary field both in terms of the diverse science and technology involved as well as in its varied applications. The technological developments necessary to enable practical structural health monitoring are originating from scientists and engineers in many fields including physics, chemistry, materials science, biology, and mechanical, aerospace, civil, and electrical engineering. SHM is being implemented on diverse systems and structures such as aircraft, spacecraft, ships, helicopters, automobiles, bridges, buildings, civil infrastructure, power generating plants, pipelines, electronic systems, manufacturing and processing facilities, biological systems, and for the protection of the environment, and for defense.

As you can see from the above definitions, NDT/NDE refers to local tests on a system performed by trained technicians who then take the collected data and manually correlate and compare it to past collected data as well as a baseline data set to determine the overall health of the system. SHM, on the other hand, performs these same tasks both

autonomously and continuously. The hope is that these transducers can bridge the gap from NDT/NDE into the realm of SHM.

1.2.2 Bulk Single Crystal Transducer

The basic principle of the piezoelectric sensor is a physical dimension is transformed into a force which in turn acts on two opposing faces of a piezoelectric sensing element. The most common sensor application comes in the form of detecting sound vibrations, most commonly seen in piezoelectric microphones and piezoelectric pickups for electric guitars. They are often used for quality assurance, process control, and materials research and development for many industries. High frequency applications for medical ultrasound and nondestructive testing in industry are also particularly common.

Ultrasound is a pervasive evaluation and testing technique and standard for many industries including nuclear. There many techniques within ultrasound that could be used if suitable transducers existed, piezoelectric active element materials characterization foremost among them. These techniques could prove to be beneficial if they were demonstrated in harsh environments.

Linear ultrasonic principles are based in particular on one fundamental assumption: that the strains undergone are sufficiently small. In anisotropic solids, the stress-strain relationship and the general wave equation take the form of:

$$\sigma_{ij} = c_{ijkl}\varepsilon_{kl} \quad \text{(Eqn. 1.5)}$$

where σ_{ij} is the stress tensor, c_{ijkl} is the stiffness tensor, and ε_{kl} is the strain tensor.

$$\rho \frac{\partial^2 u_i}{\partial t^2} = (c_{ijkl}) \frac{\partial^2 u_k}{\partial x_j \partial x_l} \quad \text{(Eqn. 1.6)}$$

where ρ is the density of the material, u_i , u_k , x_j , and x_l are several notations for displacement in varying directions, t is time, and c_{ijkl} is as above.

These equations can be correlated to (Eqn. 1.1-1.4) above. The velocity in an anisotropic solid is dependent on direction and polarity. These fundamentals are widespread in

nondestructive testing, particularly for determining elastic constants of materials, for predicting mode conversion of ultrasonic waves for oblique incidence, and for predicting dispersion in bounded media.

Measurements based on linear ultrasonic principles are pervasive throughout industry and for various other commercial applications including use as an under sodium viewing transducer [7] (Kažys, Voleišis, & Voleišienė, 2008), for condition monitoring of check valves in nuclear power plants [8] (J. Lee, M. Lee, Kim, Luk, & Jung, 2006), as an ultrasonic fission gas release monitor [9] (Villard & Schyns, 2009), for fuel porosity measurements [10] (Phani et al., 2007), and as ultrasonic thermometers [11] (Rempe, 2011a).

The transducer can be modeled as a parallel plate capacitor in series with an RLC circuit as in the work of Kim, et al. The most common models associated with the modeling of piezoelectric ceramics are the Van Dyke model as shown in Figure #1.4, the Shunt model, and the Guan model.

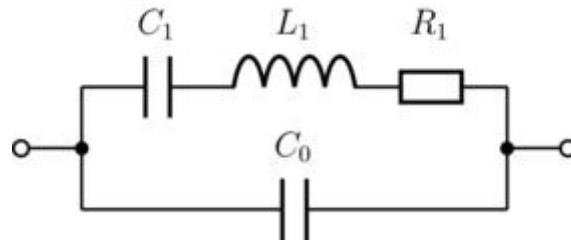


Figure #1.4: The Van Dyke model of an equivalent circuit for the bulk single crystal transducer [12] (Niedermayer, et al, 2012)

The capacitance of the piezoelectric element can be written as:

$$C_0 = \frac{\epsilon A}{d} \quad (\text{Eqn. 1.7})$$

Where: C_0 is the electrostatic capacitance of the piezoelectric sensor,
 ϵ is the permittivity of the piezoelectric material,
 A is the area of the electrode on the element, and
 d is the thickness of the element.

The impedance of the transducer can be written as:

$$Z = j\omega C_0 + \frac{1}{R_1 + j\omega L_1 + \frac{1}{j\omega C_1}} \quad (\text{Eqn. 1.8})$$

Where: Z is the impedance of the transducer,

j refers to the imaginary component,

ω is the resonance frequency,

C_0 is the electrostatic capacitance between two parallel plates as above in **(Eqn. 1.7)**,

R_1 is the resistance representing the mechanical damping of the sensor,

L_1 is the inductance representing the mass-inertia of the sensor,

C_1 is the capacitance representing the elastic compliance of the sensor.

1.2.3 Fabrication Process

The process for fabricating bulk single crystal transducers has gone through a number of iterations through the years. Each has had their fair share of problems and issues which lead to refinement and improvement of the technique in the hopes that, one day, the most efficient and least troublesome process will be discovered. A previous, but still useful methodology for fabricating the single crystal transducer is enumerated below:

- 1) Sand sensor material to desired thickness (which corresponds to roughly an 8-12 MHz resonance frequency).
- 2) Polish surfaces with 600 grit sandpaper (15 micron surface roughness).
- 3) Attach transducer waveguide.
- 4) (a) If using silver paste, apply small quantity to surface and cure at 400 °C for 20 minutes. (b) If using aluminum foil cut a round piece of foil using an X-ACTO knife and move to step 5.
- 5) Cut a round piece of foil using an X-ACTO knife for coupling between sensor and backing.
- 6) Insert spring, waveguide (insert foil if 4b).
- 7) Insert outer insulation (as guide for sensor if step 4b is taken).
- 8) Insert (if 4b taken insert first foil) sensor, foil, backing.
- 9) Attach inner and upper insulation to plunger.
- 10) Insert item 9 into transducer.

- 11)** Screw in transducer cap until assembly is snug.
- 12)** Using dremel, remove half of the outer and inner sheath layer or until the insulation is exposed along the length of wire desired.
- 13)** Use a hammer on the dremeled section to expose the lead wire. Stay a few millimeters from the end of the dremeled section as to not compress the cable and cause a potential short.
- 14)** Use wire cutters to remove the remaining outer sheath exposing the lead wire completely.
- 15)** In a small container, mix water with sauerisen in a high sauerisen to water ratio. The powder mix should be viscous but not clumpy; it should not run too quickly. It is best to add sauerisen at a scoop at a time until the desired consistency is met.
- 16)** Apply the sauerisen to the end of the cable where the lead wire is first exposed liberally.
- 17)** Fit a one centimeter long section of upper insulation (making a sheath) around the end of the cable so that cable slides half way through the insulation.
- 18)** Use a heat gun to cure the sauerisen and secure the insulation to the cable. If the heat is applied quickly then the sauerisen will cure with a highly porous structure and losses integrity, make sure to keep the heat gun several inches from the sample (at least 6) and use on a lower setting to cure. Alternatively, hot plate can be used at 400 °C and about 20 minutes is required.
- 19)** Use a digital multimeter to test the cable to ensure that it is not shorted (this was commonly an issue). If it is shorted clip the end of the cable and return to step 12.
- 20)** Screw transducer cable support onto cap
- 21)** Slip the sheath on top of the plunger end and ensure there is contact between the lead wire and the plunger.
- 22)** Screw the top onto the cable support to fix the cable to the transducer.
- 23)** Test the transducer to ensure that pulse echo amplitude is sufficient.

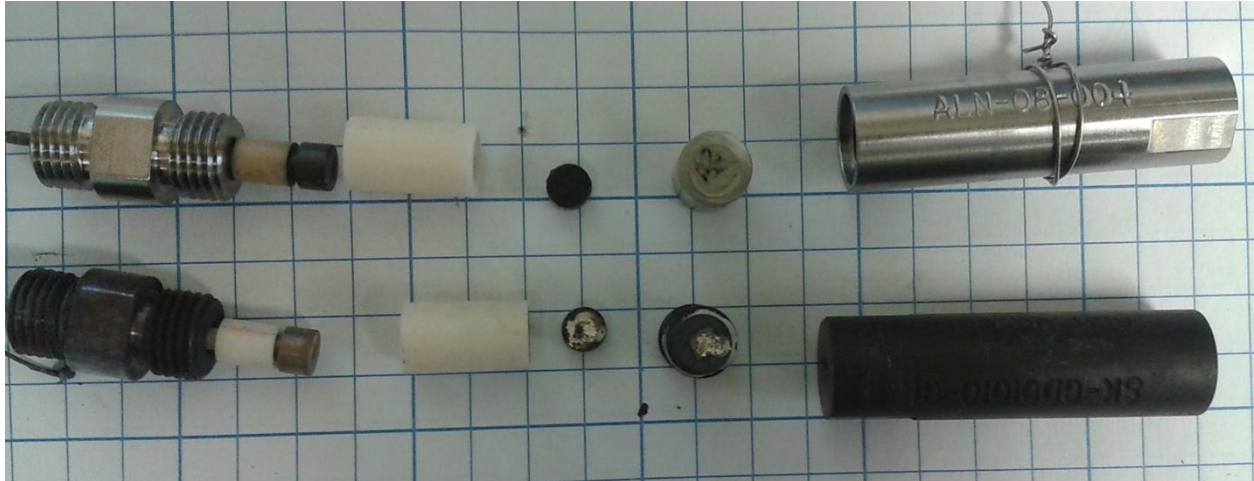


Figure #1.5: Two separate disassembled transducer constructions with components laid out in a sequential order

The current method of bulk single crystal transducer fabrication process when done within the ENCC lab is as follows:

- 1) Begin with a 304 stainless steel casing. 304 SS has the important property of being non-magnetic.
- 2) Add a high temperature-capable spring for purposes of increasing the pressure within casing. The piezoelectric effect thrives on increased pressure.
- 3) Either place (a) aluminum/gold foil or (b) apply a layer of Aremco high temperature binder between the bottom of the piezoelectric (AlN, BiT, ZnO) wafer and a kovar/stainless steel waveguide for conduction purposes. The frequency of transducer depends on thickness of piezoelectric wafer.
- 4) Repeat step 3 except we place (a) aluminum/gold foil or (b) apply the Aremco high temperature binder (1/1 mixture with water) between carbon-carbon backing and the top of the wafer. The carbon-carbon backing is important because it is a very porous material, it remains stable even at high temperatures, and it is an acoustic dampener, reducing ringing within a signal.
- 5) Proceed to add alumina insulation over the waveguide construction.
- 6) Then, slide the waveguide into the casing.
- 7) Next, add a nickel plunger and slide a smaller piece of alumina insulation over the plunger to further reduce ringing in the system.

- 8) Finally, screw on the 316 stainless steel cap. The cap will ensure pressure throughout the transducer system.
- 9) For the lead wire construction, expose and properly insulate the lead wire before attaching to the transducer. A new technique for making the connection between the transducer and the lead wire will be examined. The previous lead wire-to-transducer connection was littered with issues including but not limited to lead breakage and loss of connection in the midst of curing. The plunger will have a micro-hole drilled into the top of the plunger which will allow the lead to be inserted directly into the lead; therefore, eliminating the loss of connection issue.
 - a. Use a dremel to expose the copper lead within the mineral-insulated thermocoax cable.
 - b. Gently use a tool (hammer, wire cutters, etc) to remove the excess mineral insulation.
 - c. Use tweezers to slowly pull out the end of the copper lead from the sheath.
 - d. Use wire cutters to remove the excess sheath.
 - e. Gently insert the lead into the micro-hole drilled into plunger since the copper lead is rather brittle.
 - f. Screw on the strain relief gauge to provide stability to the lead-to-plunger connection.
 - g. Be sure to check the resistance of the thermocoax cable with multimeter after each completed step; the multimeter should read in the mega-ohm resistance range or above otherwise the cable has shorted and we return to step 9a after clipping the shorted-out end.
- 10) (a) Proceed to braze the coupling material (aluminum/gold foil) in a furnace. The foil should be soft after the brazing process so as to take full advantage of the pressure in the rest of the system and provide the best conductance. The temperature employed should be above annealing temperature of the material (aluminum/gold) but below the melting temperature for obvious reasons; a temperature at the midway point between the two is typically used in this process. (b) When using the Aremco high temperature binder, air drying the waveguide construction for two hours is required prior to insertion into the casing.

11) Transducer system is ready for action.

This particular transducer system works through an impulse of electrical energy through a lead wire or other conducting medium into, through the plunger and backing material, and into the piezoelectric wafer. The piezoelectric then transfers the electrical energy into an acoustic waveform which travels through the waveguide, rebounding off the far side and returning along the same pathway back to a device such as an oscilloscope which displays the pulse-echo response of the transducer. The performance of the transducer, in this case, is determined by the relative increase or decrease in signal amplitude over a given time period in the test conditions.



Figure #1.6: Disassembled components of the bulk single crystal transducer assembly (from left to right) 304 stainless steel cap, nickel plunger with alumina insulation, carbon-carbon backing material, gold foil coupling, alumina insulation, aluminum nitride piezoelectric element, gold foil coupling, kovar waveguide, iron-nickel-cobalt alloy spring, 316 stainless steel casing

The dimensions of the transducer assembly as well as the individual components can be seen in Table #1.1 below.

Component	Length (cm)	Diameter (cm)	Ring Width (cm)
Casing	4.0	1.15	n/a
Spring	0.5	0.8	n/a
Waveguide	1.2	0.75	n/a
Insulation	1.35	0.8	0.1
Backing	0.4	0.55	n/a
Plunger	3.35	0.5/0.1	n/a
Cap	2.0	0.9	0.3
Strain relief gauge	3.4	1.15	n/a
Assembly	7.5	1.15	n/a

Table #1.1: Measurements of transducer assembly and component dimensions

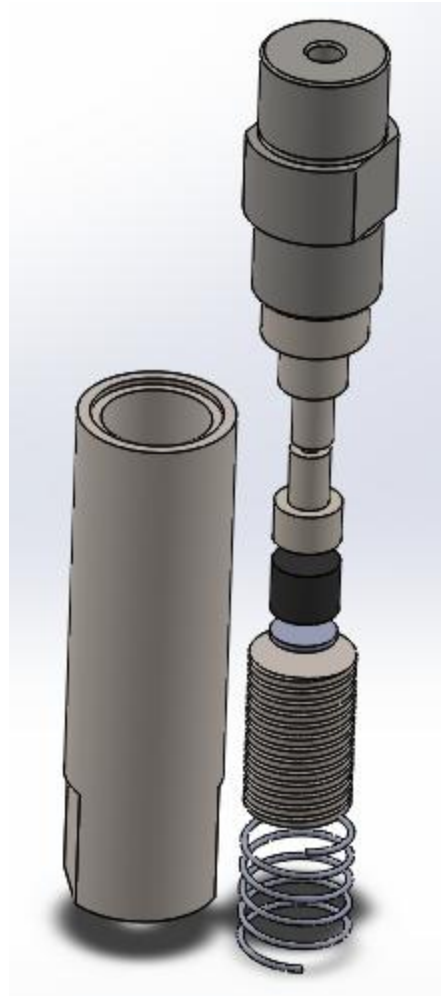


Figure #1.7: 3D solid model of the bulk single crystal transducer assembly

As shown above, the biggest change in the fabrication process is the elimination of the use of saureisen. Although the ceramic can indeed provide improved connection strength, it was also rather brittle if not cured properly which in turn led to more issues than it solved. The biggest issue with this process is not in the transducer construction itself, but in the lead wire to transducer plunger connection. One possibility is to use a thicker gauge mineral-insulated thermocoax cable. The other solution requires a machine shop in order to add both stability and pressure to the system.

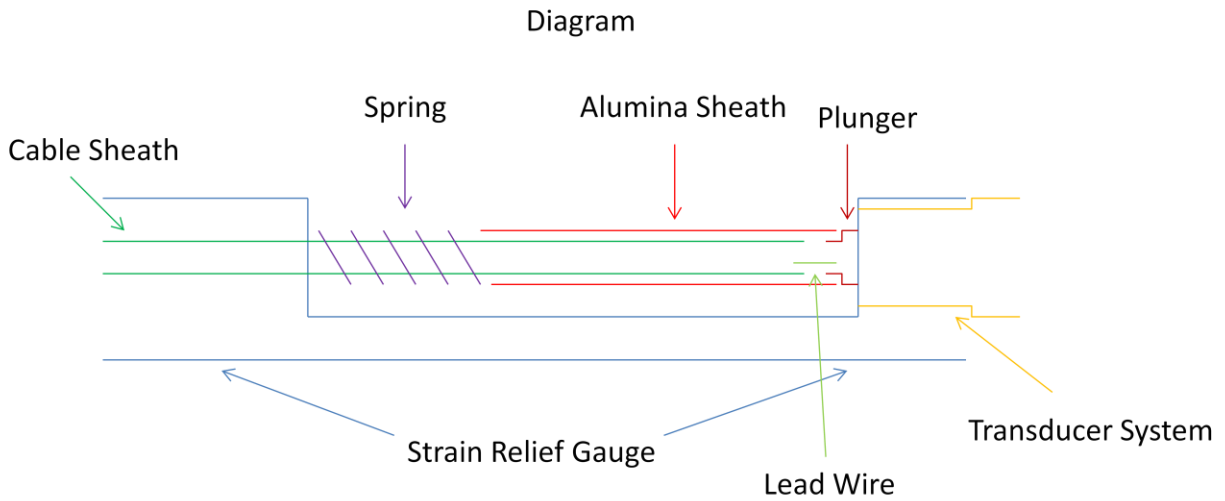


Figure #1.8: Rendering of the schematics sent to the machine shop

However, due to the complexity of disassembling and reassembling the machine shop construction, a simple contact-pressure connection was made, stabilized by the strain relief gauge.



Figure #1.9: Fully constructed bulk single crystal transducer assembly connected to the mineral-insulated thermocox lead wire and stabilized by the strain relief gauge



Figure #1.10: Close-up of the fully constructed bulk single crystal transducer assembly, illustrating the connection between the lead and the plunger

1.2.4 High Temperature Environment

A high temperature environment causes piezoelectric breakdown within the structure of the crystal. Universally, as the operating temperature increases, piezoelectric performance decreases. Piezoelectric materials with a Curie temperature will undergo complete and total depolarization when exposed to temperatures above their Curie point. This Curie point is typically referred to as the maximum possible exposure temperature for a material. When choosing an operating temperature for a piezoelectric sensor, it is best to select a temperature that is substantially below the Curie temperature in order to facilitate performance of the sensor. In applications with long term exposure and operation, the temperature limitations of a piezoelectric material tend to decrease. This means that the aging process of a given material is accelerated, decreasing performance and reducing the maximum stress level at elevated temperatures.

Another primary effect on any material subject to a high temperature environment is thermal expansion. Thermal expansion is the tendency of a given material to change its physical dimensions (area, volume, and shape) through a heat transfer process. When undergoing thermal expansion, solids tend to keep their overall shape, but their volumes may undergo changes depending on conditions. Bond strength within a crystal structure has a significant effect on thermal expansion within solids. Materials with high bond strengths between atoms and, therefore, high melting points such as crystals will tend to have a low thermal expansion coefficient. Materials with lower bond strengths and consequently lower melting points such as glasses will tend to have higher thermal expansion coefficients. The coefficient of thermal expansion refers to the physical response (change in volume, etc) of a material to a change in temperature. The most common coefficient of thermal expansion is the volumetric coefficient of thermal expansion which is mainly used to characterize the change in volume in solids and liquids.

$$\alpha_V = \frac{1}{V} \left(\frac{\partial V}{\partial T} \right)_P \quad \text{(Eqn. 1.9)}$$

Where α_V is the volumetric coefficient of thermal expansion, V is the volume of the material, and $\left(\frac{\partial V}{\partial T} \right)_P$ is the change in volume given a change in temperature at a constant pressure.

In addition to thermal expansion, one has to be aware of oxidation processes when dealing with non-inert environment applications in high temperature. Oxidation refers to a loss of electrons in an atom or molecule. Oxidation reactions are most commonly associated with the interaction of oxygen with a material, usually a metal or metallic compound, which causes an oxide layer to form on the surface of the material.

1.2.5 Irradiation

Finding suitable materials that can handle both the temperature strain and radiation pressure in harsh environment applications is vitally important. In regards to the piezoelectric materials in particular, a high radiation environment causes point defects to form within the crystal structure which can lead to scattering. Hazardous byproducts of the radiation can lead to transmutations of the structure itself. Localized heating from gamma radiation leads to increased

strain on certain components within the transducer over others. This all leads to a decrease of over 50% as reported in many materials at moderate fluence levels. The perovskite crystal structure typically fails due to phase transitions within the crystal lattice. Depolarization, phase transformations, and metamictization are all reported failure mechanisms of piezoelectric materials in irradiated environments. Depolarization is the process by which a crystal structure that has a defined polarization undergoes a rapid shift in the direction of its polarization, resulting in the loss of its remnant polarization. Without a polarization direction, the piezoelectric potential disappears. There are typically two kinds of phase transformations that occur in solid and metallurgical crystal structures: diffusional transformations and displacive transformations. Diffusional transformations generate a different chemical composition in the new phase of the compound. This new phase requires atoms to traverse relatively long distances due to its compositional differences to the parent phase. It is a process that is dependent mainly on time rather than temperature and is an isothermal transformation which means that it is capable of occurring at constant temperature. Displacive transformations changes the crystal structure itself rather than the chemical composition of the starting phase. Since it is based on changes at an atomic structural level, it does not require the atoms to move long distance. Slight atomic adjustments cause the formation of a new phase which ideally is a more stable structure than the original. The process occurs in a time-independent fashion since it does not require atomic migration and is an athermal transformation since temperature is the determining factor in the amount of the new phase that forms. Metamictization is the process by which a crystal structure is gradually destroyed by repeated bombardment of an internal or external nature. This leaves the structure in an amorphous state and thereby eliminating any piezoelectric potential.

1.3 Literature Review

1.3.1 Materials Properties and Reactions

Each of the materials currently employed in fabricating a bulk single crystal transducer are to be examined in terms of their thermal, mechanical, electrical, etc. properties. These materials are the following:

- 1) Piezoelectric material: aluminum nitride (AlN), bismuth titanate (BiT)
- 2) Transducer casing: 304 stainless steel (304 SS)

- 3) Transducer cap: 316 stainless steel (316 SS)
- 4) Waveguide: kovar, 304/316 SS
- 5) Backing: carbon-carbon (C-C) composite

1.3.1.1 Aluminum Nitride

Bulk single crystal aluminum nitride possesses many qualities and properties that make it ideal for high temperature transduction applications. First of all, it possesses the wurtzite crystal structure which has been found to resist changes in lattice formation. Other properties include but are not limited to: stable piezoelectric properties at elevated temperatures, high sound velocities, ability to operate in harsh environments, no phase transition up to and beyond its melting point, and transparency in the UV range. Aluminum nitride also possesses a high operating temperature coupled with a moderate coupling coefficient. The artificial transmutation of nitrogen occurs when nitrogen-14 interacts with an alpha particle (helium-4), forming oxygen-17 and hydrogen as residuals. The natural transmutation of nitrogen occurs when nitrogen-14 interacts with a neutron, forming carbon-14 and hydrogen as residuals. This is the main reaction that could cause issues in nuclear reactor applications. However, in the work of Yano, et al [13], as well as that of Ito, et al [14], established that this natural transmutation process is not a concern for nuclear reactor applications, showing nitrogen within the structure does transmute but the stoichiometry provides stability for the element. While it does not possess the highest electro-mechanical coupling coefficient or d_{33} value among piezoelectric materials, the properties enumerated above and below more than make up for this discrepancy. Some of the common properties associated with aluminum nitride can be seen in Table #1.1 below.

Material	Elastic Modulus (GPa)	Density (g/cm ³)	Thermal Expansion (m/m/°C)	Piezoelectric Sensitivity (d_{33}) (pC/N)	Coupling Coefficient (k_{33})	Curie Temperature (°C)	Melting Temperature (°C)	Oxidation Temperature (°C)
AlN	350	3.26	4.5(10 ⁻⁶)	5	0.3	Far exceeds melting temperature	2826	800-1000

Table #1.2: Mechanical, thermal, and acoustic properties of aluminum nitride

There are two different forms that aluminum nitride crystals take: the more nitrogen-rich clear crystal and the more aluminum-rich brown crystal. Previous work [1] (Parks, et al., 2010) has shown that clear aluminum nitride crystals are capable of performance up to at least 400 °C,

later showing that it was capable of performance up to 1000 °C where oxidation reactions began to seriously degrade the transduction capabilities of the crystal; brown aluminum nitride crystals were shown to be only capable of performance up to 300 °C. It is thought that this failure is due to a high density of defects present within the sample. There is a correlation between the quantity of defects present and defect chemistry within the crystal structure and crystal color (brown or clear). The following images were taken using a Keyence VHX Optical Microscope and illustrate the cosmetic differences between the clear and brown aluminum nitride crystal forms.

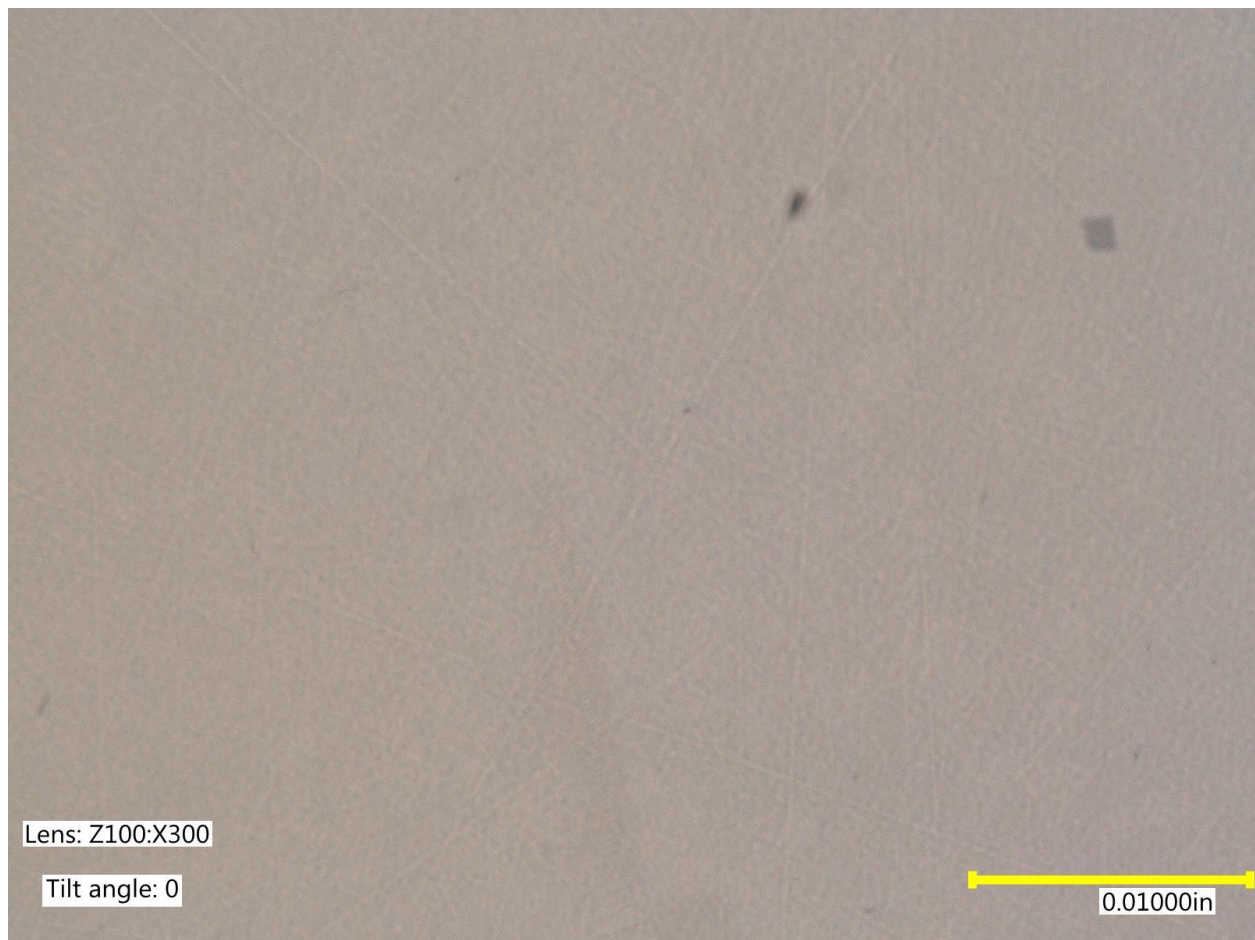


Figure #1.11: Microscope image of HT-2412 aluminum nitride crystal

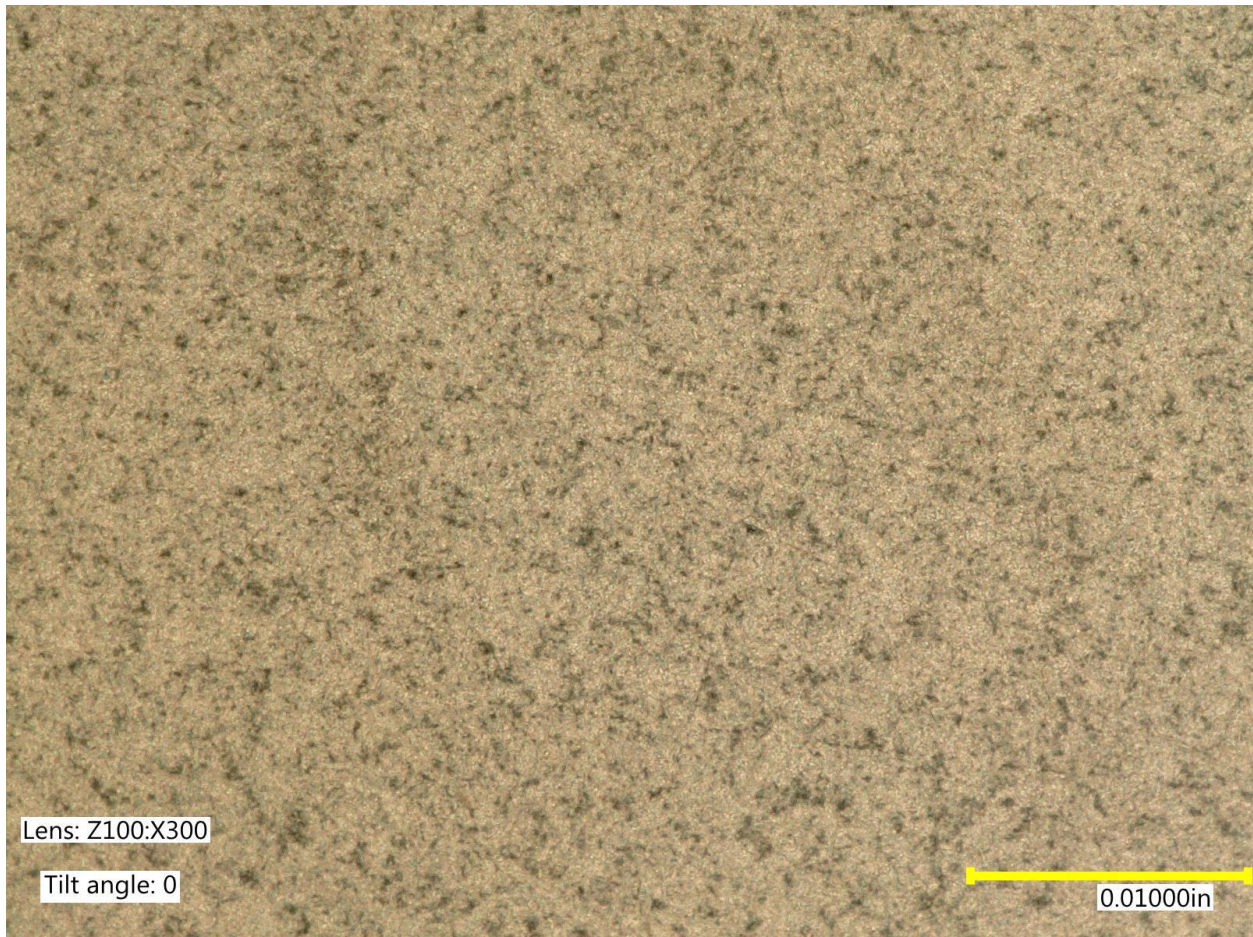


Figure #1.12: Microscope image of HT-2572 aluminum nitride crystal

Literature seems to suggest an approximately 25% decrease in the performance of aluminum nitride in terms of its d_{33} as a function of temperature based on annealing studies.

In “Oxidation of Aluminum Nitride for Defect Characterization”, Edgar, et al. observed that the oxidation rate of a crystal was based on the orientation, polarity, stress, and condition of the surface of the crystal itself. Oxidation tends to occupy grain boundaries, polishing scratches, and inversion domains by forming oxidation layers of varying thickness. Oxidation in aluminum nitride begins to occur around 800 °C and is known as low temperature oxidation. This form of oxidation generates an amorphous oxide layer which in turn leads to the generation of a high density of defects such as dislocations, vacancies, etc. particularly around the oxide-nitride interface (observed through cross-sectional transmission electron microscopy). High temperature oxidation (oxidation around 1000 °C) generates a crystalline oxide layer, leaving the nitride free of discernible defects. For best effectiveness, the defect densities within an aluminum

nitride crystal must be as low as possible. Oxidation reactions can be used for “selective defect etching”.

In “Oxidation Behavior of AlN substrate at Low Temperature”, Lee, et al. observed that oxidation began in the 800-900 °C range and covered the entire substrate surface with a layer of aluminum oxide below 1100 °C. They also observed that the oxidation kinetic follow a linear rate law below 1000 °C and a parabolic rate law above 1000 °C. Surface roughness was dramatically affected above 1100 °C as the oxide began to grown unevenly. Above 1200 °C, the oxide layer was seen to crack and split due to the difference in thermal expansion coefficients between aluminum nitride and aluminum oxide.

In “Early Stages of Oxidation of Aluminum Nitride”, Geng and Norton explain that the oxidation behaviors of ceramics have received far less attention than that of their metallic counterparts. In their examination of aluminum nitride, they found that the onset of oxidation occurred within the range of 700-800 °C based on weight gain and visual inspection. When oxidized at temperatures exceeding 1100 °C, the oxidation product of aluminum nitride is a thermodynamically stable alumina. Microstructural damages began to occur in the aluminum nitride sample around 800 °C.

In the work of Parks, et al [1], it was found that the oxidation of aluminum nitride had no significant impact on the efficiency of the material as an ultrasonic transducer, but the difficulty in procuring high purity/quality aluminum nitride crystals might limit their application in industry.

1.3.1.2 Bismuth Titanate

Bismuth titanate ($\text{Bi}_4\text{Ti}_3\text{O}_{12}$) is a piezoelectric material which has seen an uptick in its usage in recent years for all applications due to the push for lead-free piezoelectric devices throughout the scientific community. Bismuth titanate possesses the layered perovskite crystal structure which typically tends to fail due to phase transformations in high temperature conditions. It is capable of being used on non-flat surfaces such as pipes through the sol-gel deposition method. With an active working temperature of only around 330 °C, bismuth titanate typically requires some form of doping to ensure performance at higher working temperatures. Although its Curie temperature is upwards of 650 °C, it is typical to limit the maximum

recommended operating temperature of bismuth titanate, or any other piezoelectric material with a Curie temperature, to a temperature that is about half that of the Curie temperature. Another reason for doping the ceramic is the high electrical conductivity that is prevalent in pure bismuth titanate. The most common elements used in the doping process are niobium and sodium. However, the doping process, particularly with niobium, reduces the Curie temperature of the ceramic, but is capable of increasing the piezoelectric sensitivity by nearly 6 times depending on the level of doping [15] (Shulman, et al, 1996). Below in Table #1.2 are some common properties associated with bismuth titanate ceramics.

Material	Elastic Modulus (GPa)	Density (g/cm ³)	Thermal Expansion (m/m/°C)	Piezoelectric Sensitivity (d ₃₃) (pC/N)	Coupling Coefficient (k ₃₃)	Curie Temperature (°C)	Melting Temperature (°C)	Oxidation Temperature (°C)
BiT	135	7.2 (K15) - 7.95 (pure BiT)	5.5(10 ⁻⁶)	20	0.15 (K15) - 0.23 (pure BiT)	650	875 (for Bi ₁₂ TiO ₂₀ decomposing into Bi ₄ Ti ₃ O ₁₂ and Bi ₂ O ₃)	n/a

Table #1.3: Mechanical, thermal, and acoustic properties of bismuth titanate

A majority of the literature on bismuth titanate transducers is based on different methods of fabrication such as sol-gel deposition and mixed-oxide. Therefore, due to the variation in the fabrication methods between researchers, the properties of the bismuth titanate and results gathered from analysis are also rather varied. Much of the research done also includes the use of various dopants as acceptors for bismuth, such as cadmium and strontium, and titanium, such as iron, as well as donors such as niobium [15] (Shulman, et al, 1996).

In “Investigation into the use of Bismuth Titanate as a High Temperature Piezoelectric Transducer”, McAughey, et al, found that the piezoelectric coefficient of pure bismuth titanate transducers is stable up to temperatures of 550 °C, giving confidence in its high temperature capabilities for the following high temperature endurance testing.

1.3.1.2.1 BiT, Sodium-modified BiT, & BNT

Due to the common use of sodium as a dopant for improved high temperature performance in pure bismuth titanate ceramics, it is necessary to make a differentiation between sodium-modified (K15) bismuth titanate and sodium bismuth titanate (NBT) or bismuth sodium titanate (BNT), depending on the author.

K15 sodium-modified bismuth titanate is a recent innovation in the area of both lead-free ceramics and high temperature piezoelectric materials. Due to this fact, there is very little actual published literature on its performance in high temperature conditions.

Bismuth sodium titanate, in contrast, has a more extensive literary background. Aksel and Jones [16] report that the high sodium doping in bismuth sodium titanate reduces the Curie temperature of the ceramic by over half, but improves the piezoelectric sensitivity by a factor of over three and a half. It also retains the high conductivity property of pure bismuth titanate. The lower Curie temperature and a substantially lower depolarization temperature, limit its high temperature application.

Takenaka and Nagata [17] report that when the sodium bismuth titanate ceramic is formed through a hot pressing process, the Curie temperature no longer is a factor and the piezoelectric sensitivity is increased by a factor of over four and a half. However, it seemed there was no way to consistently improve the depolarization temperature which leaves the ceramic limited in a high temperature environment.

There is quite an obvious difference in atomic structure between K15 sodium-modified bismuth titanate and sodium bismuth titanate. Whereas K15 is only 3% mol by weight sodium added to the bismuth titanate structure, sodium bismuth titanate sees a substitution of sodium for bismuth within the crystal structure in a 1-to-1 ratio. This leads to the variation in the mechanical, piezoelectric, and thermal properties between the two ceramics.

1.3.1.3 Stainless Steel

Stainless steels are favored for their anti-corrosion properties. They are differentiated from carbon steel by the amount of chromium present in the alloy. Carbon steel readily activates with air and water, forming iron oxide or rust on the surface which in turn form more and more rust, causing the steel to corrode and break down. Stainless steel, due to the chromium present, forms a passive chromium oxide layer which protects the surface from rusting and corrosion by preventing oxygen diffusion to the surface. For oxidation resistance at ambient temperatures, addition of 13% by weight chromium is usually employed and 26% by weight in harsh environments. 304 is the most common stainless steel in circulation. It is non-magnetic and not highly electrically or thermally conductive as well. It is rather easy to form into various shapes for a wide range of uses. 316 possesses an even stronger resistance to corrosion than 304 as well

as strong pitting resistance and resistance to chemicals. The biggest difference between the two stainless steel alloys is the higher nickel content in 316 stainless steel.

Material	Elastic Modulus (GPa)	Density (g/cm ³)	Thermal Expansion (m/m/°C)	Melting Temperature (°C)	Oxidation Temperature (°C)
304 SS	200	8.03	16.9-18.7(10 ⁻⁶)	1399-1454	812-899
316 SS	193	7.99	16.0-17.5(10 ⁻⁶)	1371-1399	871-899

Table #1.4: Mechanical and thermal properties of 304 stainless steel and 316 stainless steel

1.3.1.4 Kovar

Kovar is an iron-nickel-cobalt alloy (typically 54% Fe-29% Ni-17% Co) which is produced in a highly controlled manner to ensure precise and uniform mechanical and physical properties. It possesses a thermal expansion coefficient similar to that of borosilicate glass, making it ideal for uses that require matched sealing between metal and glass components such as in vacuum systems. Another advantage that kovar possesses is that it is an inert metal alloy which does not oxidize, a tremendous boon to high temperature applications particularly in non-inert environments. It was initially fabricated as a means of forging direct mechanical connections over a range of temperatures in a variety of electrical conductive devices such as vacuum tubes, X-ray tubes, microwave tubes, and even light bulbs.

Material	Elastic Modulus (GPa)	Density (g/cm ³)	Thermal Expansion (m/m/°C)	Curie Temperature (°C)	Melting Temperature (°C)	Oxidation Temperature (°C)
Kovar	207	8.36	4.9-11.5(10 ⁻⁶)	435	1450	n/a

Table #1.5: Mechanical and thermal properties of kovar

1.3.1.5 Carbon-carbon composites

Reinforced carbon-carbon composite is a material well-suited for structural high temperature applications due to its low thermal expansion coefficient and high thermal shock resistance. It is a unique composite material consisting of carbon fibers embedded into a carbonaceous matrix. Due to improved oxidation resistance and decreasing manufacturing costs, this type of material has become increasingly employed in high performance applications such as

in aerospace for aircraft brakes and rocket nozzles. The material itself is quite dependent on the manufacturing methods employed, meaning that the composites can be specially tailored by combining production processes.

Material	Elastic Modulus (GPa)	Density (g/cm ³)	Thermal Expansion (m/m/°C)	Curie Temperature (°C)	Melting Temperature (°C)	Oxidation Temperature (°C)
Carbon-carbon composite	95	1.3-1.8	4(10 ⁻⁶)	n/a	n/a	450 (pure carbon), >2000 (C-C composite)

Table #1.6: Mechanical and thermal properties of carbon-carbon composite

According to Manocha [18], carbon-carbon composites made with thermal setting resins tend to have low densities (between 1.55-1.75 g/cm³) and “well-distributed microporosity”. These resin-based composites also possess “high flexural strength, low toughness, and low thermal conductivity”. In particular, “carbons with covalently bonded atoms possess very high specific strengths (40-50 GPa) and retain this strength at high temperatures in the temperature range over 1500 °C”. These carbon-carbon composites have low densities compared to ceramics and metals, are rather lightweight, possess high strength at high temperature (3000 °C) in non-oxidizing environments, a low thermal expansion coefficient, higher thermal conductivity than that of copper or silver, high thermal shock resistance, and low recession in high pressure environments. In fact, the mechanical strength of the carbon-carbon composite increases with increasing temperature, in contrast to the strengths of metals and ceramics. These composites possess high fracture toughness as well as good creep and fatigue resistance. In high temperature (2000 °C) inert environments, carbon-carbon composites have exhibited a 10-20% increase in mechanical properties. In air, the properties drop to 10-20% depending on temperature and time. These composites are quite stable and highly sought after for nuclear applications; at fluence below 10²¹ n/cm², the composite increases strength and fracture toughness by 20-30% and Young’s modulus by 30%.

Since carbon-carbon composites have a variety of microstructures, it is difficult to estimate their thermal transport properties. Thermal conductivity and thermal expansion coefficient are both heavily dictated by fiber orientation (parallel to fiber direction, high thermal conductivity/low coefficient of thermal expansion; perpendicular to fiber direction, low thermal conductivity/higher coefficient of thermal expansion). This is due to the highly anisotropic nature of the composites.

Pure carbon is prone to reaction with oxygen above 450 °C. Therefore, long term, high temperature applications in normal environments may require the composite to be protected against oxidation.

Luo, et al [19], saw that the higher the porosity of the carbon-carbon composite, the lower the coefficient of thermal expansion would be. Thermal conductivity values were far higher in the x-y-direction (parallel to the carbon fibers) than the z-direction (perpendicular to the carbon fibers).

Chłopek, et al [20], explained that carbon-carbon composites contain synthetic carbon to strengthen and reinforce the elemental carbon. The following properties result from this formation: “high strength and stiffness in high temperature applications, thermal shock resistance resulting from high thermal conductivity and low thermal expansion, good chemical resistance and low density resulting from the low atomic weight of elemental carbon.” Only issue with synthetic carbons is that they are prone to high temperature oxidation.

1.3.2 Gold-Aluminum Boundary Interactions

It was made aware to the author of a possible issue with gold-aluminum interactions, so it became necessary to investigate the ramifications of the gold-aluminum interactions.

According to Hansen [21], there are five intermetallic phases that are reported in the gold-aluminum phases; AuAl₂, AuAl, Au₂Al, Au₅Al₂, and Au₄Al. Some of these phases may never occur however since gold and aluminum join rapidly in the solid state. The AuAl₂ phase has been attributed with a phenomenon known as ‘purple plague’ where a ‘purple phase’ appears in the interdiffusion zone.

According to Philofsky [22], this ‘purple phase’ has only been observed in minute quantities. The reasoning for this observation is that the growth rate is very slow, even becoming negative at temperatures above 400 °C due to the AuAl phase growing into the AuAl₂. At temperatures above 400 °C, it is also noted that vacancies begin to form within the phase due to the Kirkendall effect where the aluminum diffuses out of the phase faster than the gold can move into the phase. Eventually, the vacancies form an almost continuous line which has a serious negative effect on the coupling between elements. The AuAl phase, known as the ‘white phase’, only appears after a long time at low or high temperature which suggests difficulty nucleating.

As mentioned above, the ‘white phase grows into the ‘purple phase’ by excess gold diffusing into it. The ‘tan phase’, Au_2Al , nucleates slowly, but grows rather rapidly once nucleation occurs. The most prominent phase, Au_5Al_2 , nucleates almost immediately and grows at the fastest rate of any phase. Due to the rapid nucleation and growth rates, cracking was seen around the gold-aluminum interfaces at temperatures of 400 °C. The Au_4Al phase is present in most interactions, but has a very slow growth rate.

Most aluminum nitride single crystals are approximately half nitrogen in atomic content with a small percentage of oxygen. I have not found any literature that mentions phases forming between high purity gold foil and aluminum nitride single crystals. Therefore, I am confident that these gold-aluminum interactions and phases will have minimal impact on my research.

1.4 Dissertation/Thesis Scope

As stated previously, the main thrust of this research is to attempt to, not only construct and test, but also optimize a sensor that is capable of both structural health monitoring as well as non-destructive evaluation in high temperature and potentially harsh environments.

Nuclear power plants of all sorts provide harsh environments in and near the core that can severely alter material performance, and limit component operational life. The current inspection paradigm is based on cook and look methodologies. This is problematic for a number of reasons namely: it is an expensive process which costs the power industry millions of dollars per year. It provides an insufficient amount of data for the amount of money spent on procuring it. Finally, there are exceedingly long wait times, up to 18 months per data point in commercial reactors. All of these factors combined highlight that it is paramount to design transducer capable of acquiring data in-situ for high temperature and harsh environment applications.

2 High Temperature Endurance Runs

As stated prior, the intent of the experimentation is to mimic the conditions of a nuclear reactor in terms of its temperature component. The transducers will be subject to temperatures upwards of 430-450 °C, the level of temperatures you would expect to find in the core of a reactor. The temperature will be held as constant as possible for a month to a month and a half ideally. In order to ensure a relatively constant temperature throughout, a K-type thermocouple attached to a digital multimeter or a designated thermocouple reader will be employed. The acoustic data will be recorded using a LabView program installed on a National Instruments operating system with an oscilloscope feature. Data will be taken every hour and the temperature will be recorded every hour (to the best of the author's ability). When unable to record the temperature personally, an exponential decay and growth model based on the trends in heating and cooling observed with regards to the furnace was employed.

$$\text{Cooling: } T = T_0 e^{-ct} \text{ (Eqn. 2.1)}$$

$$\text{Heating: } T = T_0(1 - e^{-ht}) \text{ (Eqn. 2.2)}$$

Where T is the cooled/heated furnace temperature in Celsius, T_0 is the initial temperature in Celsius, t is time in hours, c is cooling rate, and h is heating rate.

A Thermolyne 21100 tube furnace is used to provide the high temperature environment for the endurance testing. The K-type thermocouple is inserted into one side of the furnace while the transducer is inserted into the other side. Each component is wrapped at the outer ends by flame-retardant insulation in order to hold them in place; the insulation also isolates the environment inside the furnace. Prior to running the endurance tests, a series of tests were run to determine the optimal furnace setting. Each tick mark on the furnace dial was tested to determine its temperature level.



Figure #2.1: Thermolyne 21100 tube furnace used for high temperature endurance runs

To power the transducer, a BNC cable and alligator clip BNC connector is attached to an Olympus Panametrics-NDT Model 5800 Computer Controlled Pulser-Receiver. The Panametrics system allows the ability to control the input mode (pulse-echo or through-transmission), the internal pulse frequency (PRF) (80 Hz – 10 kHz), the input energy (12.5 – 100 μ J), the damping resistance (25 – 500 Ω), the high and low pass filtering (HP: 1 kHz – 1 MHz; LP: 5 – 35 MHz), the input (coarse: 0 – 50 dB in 10 dB intervals) and output (fine: 0 – 15.9 dB in 0.1 dB intervals) attenuation, and the gain (20 – 60 dB). It also possesses a bandwidth of 35 MHz. The alligator clips are then attached to the lead wire of the transducer. The alligator clips are not temperature resistant and therefore must remain outside of the furnace atmosphere.



Figure #2.2: Olympus Panametrics-NDT Model 5800 Computer Controlled Pulser-Receiver used to power the transducer

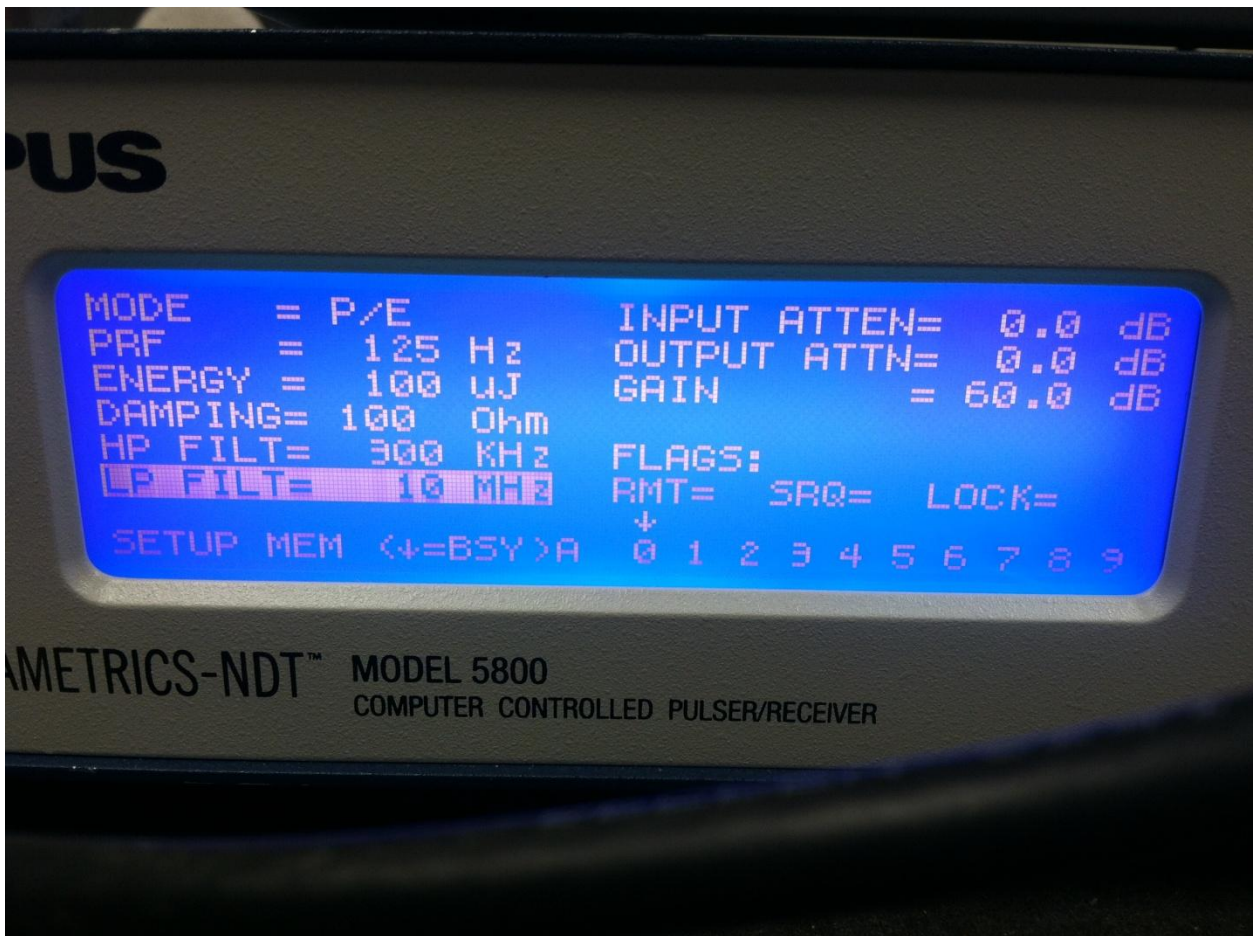


Figure #2.3: Example of settings used for spray-on transducers on the Olympus Panametrics-NDT Model 5800 Computer Controlled Pulser-Receiver

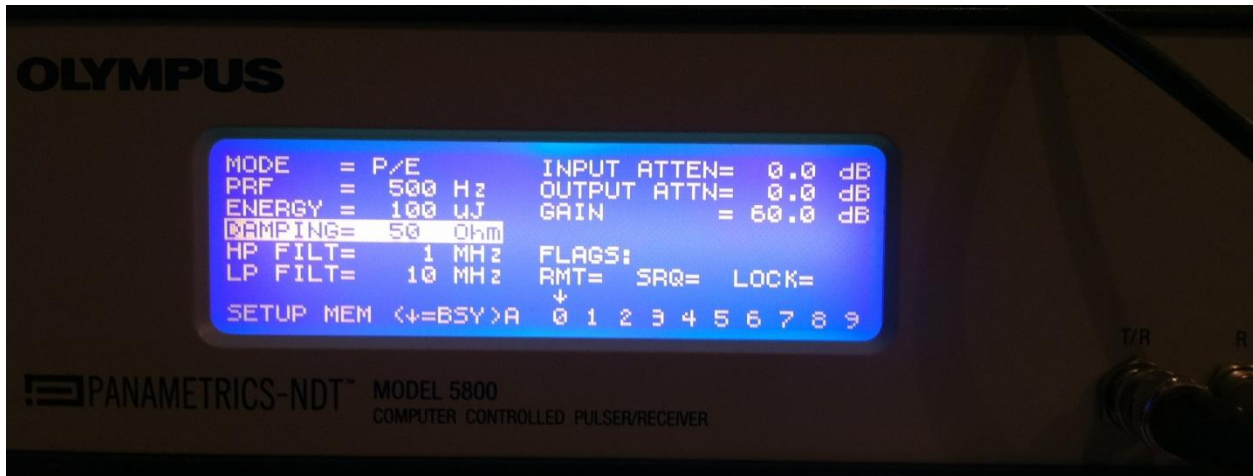


Figure #2.4: Example of settings used for single crystal transducers on the Olympus Panametrics-NDT Model 5800 Computer Controlled Pulsar-Receiver

To verify the transducer is providing a viable signal, the pulser-receiver is connected to an oscilloscope. This is an important step to take before proceeding to connect the transducer to the LabView system. The LabView system is comprised of a National Instruments NI PXI-1042Q operating system, a National Instruments NI PXI-5122 14-bit 100 MS/s Digitizer oscilloscope card, the LabView software, and a monitor to display the LabView program and oscilloscope.



Figure #2.5: Monitor connected to the National Instruments NI PXI-1042Q system



Figure #2.6: The National Instruments NI PXI-1042Q system, with NI PXI-5122 14-bit 100 MS/s Digitizer oscilloscope card and LabView software installed, used to take acoustic data during high temperature endurance run

2.1 Bismuth Titanate Testing (Sodium-modified)

The main characteristics of the sodium-modified bismuth titanate (K15) transducer are: piezoelectric sensitivity, $d_{33} = 20 \text{ pC/N}$, and resonant frequency (f_r) = 12.9 MHz.

This specimen was fabricated expressly for the purpose of high temperature endurance and performance evaluation. The transducer was rated to run up to 450 °C; therefore, the experimentation would be pushing the upper limits of the K15 transducer's performance rating.

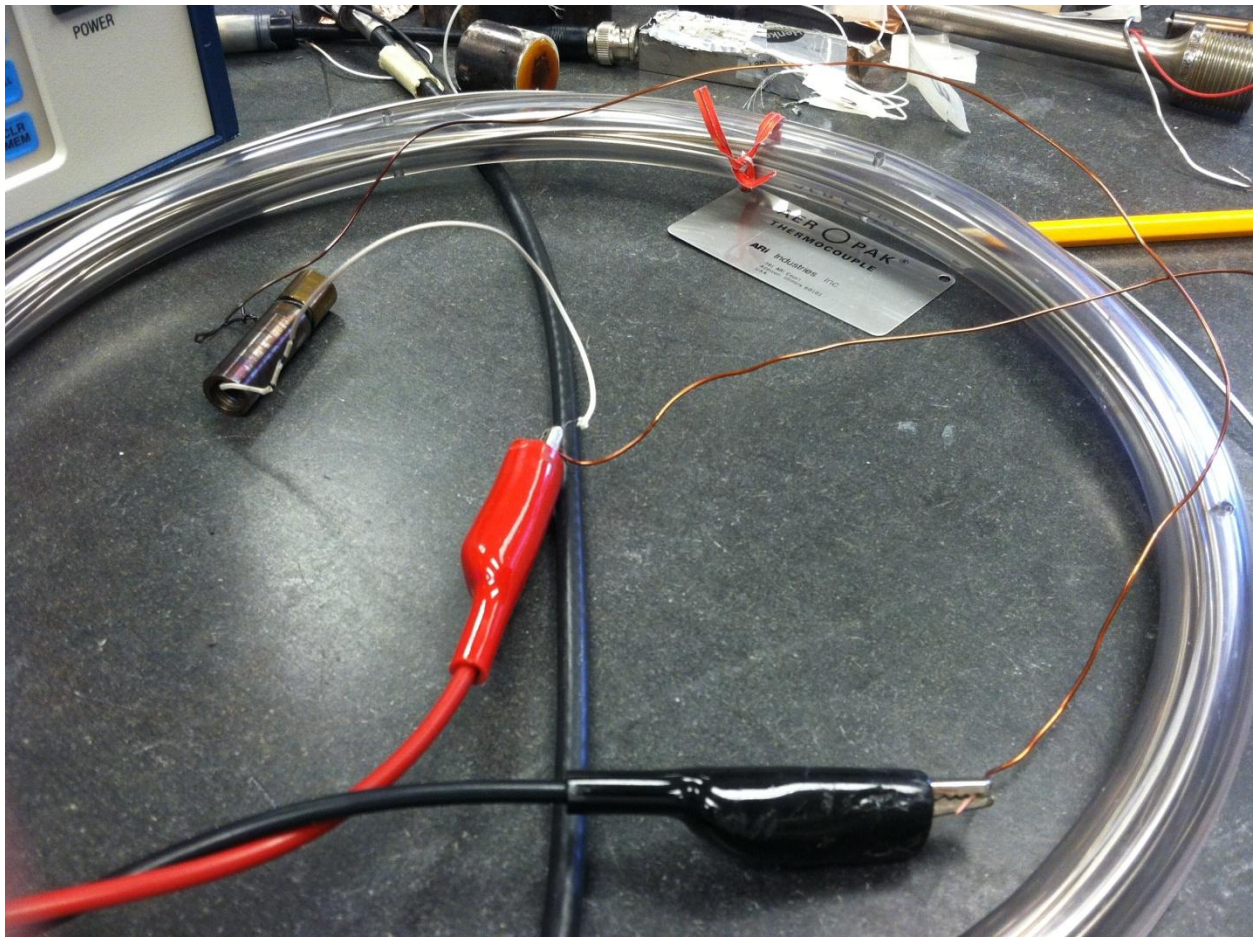


Figure #2.7: The connections made to the K15 bismuth titanate transducer for high temperature endurance and performance analysis

Above, Figure #2.7 shows the ground and lead wires attached to the K15 transducer. This was done to allow the alligator clips, which are not high temperature grade, to remain out of the furnace while the experiment was running. The lead and ground wires are both a copper-based wire which required sanding of the contact points to ensure proper conduction. The pulser-receiver settings were set at: 500 Hz pulse frequency, 100 μ J energy, 50 Ω damping, 1 MHz high pass filter, 10 MHz low pass filter, 10 dB fine attenuation, and 20 dB gain. Below in Figure #2.8 is an example of the analyzed segment of the pulse-echo response from the K15 transducer, constructed from a Matlab program code.

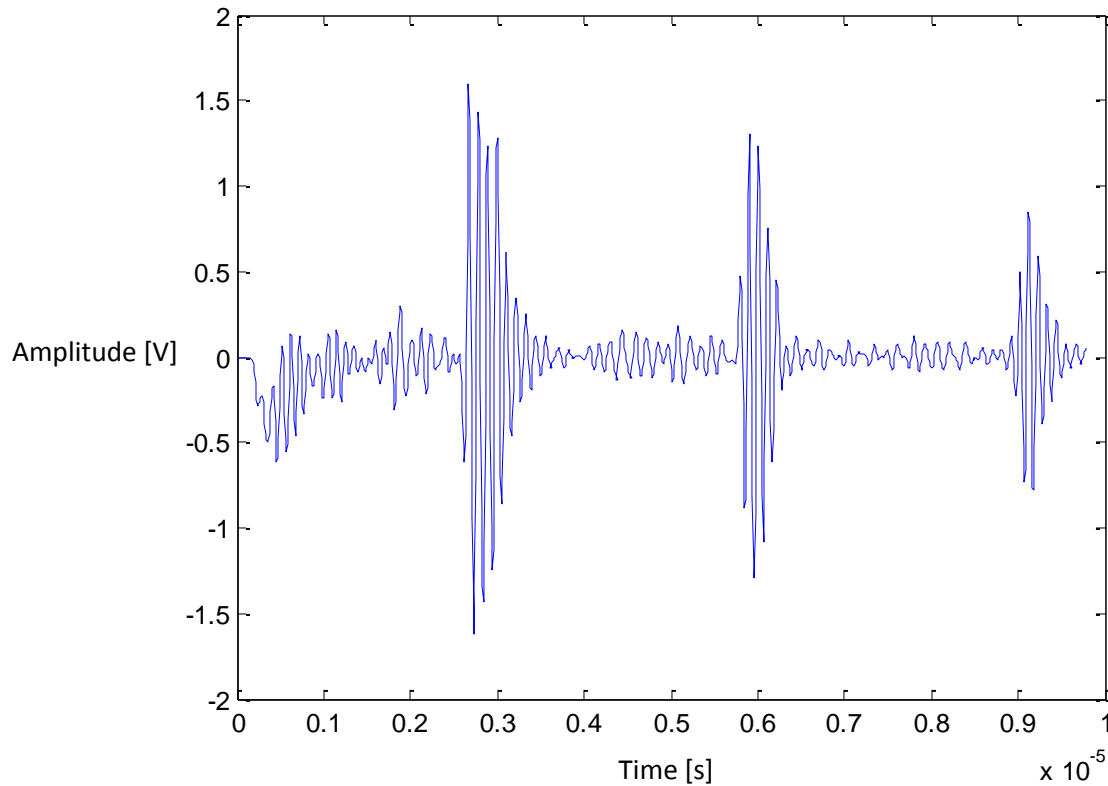


Figure #2.8: Analyzed segment of the initial pulse-echo signal amplitude response of the sodium-modified bismuth titanate transducer at room temperature

The space between signal peaks corresponds to the thickness of the waveguide based on a time-of-flight method assumption.

When the signal was analyzed using a Fast Fourier transform (FFT) in Matlab, the resonant frequency of the K15 sodium-modified bismuth titanate transducer came out to about approximately 9.1 MHz from nearly equivalent resonance peaks as seen in Figures #2.9 and #2.10.

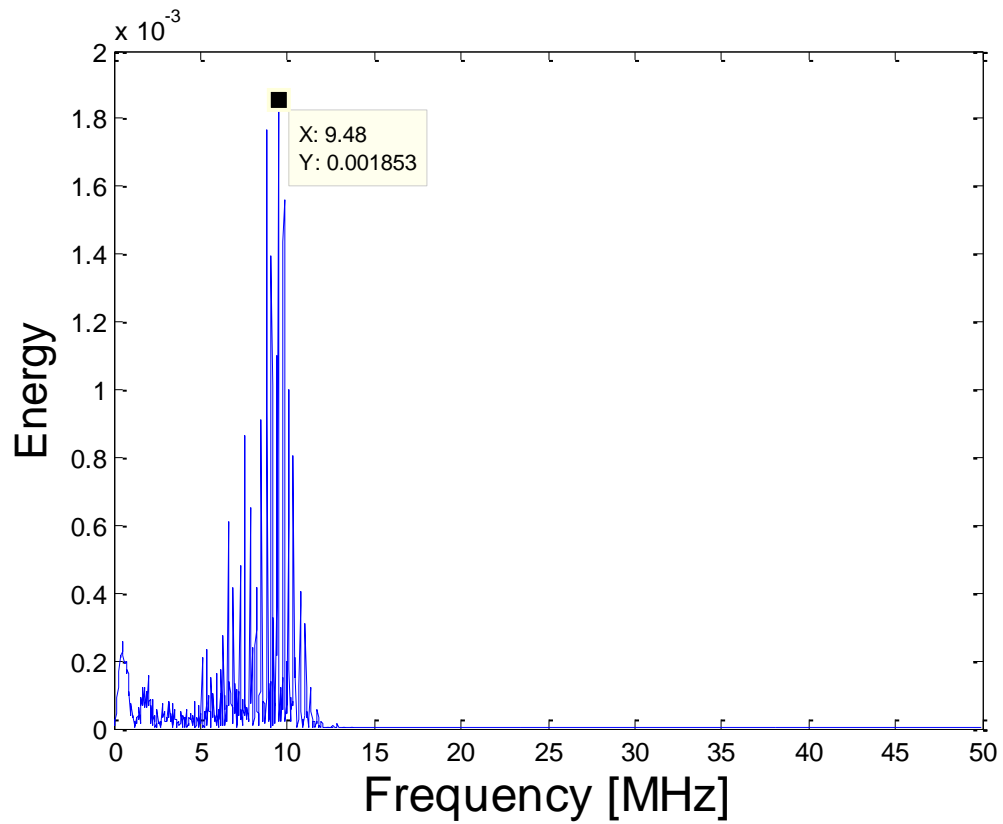


Figure #2.9: Plot of the FFT analysis of the initial K15 transducer signal with an arrival time of $2.7 \mu\text{s}$ within a $25 \mu\text{s}$ window length

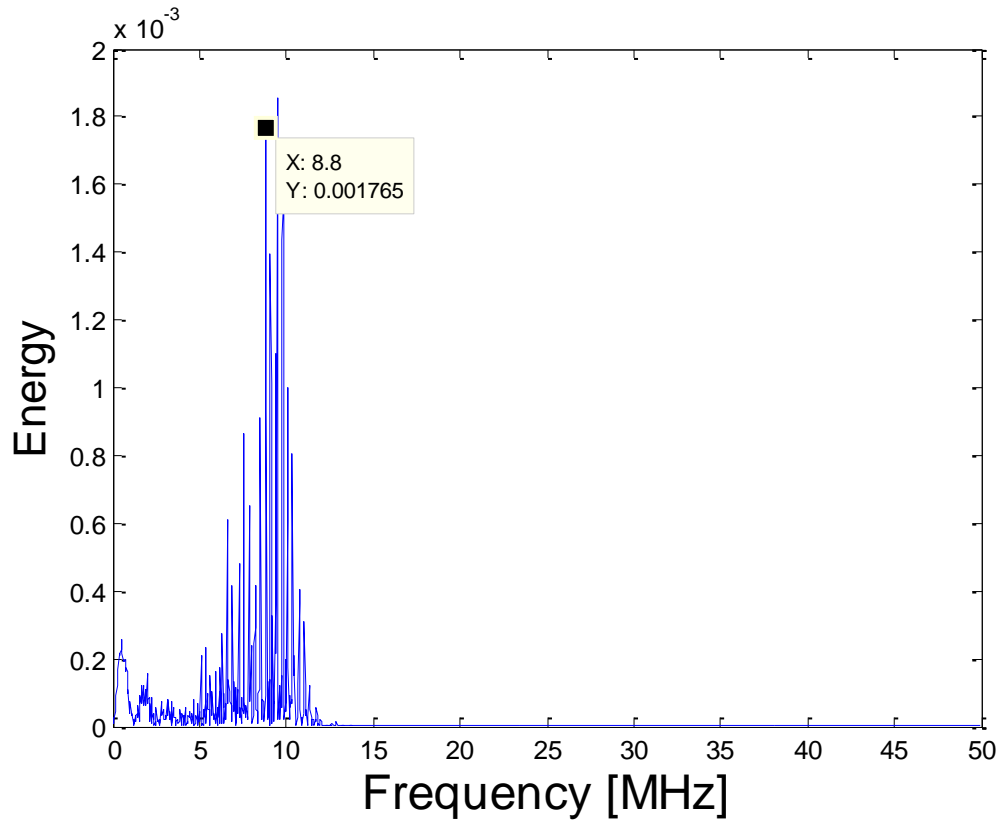


Figure #2.10: Plot of the FFT analysis of the initial K15 transducer signal with an arrival time of 2.6 μs within a 25 μs window length

Due to extenuating circumstances beyond the author's control, the endurance test was broken up into three separate segments as seen below in figures #2.11-2.16 and those results were compiled into a full endurance test plots as seen in figures #2.17 and 2.18. Each segment as well as the full temperature test will be plotted first as the raw amplitude data and secondly as the relative amplitude data (amplitude ratio relative to initial amplitude signal).

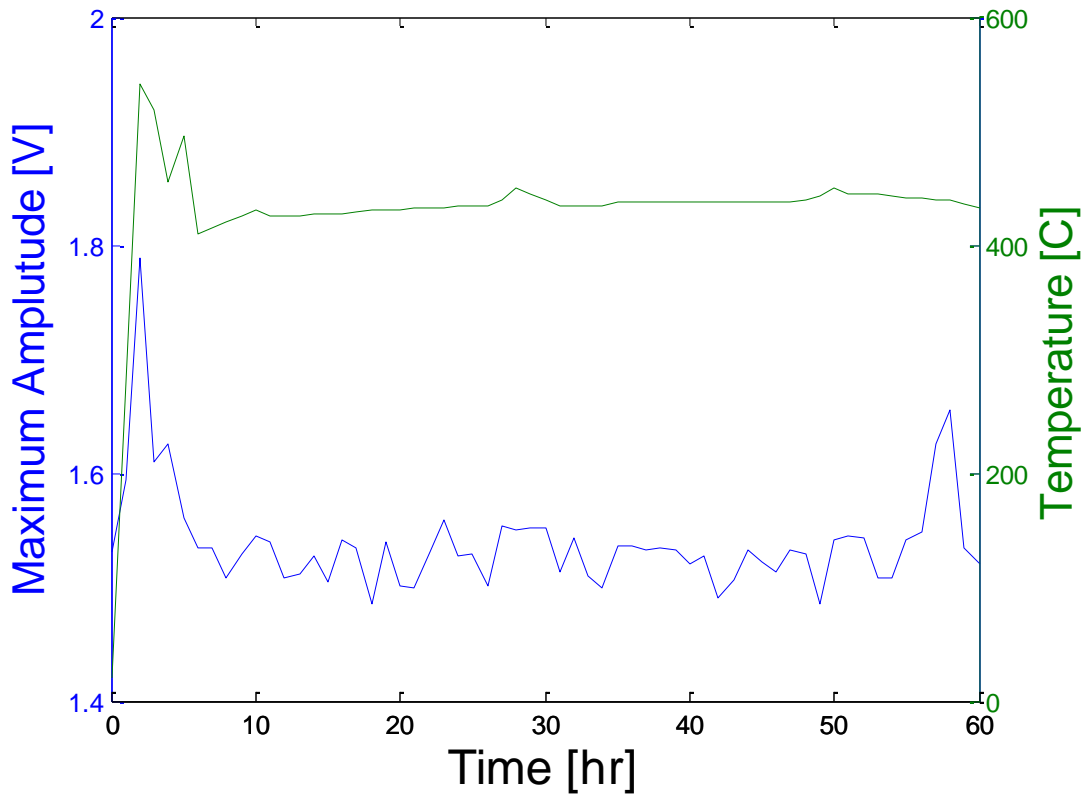


Figure #2.11: Graph of segment 1 maximum raw amplitude data (blue) and temperature (green) versus time

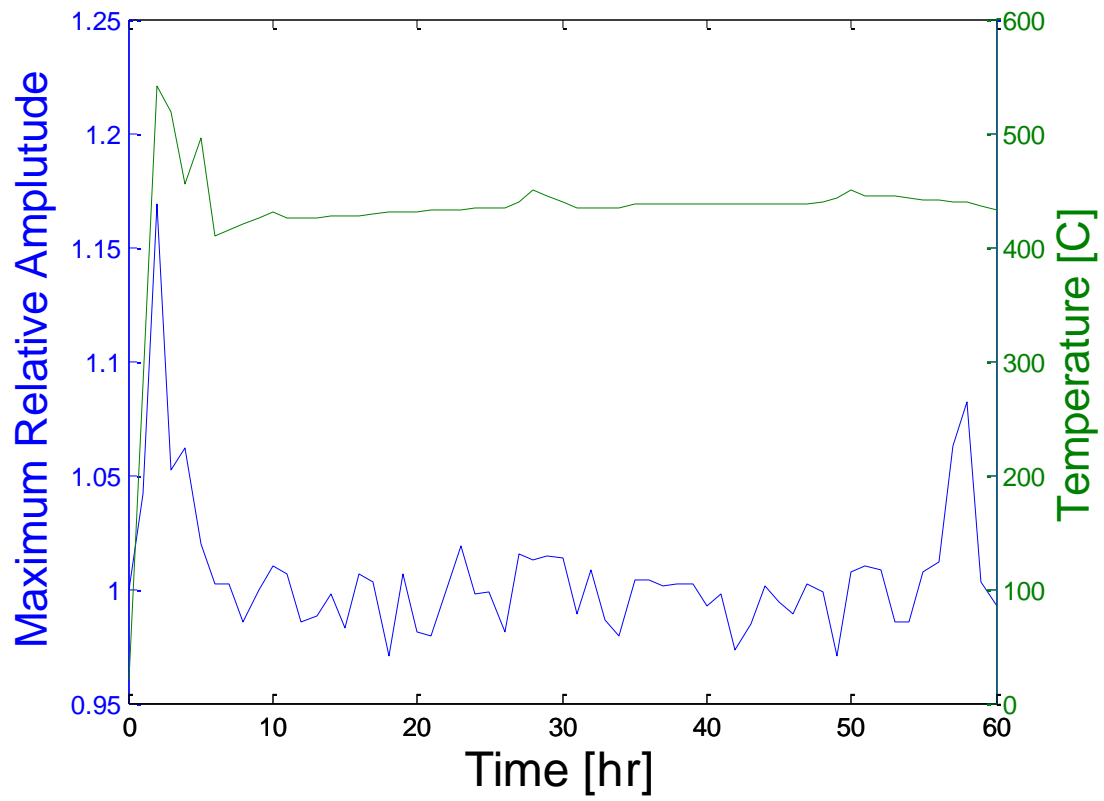


Figure #2.12: Graph of segment 1 maximum relative amplitude (blue) and temperature (green) versus time

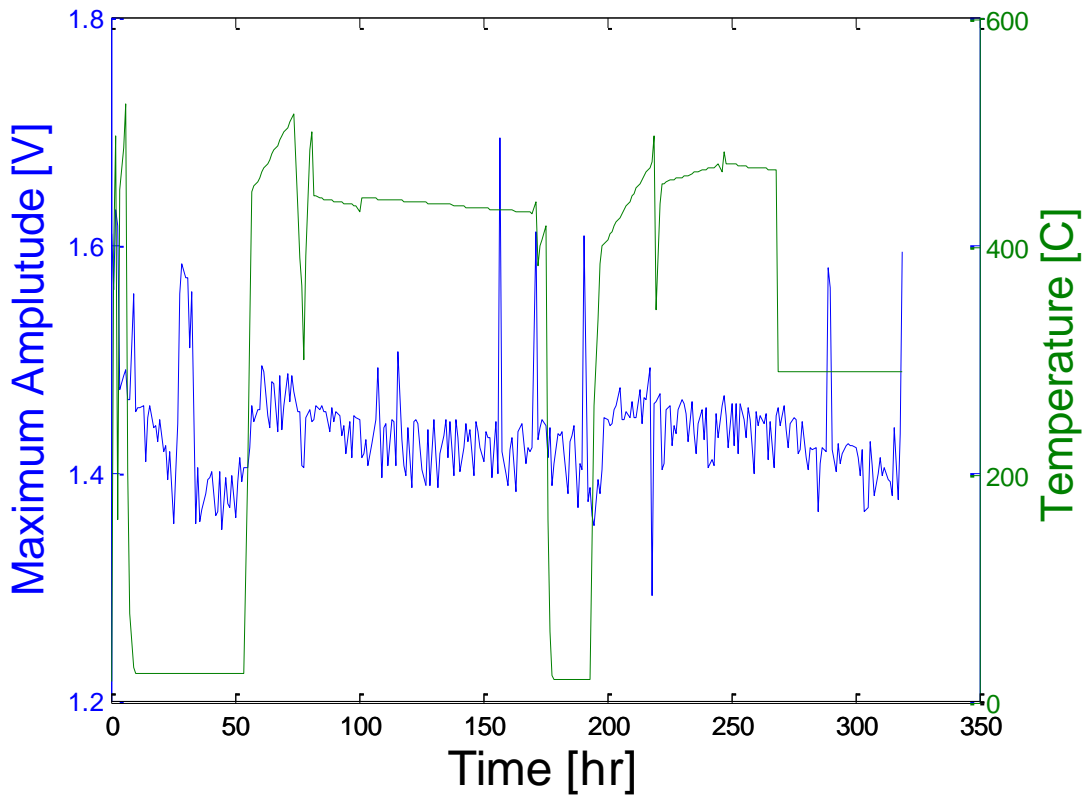


Figure #2.13: Graph of segment 2 maximum raw amplitude (blue) and temperature (green) versus time

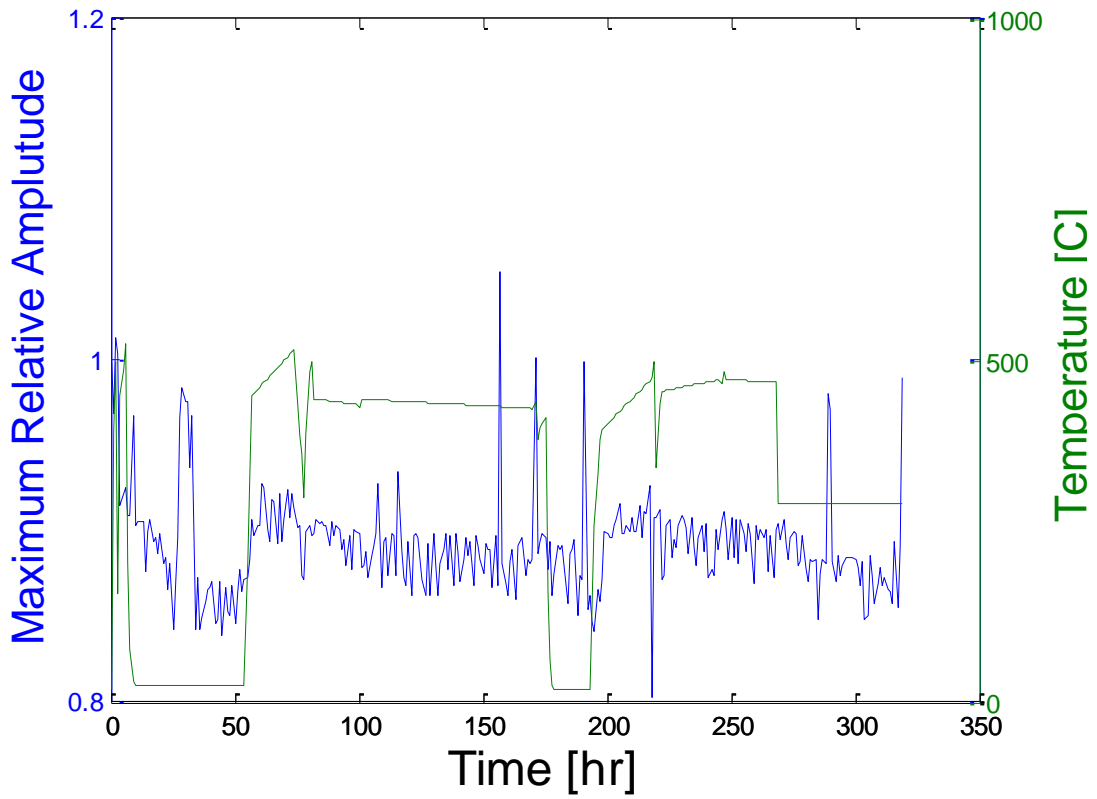


Figure #2.14: Graph of segment 2 maximum relative amplitude (blue) and temperature (green) versus time

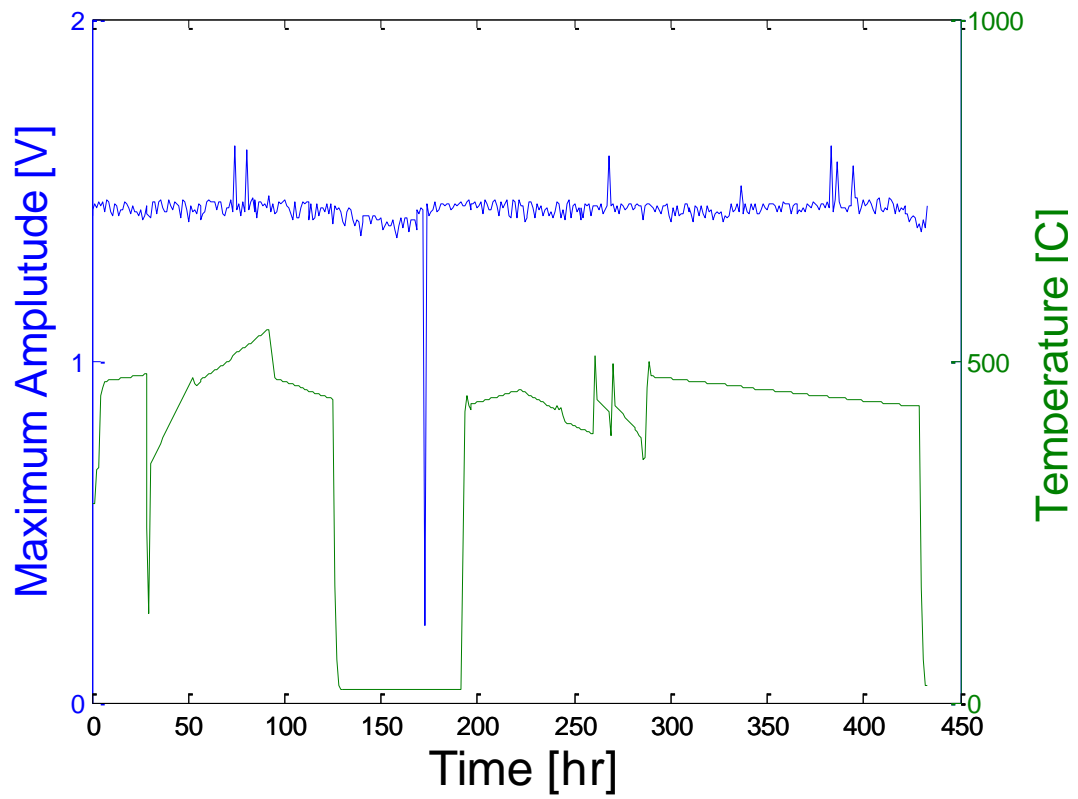


Figure #2.15: Graph of segment 3 maximum raw amplitude (blue) and temperature (green) versus time

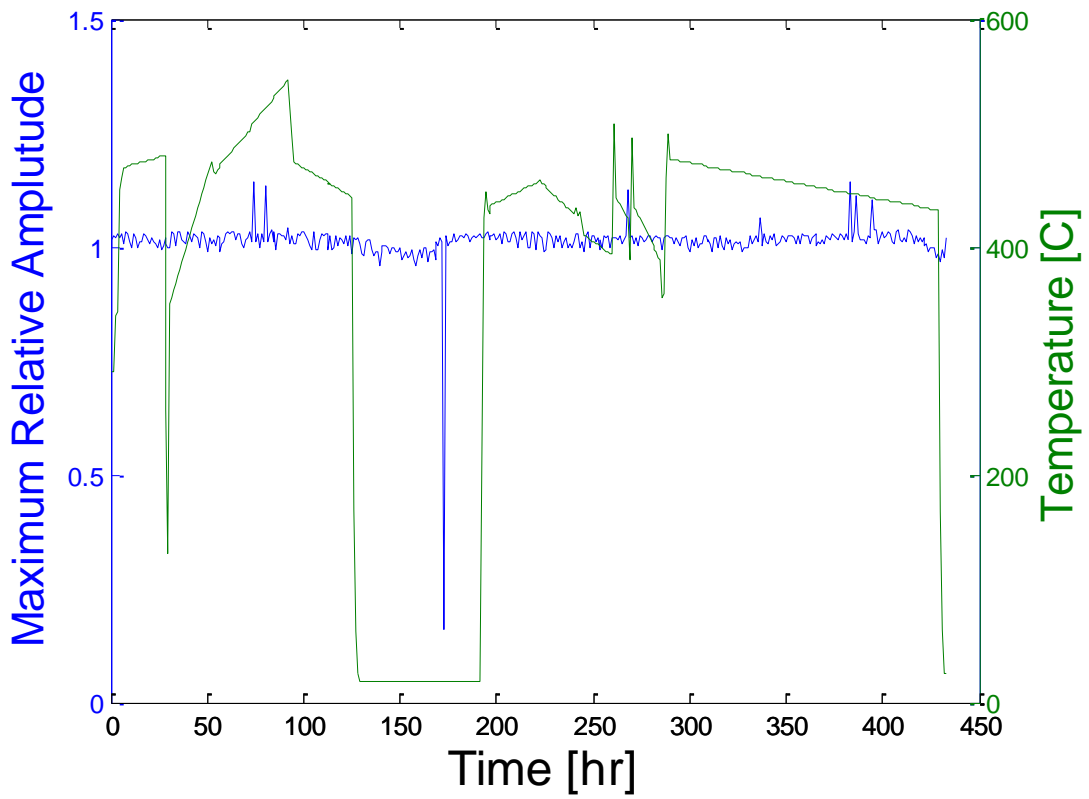


Figure #2.16: Graph of segment 3 maximum relative amplitude (blue) and temperature (green) versus time

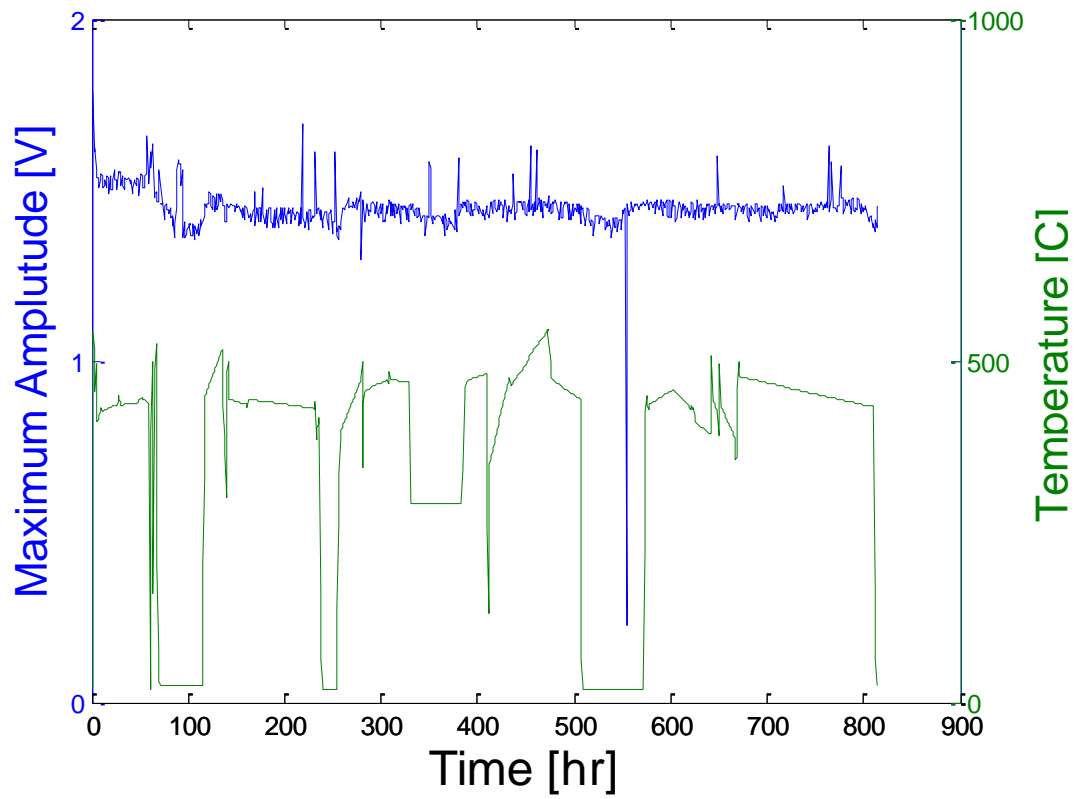


Figure #2.17: Full high temperature endurance test of the K15 transducer, graphing raw amplitude (blue) and temperature (green) over time

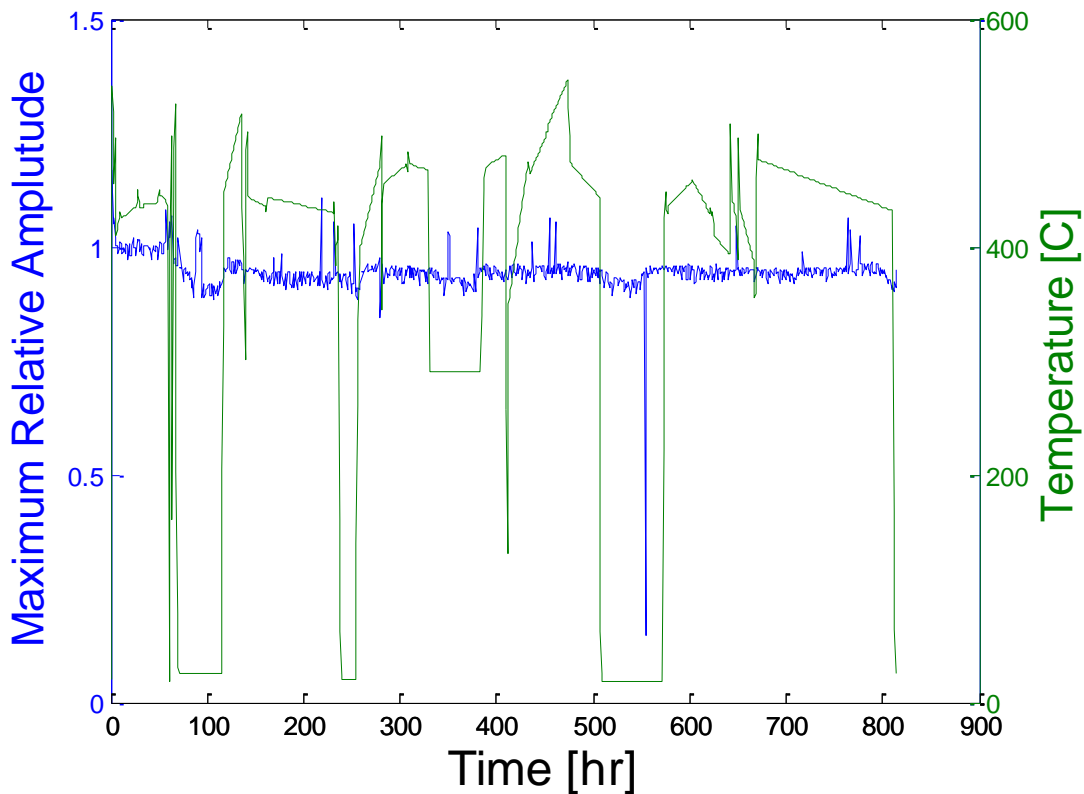


Figure #2.18: Full high temperature endurance test of the K15 transducer, graphing relative amplitude (blue) and temperature (green) over time

The only notable degradation of the K15 bismuth titanate transducer signal during the entirety of the endurance test occurred when the wires connected to the transducer became crossed, nearly causing the signal to completely short circuit. There was a notable spike in max amplitude near beginning of the test, at the end of segment 1, despite the temperature remaining level. The acoustic signal from the transducer remained fairly steady through the temperature fluctuations. Taking all three segments together, the K15 transducer holds more than sufficiently steady throughout an approximately five to six week period mainly at a temperature of ~430-450 °C.

Throughout the test, it was clear that the furnace is notoriously difficult to keep at temperature for longer than a week without close supervision which would be difficult to accomplish without making the lab a near permanent residence. However, this is not an unwanted occurrence given that the test was meant to mimic nuclear reactor test conditions which includes start ups and shut downs.

2.2 Aluminum Nitride Testing

The main endurance testing on aluminum nitride was run with a piezoelectric element which possesses a d_{33} of approximately 4, and a resonance frequency of approximately 12.7 MHz based on an element thickness of 0.4 mm.

$$f_r = \frac{v_m}{2t_m} \quad (\text{Eqn. 2.3})$$

Where f_r is resonant frequency, v_m is the sound velocity in the given material, and t_m is the thickness of the material

The pulser-receiver settings were set at: 500 Hz pulse frequency, 100 μ J input energy, 50 Ω damping, 1 MHz high pass filter, 10 MHz low pass filter, 8 dB fine attenuation, and 60 dB gain.

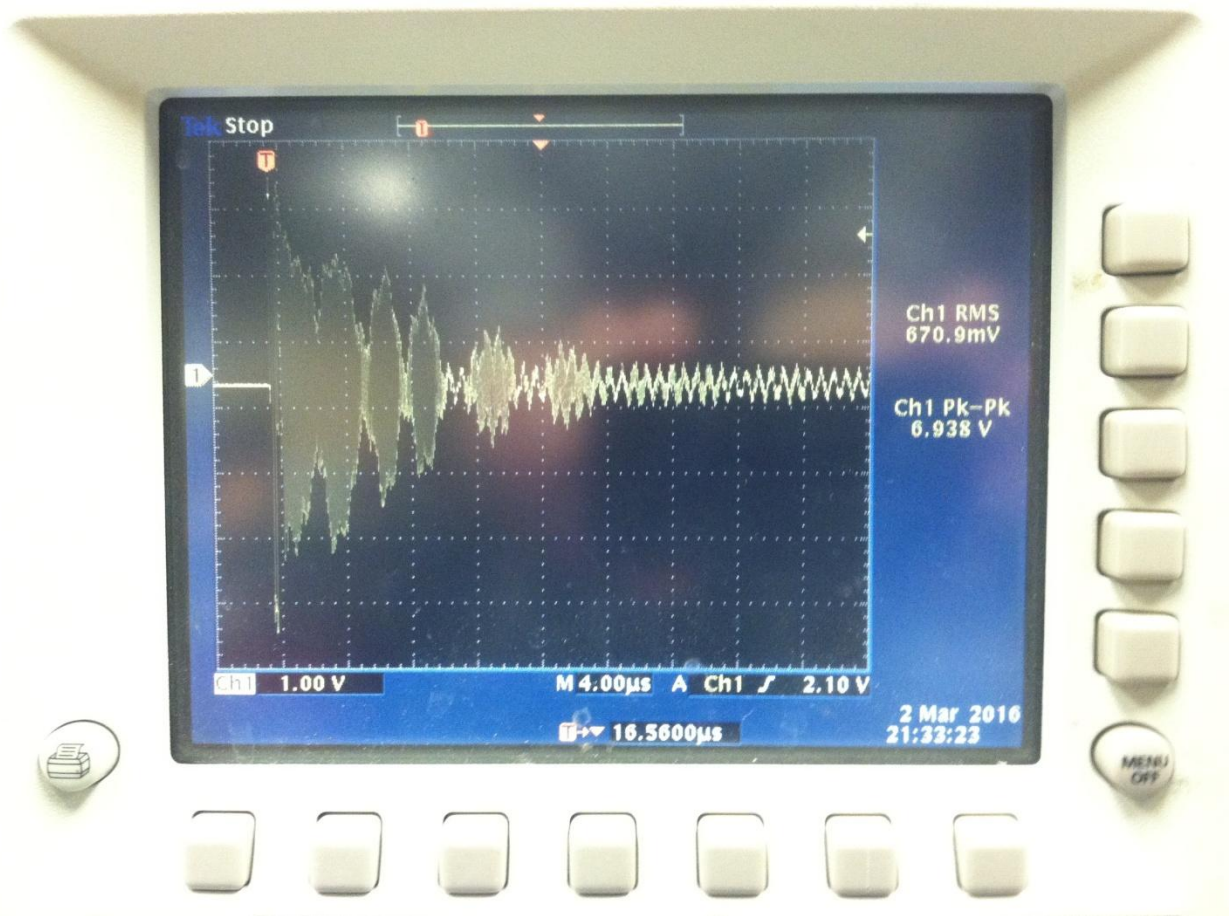


Figure #2.19: Oscilloscope display showing pulse-echo amplitude signal from the aluminum nitride transducer prior to endurance testing

Figures #2.19 and #2.20 show the initial signal from the aluminum nitride transducer prior to the high temperature endurance test.

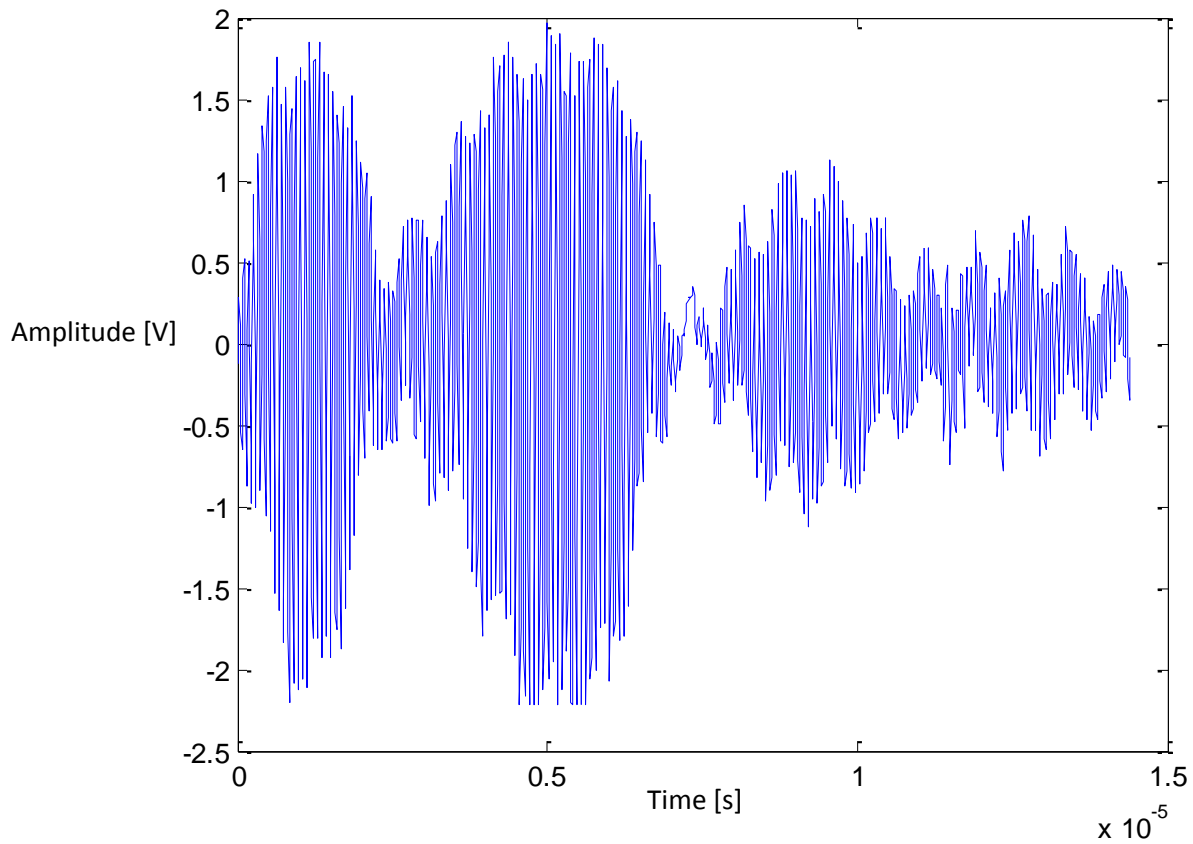


Figure #2.20: Analyzed segment of the initial pulse-echo amplitude response of the aluminum nitride transducer at room temperature

As mentioned above, the calculated value of the resonant frequency for the aluminum nitride transducer is approximately 12.7 MHz. The initial signal from the aluminum nitride transducer was run through a Fast Fourier transform in Matlab. The plot can be seen in Figure #2.21.

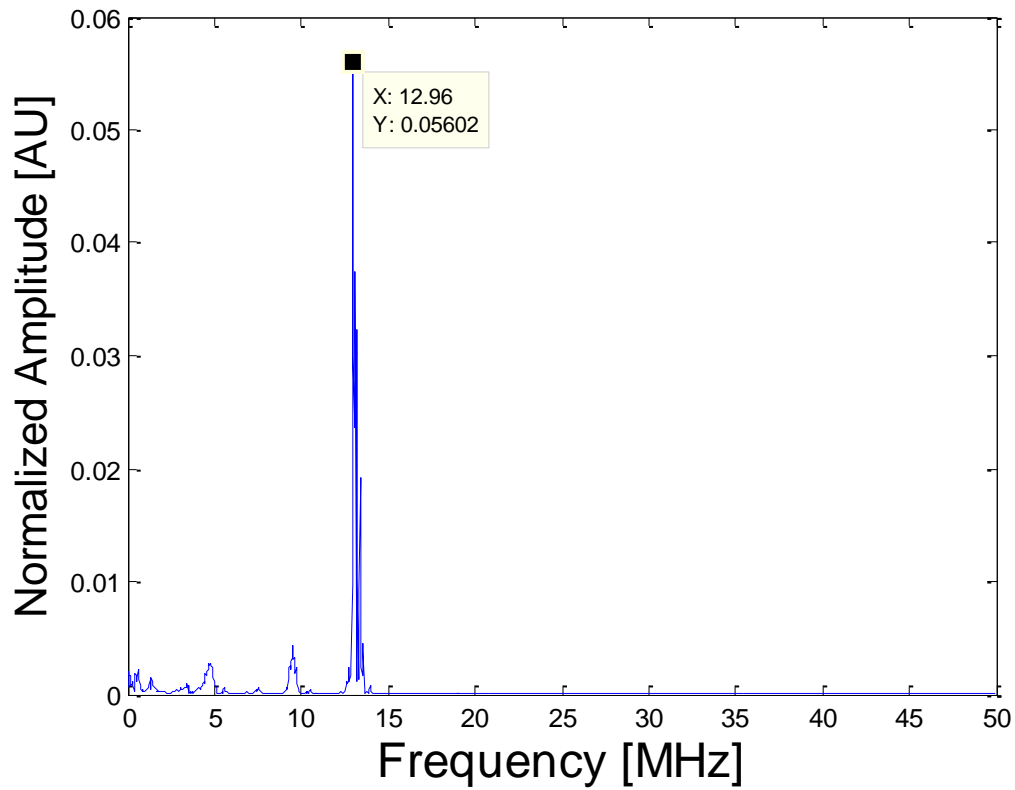


Figure #2.21: Plot of the resonance peak from the FFT analysis of the initial aluminum nitride transducer signal

The FFT analysis of the signal produced a resonance peak at around 12.9 MHz which correlates well with the calculated value.

Thus, the high temperature endurance test began on the aluminum nitride single crystal transducer. The plots of the transducer performance as a function of temperature over time can be seen in figures #2.22 and #2.23.

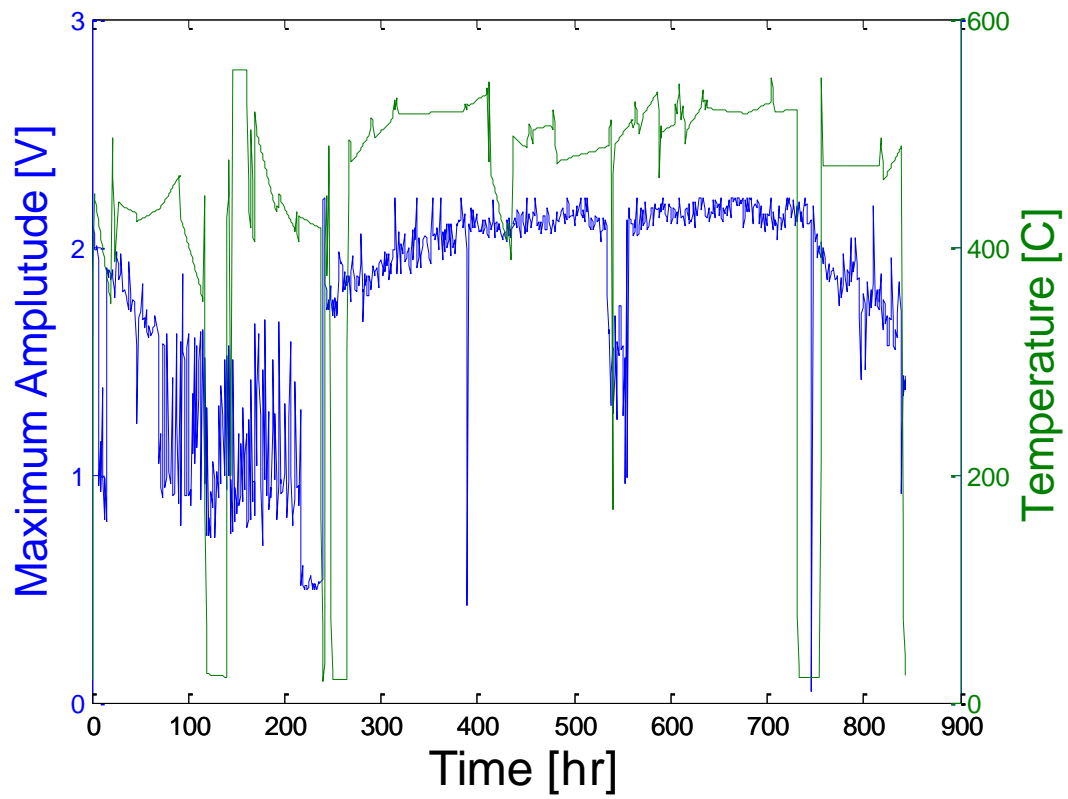


Figure #2.22: Full high temperature endurance test of the aluminum nitride transducer, graphing maximum amplitude (blue) and temperature (green) versus time

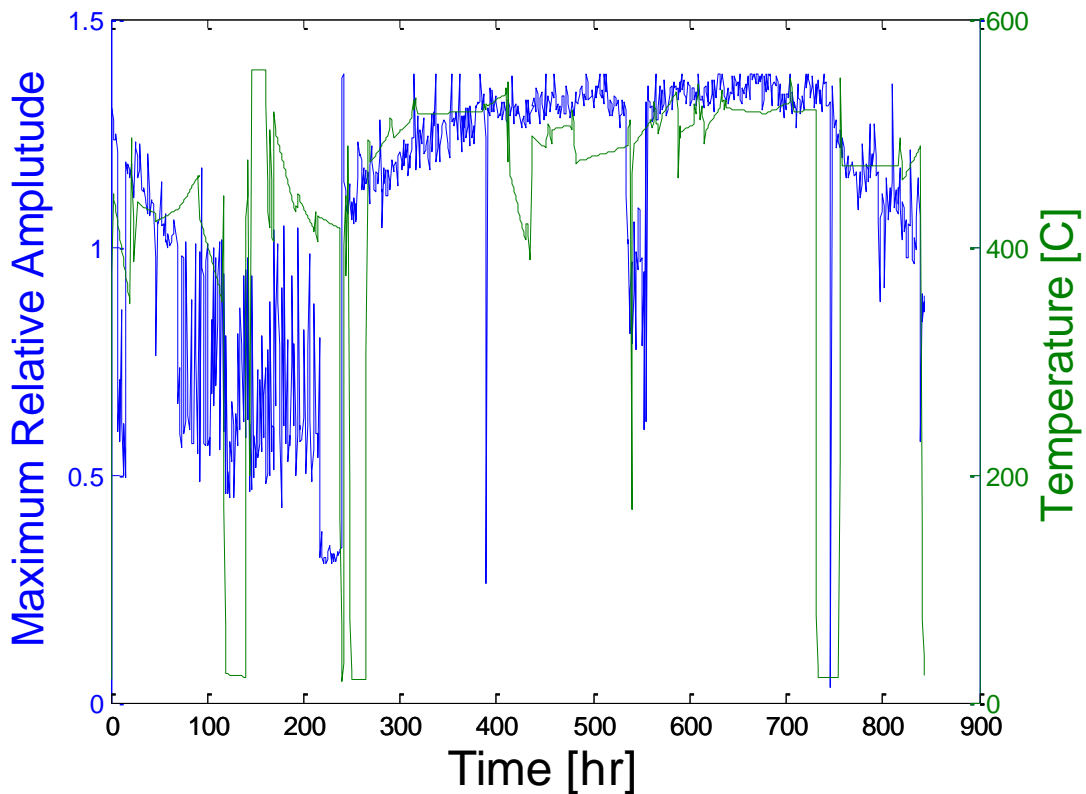


Figure #2.23: Full high temperature endurance test of the aluminum nitride transducer, graphing maximum relative amplitude (blue) and temperature (green) versus time

Some physical processing of the sample was taken using a scanning electron microscope. Below are a couple of scanning electron microscope images to illustrate the low surface roughness of the aluminum nitride substrate. One image is taken at 500x magnification (Figure #2.25), while the other is taken at 2000x magnification (Figure #2.24). A low surface roughness is important in making the best possible contact necessary for acoustic transmission between piezoelectric element and waveguide as well as piezoelectric element and backing.

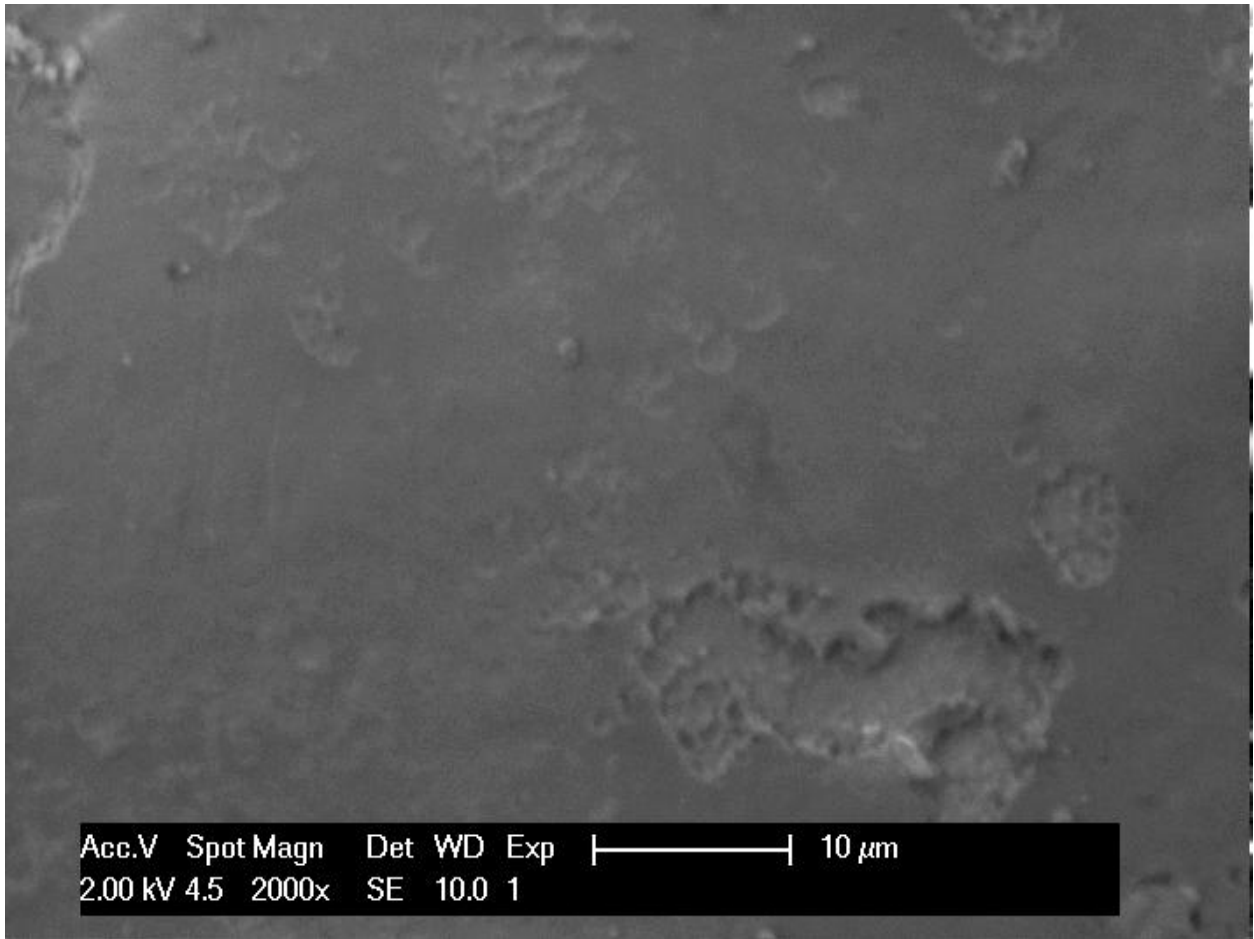


Figure #2.24: SEM image of the aluminum nitride sample at 2000x magnification

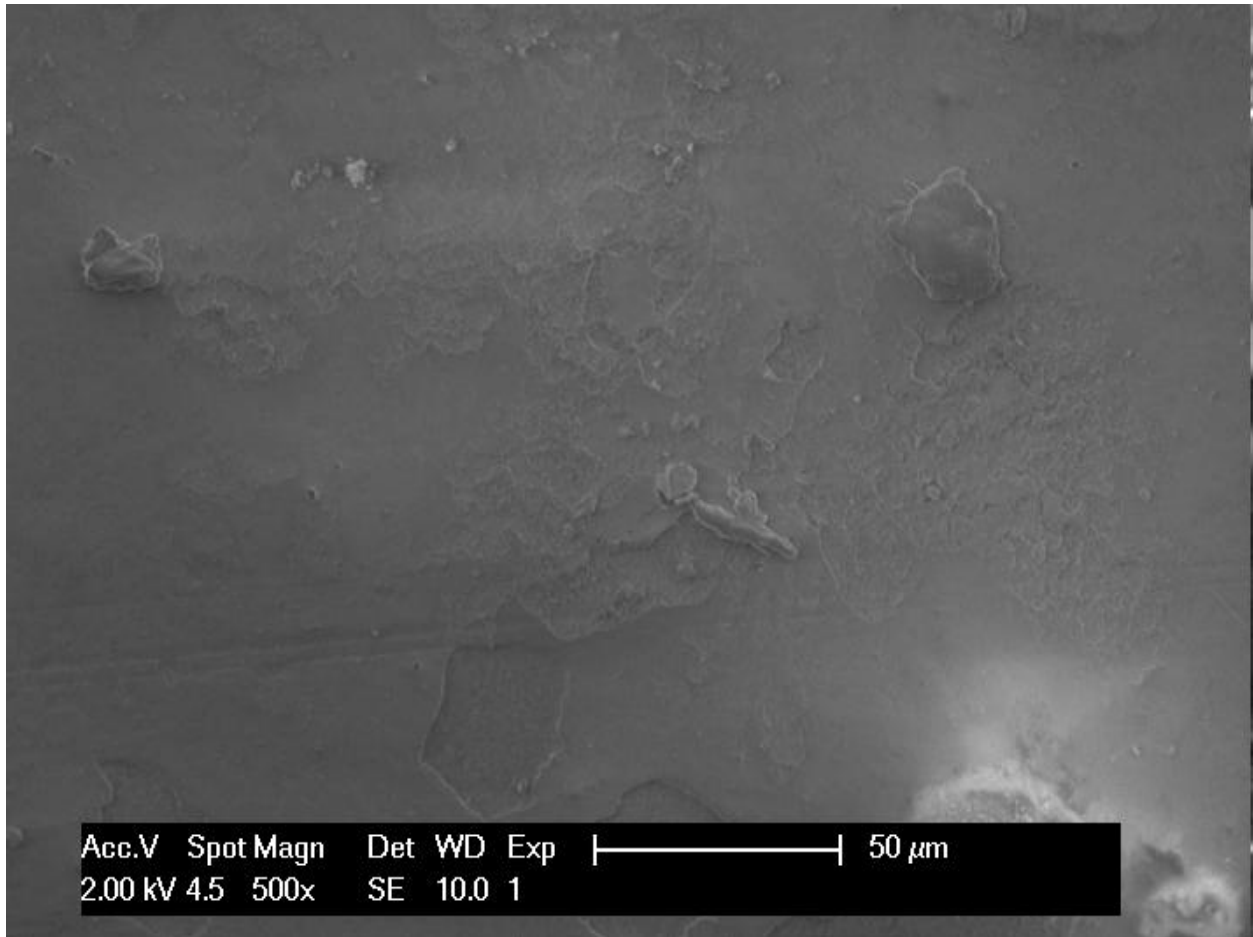


Figure #2.25: SEM image of the aluminum nitride sample at 500x magnification

It would be prudent to explain the unexpected degradation of the amplitude signal of the aluminum nitride transducer. The initial degradation from about hour 70 through hour 240, and particularly between approximately hours 210 and 240, can be explained by an electronics issue caused by improper triggering in the acoustic signal. The trigger function of an oscilloscope stabilizes repetitive waveforms, allowing for more accurate analysis of received signals. When this function is not properly employed, signals as in Figures #2.26 and #2.27 below are the result.

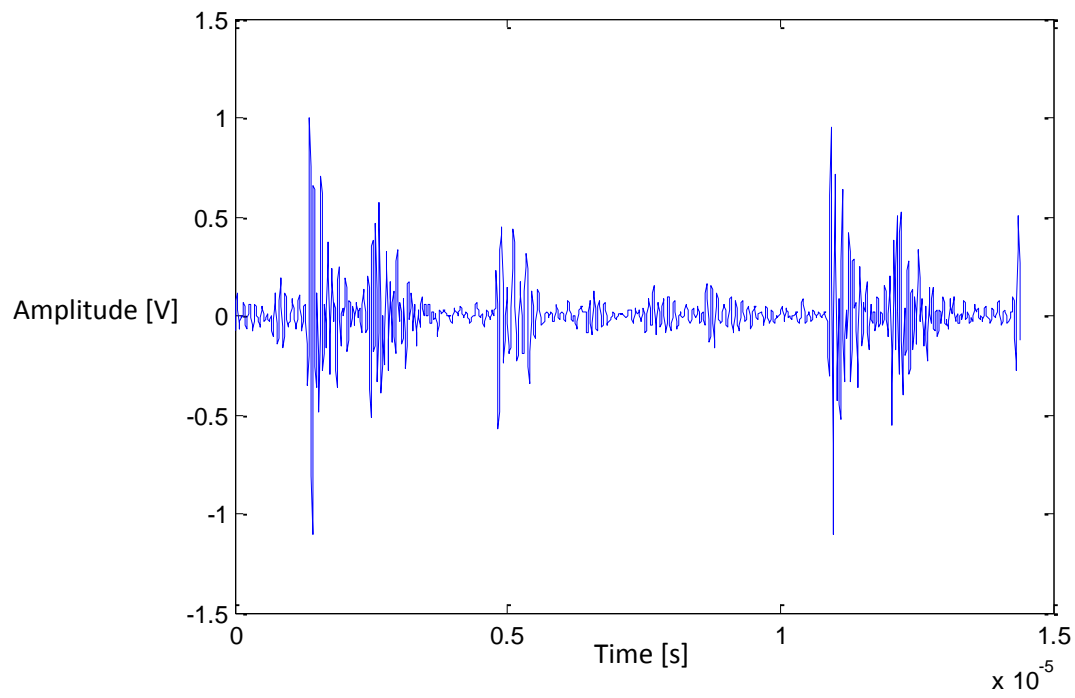


Figure #2.26: Example of an improperly triggered signal from the initial signal degradation in the aluminum nitride endurance test

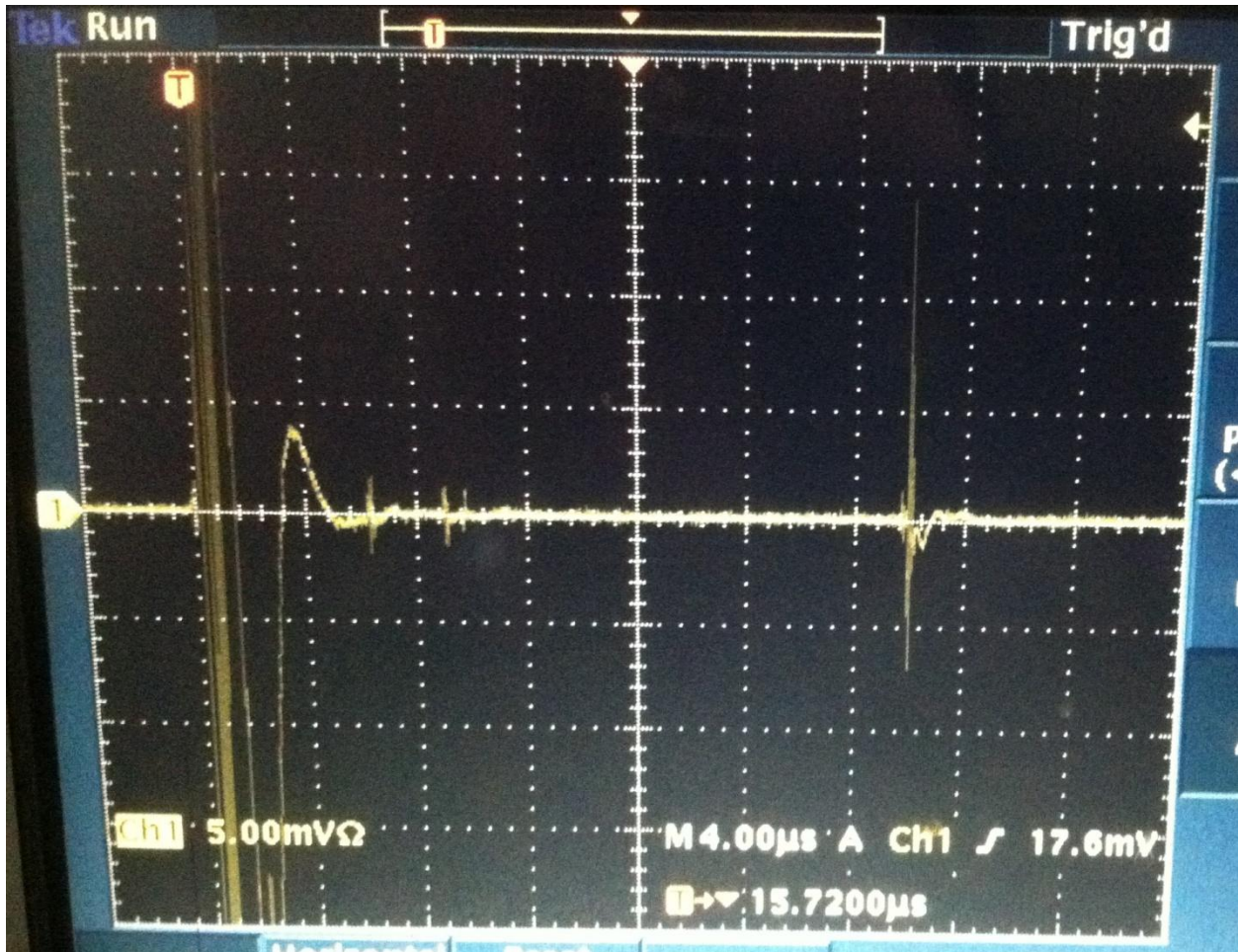


Figure #2.27: Oscilloscope display of an improperly triggered aluminum nitride transducer signal

The signal degradation that can be observed near the end of the high temperature endurance test, albeit small in comparison to the initial degradation of the signal, is due in large part to the breakdown of the backing material. In a non-inert environment, carbon is susceptible to interaction with oxygen at high temperatures. When this occurs, the elemental carbon in the composite matrix slowly begins to burn out. Once the burn out is complete, the only remnant of the carbon-carbon composite matrix is the carbon fibers that were woven together within the elemental carbon. This is a primary reason why there is to be a preliminary search for a replacement for carbon-carbon as a backing material for non-inert environments, possibly inert environments as well assuming that this new backing material possesses properties of equivalent or higher value to the performance and efficiency of the bulk single crystal transducer system.

Figure #2.28 below illustrates the end result of the non-inert environment breakdown of the carbon-carbon composite.



Figure #2.28: Displaying breakdown of carbon-carbon backing after long term high temperature exposure

Besides these noted degradations of the amplitude signal, the aluminum nitride piezoelectric element performed well over the course of the high temperature endurance test, even seeing an improvement in its relative amplitude signal for a good portion during the middle of the experiment.

Next, several viability studies will be performed on a few different single crystals of aluminum nitride to determine their potential for future high temperature endurance testing.

2.2.1 HT-series Aluminum Nitride High Temperature Viability Studies

Three additional aluminum nitride crystals (HT-2412, HT-2572, and HT-2902) were provided for endurance and performance testing. Each sample possessed a d_{33} of approximately 4 pC/N, when tested on an APC International YE2730A Piezo d_{33} Test System, prior to any cutting or heat treatment. The first construction (and first attempt) of the HT-2412 was run with pulser-receiver settings of 40 dB gain while every other attempt was run with pulser-receiver settings of

60 dB gain and 10 dB attenuation on the Olympus Panametrics-NDT Model 5800 Computer Controlled Pulser-Receiver.

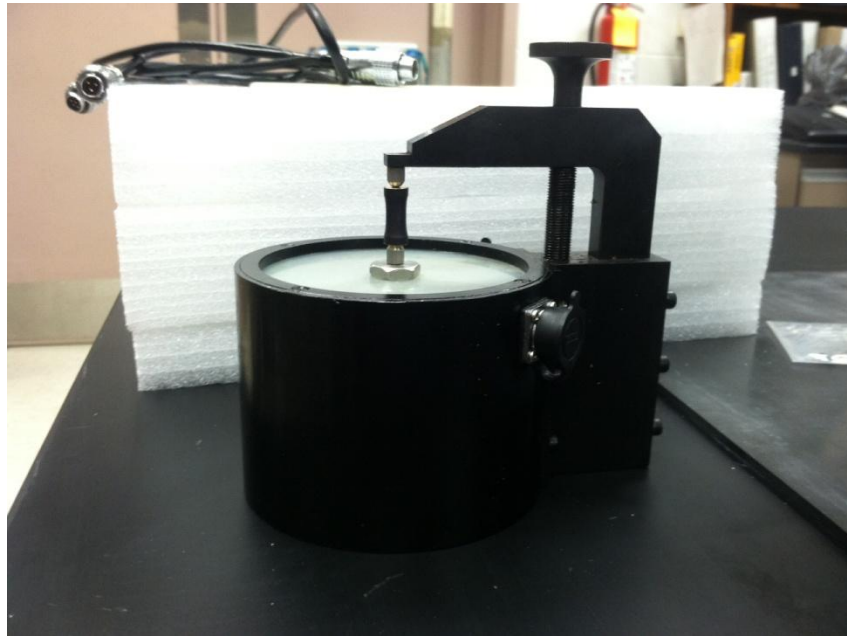


Figure #2.29: APC International YE2730A Piezo d_{33} meter with test piece



Figure #2.30: Power supply and display for APC International YE2730A Piezo d_{33} meter

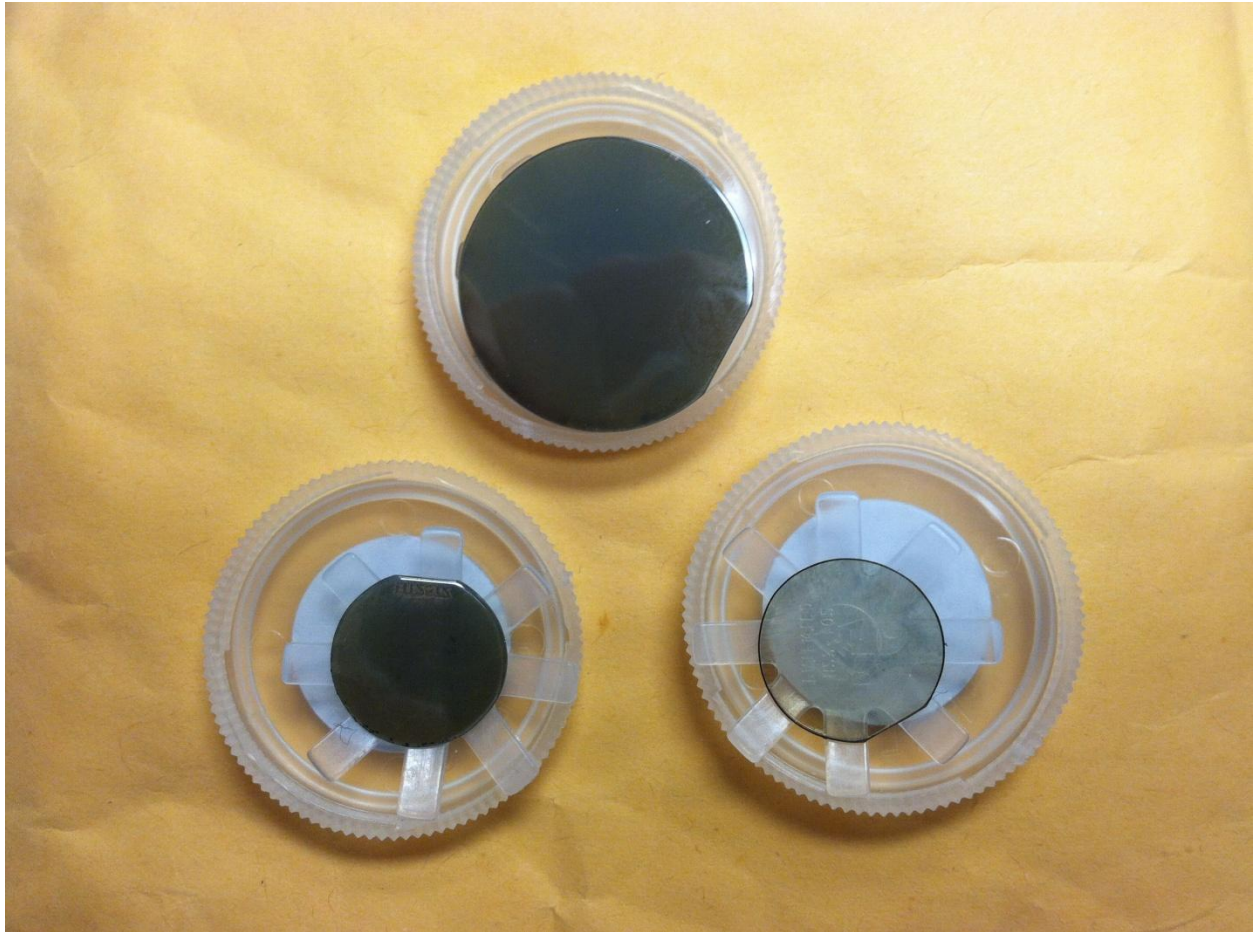


Figure #2.31: HT wafers in their pre-cut, pre-heat treatment form, (top) HT-2902, (bottom left) HT-2572, (bottom right) HT-2412

HT-2412

Six separate attempts were made to get this particular crystal to work (since it was made known to the author that this sample would be the most likely candidate of the three to perform at high temperatures), none of which proved successful above approximately 350 °C. The first attempt was made with a different construction than attempts 2-6 as will be enumerated below.

Construction #1 (Attempt 1): A magnetic steel substrate was employed as a waveguide. A layer of Cotronics epoxy was applied as coupling, followed by a HT-2412 shard, and a gold electrode. The sample was cured as instructed by the epoxy's packaging. Next, a copper lead of a thermocoax cable was woven through a copper mesh. Silver paste was applied to keep contact and allowed to air dry for approximately two hours. The mesh was then placed onto the electrode and another coating of the epoxy was applied, curing as instructed. The sample was placed into

the furnace once the received signal from shard was established. The temperature was slowly ramped up from room temperature. The signal received from the shard initially increased before dropping sharply at around 200 °C. The signal was no longer present overnight at a temperature around 390 °C; visual inspection upon cooling of the furnace and subsequent removal of the construction from within showed that the epoxy had burned completely off leaving the system unconnected.

Construction # 2 (Attempts 2-6): The housing construction that has proved successful in past applications for aluminum nitride testing as well as reactor testing was employed for the remaining attempts. Within the stainless steel casing from the bottom are: a high temperature spring, a kovar waveguide, aluminum foil coupling, Aremco binder, a HT-2412 round sample, Aremco binder, carbon-carbon backing, nickel plunger, and stainless steel cap (with alumina shielding and insulation around a number of the previous elements). A copper lead was attached directly to the tip of the plunger (where a very small hole was drilled previously by the machine shop) using the strain relief gauge to stabilize the wire. A signal received from the sample was established before it was placed into the furnace. The first attempt with this construction barely reached 200 °C before signal disappeared; the furnace was allowed to cool back to room temperature and the signal recovered. The second attempt produced essentially same result as the first, the signal once again recovering once the furnace was allowed to cool. The signal in the third attempt remained in working order up to around 350 °C before the signal rapidly disappeared, once again recovering upon cooling of the furnace. The fourth attempt proceeded in the same vein as the third, signal remaining viable up to around 350 °C before dropping sharply, disappearing almost completely at around 420 °C. The final attempt unfortunately produced the same result as the previous ones, able to reach a slightly higher temperature of about 360 °C before the drop occurred.

HT-2572

I used the same housing construction as attempts 2-6 of the HT-2412 for this test. This different form (darker in color and opaque to the eye) of aluminum nitride produced nearly the same result as its lighter and translucent counterpart. The signal was strong up to around 310 °C, even producing more echoes starting around 220 °C. However, the same signal degradation

began to occur at approximately the 360 °C mark with the signal unable to be distinguished from the noise at around 410 °C.

HT-2902

Once again, the same housing construction as previous tests was employed. Similar in color and clearness as the HT-2572, this form of aluminum nitride produced the most promising results. The signal held strong with very little degradation of the initial signal up to 495 °C when it was left in the furnace for an overnight stay. Upon return, the temperature had risen to 550 °C and the signal had degraded approximately 50%, but this is far better than any of the other tests we had run prior. Interesting note, upon visual inspection after cooling the furnace and removing the transducer from its confines, the crystal itself appears to have changed color from brown to pink.

The color change in the crystal prompted an investigation into the surface topology as well as the atomic content of the crystal itself. This was performed using, first, Scanning Electron Microscopy (SEM) and, secondly, Electron Deflection Spectroscopy (EDS). Each technique was employed on two samples: one which was non-heat treated; while the other was heat treated (and is now subsequently colored a pink-purple hue).

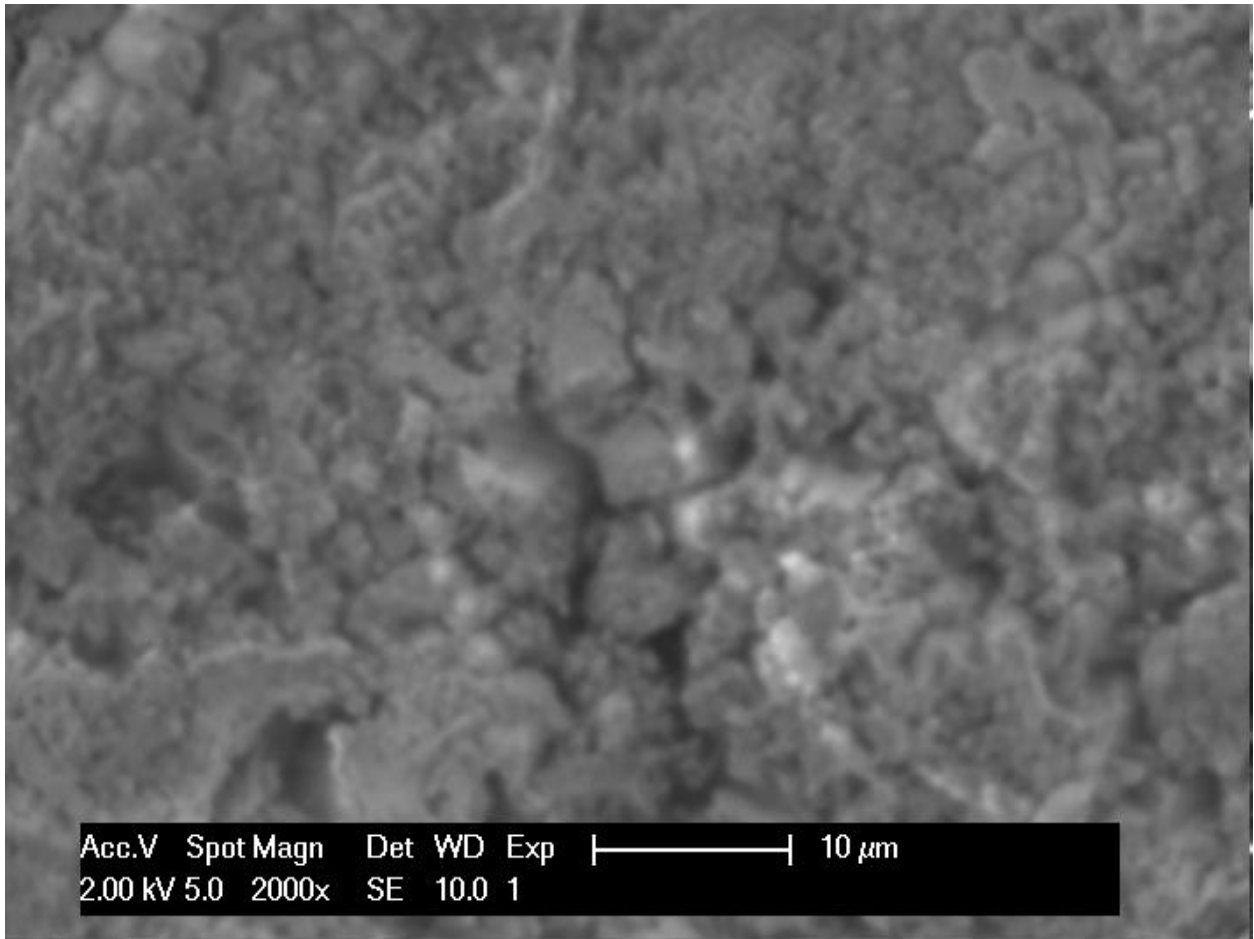


Figure #2.32: SEM image of non-heat treated HT-2902 at 2000x magnification

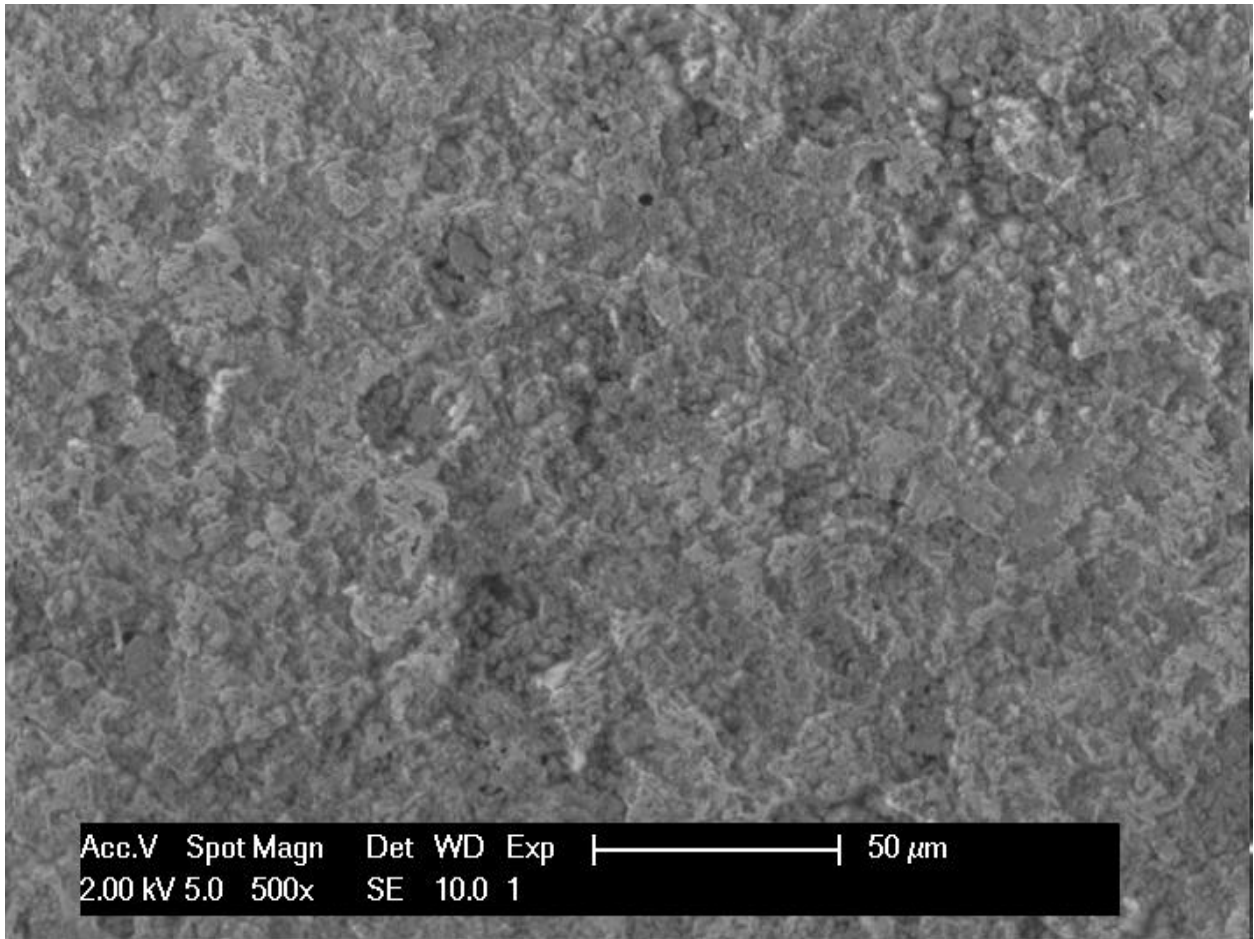


Figure #2.33: SEM image of non-heat treated HT-2902 at 500x magnification

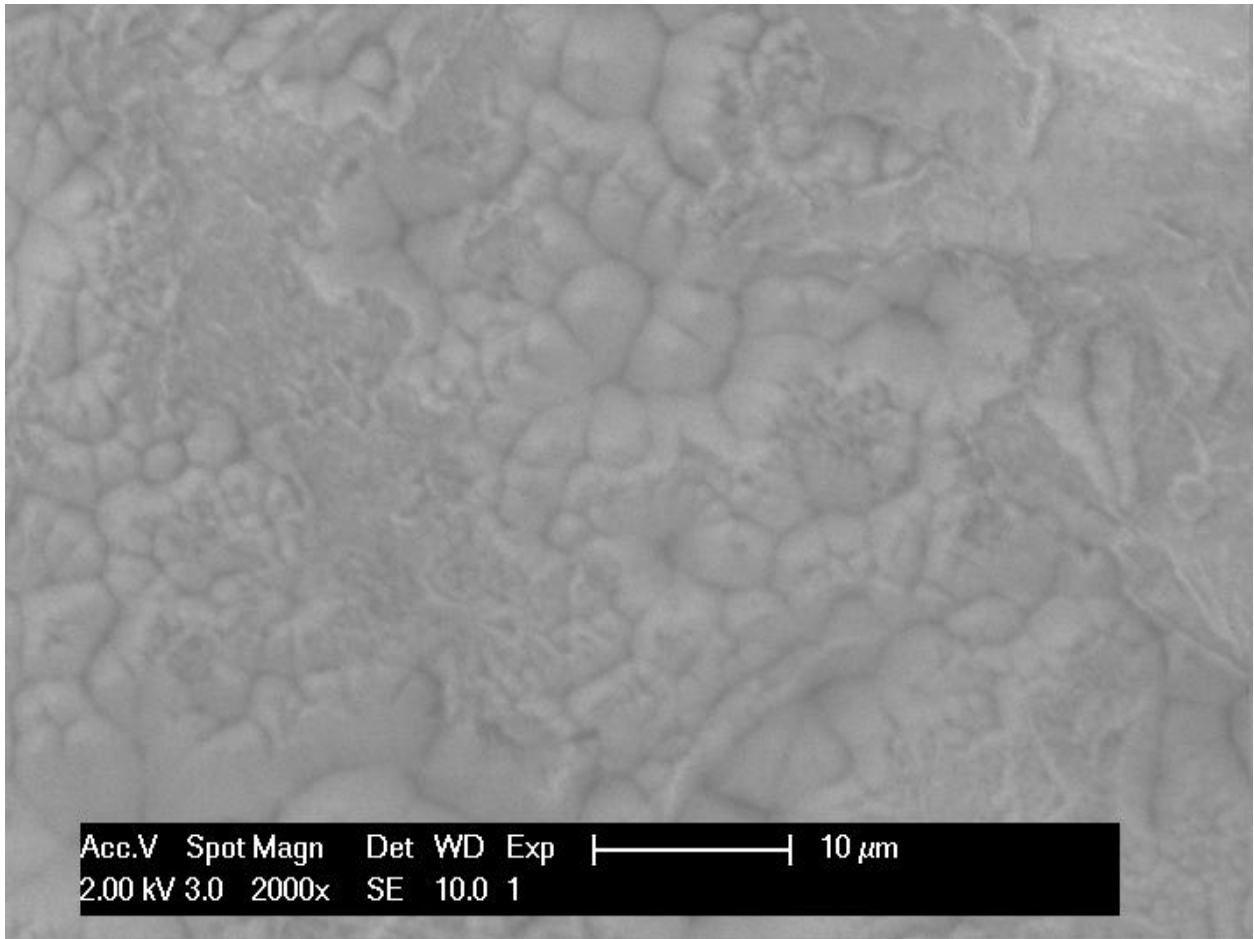


Figure #2.34: SEM image of heat treated HT-2902 at 2000x magnification

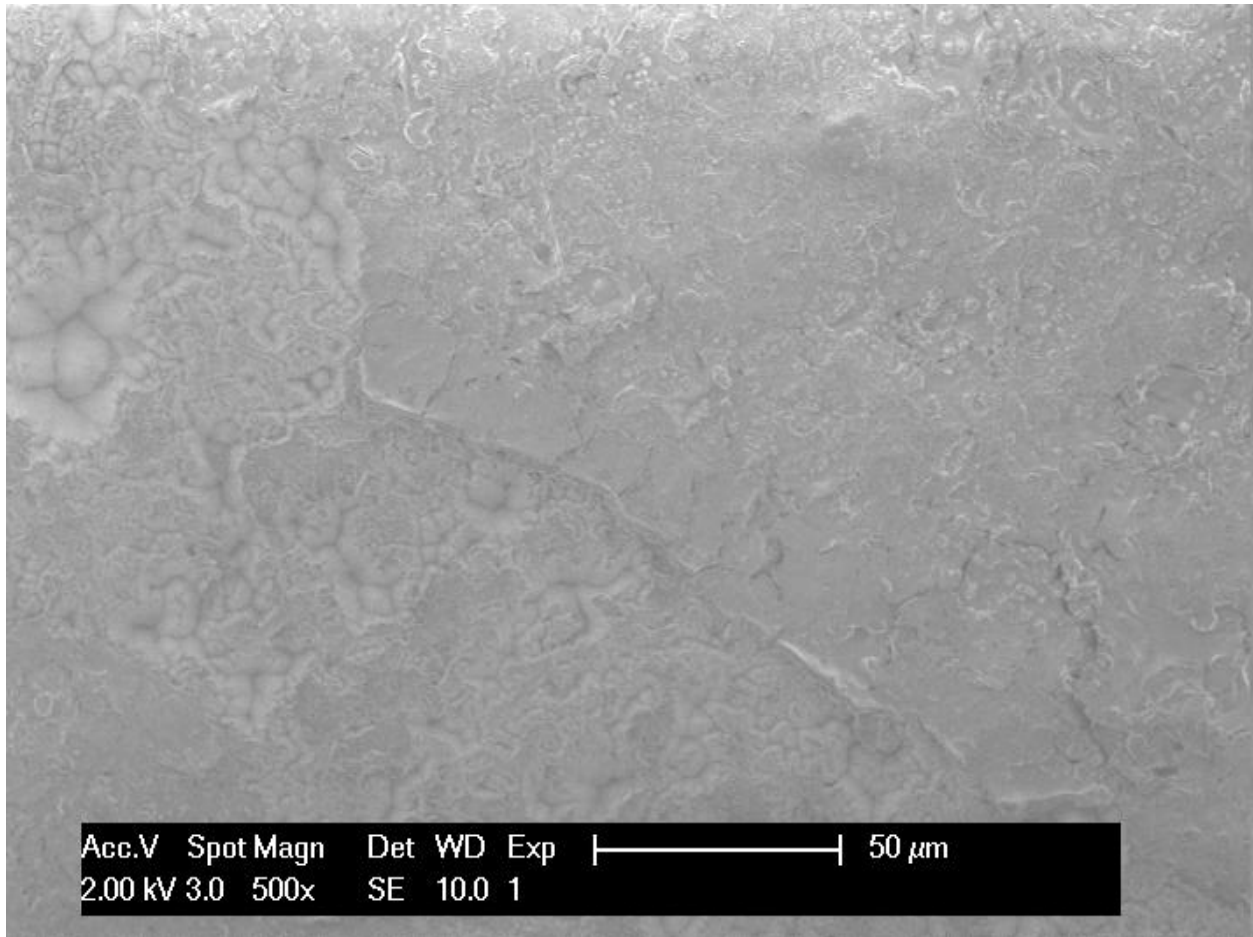
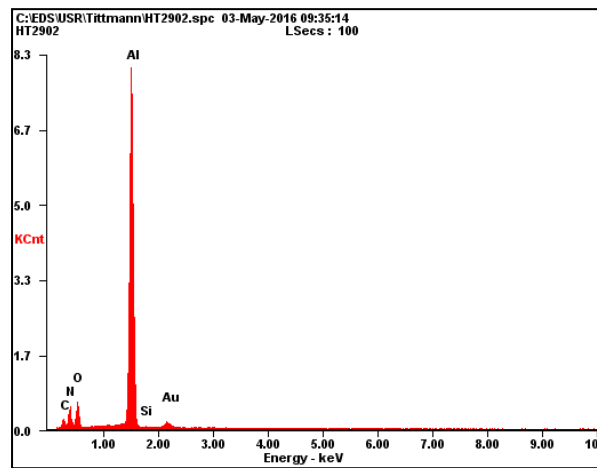
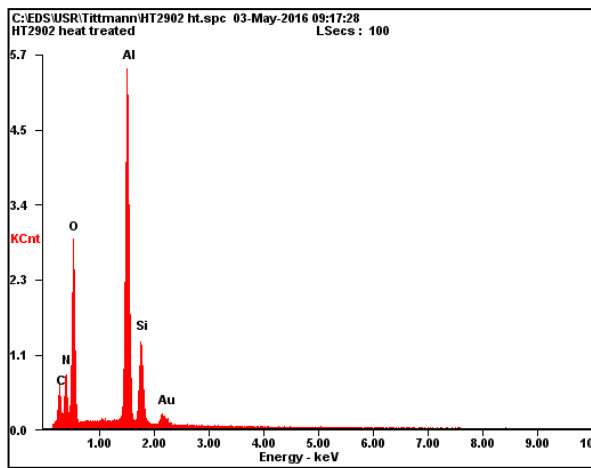


Figure #2.35: SEM image of heat treated HT-2902 at 500x magnification



Figures #2.36 & 2.37: (right) EDS graph of heat treated HT-2902;
 (left) EDS graph of non-heat treated HT-2902

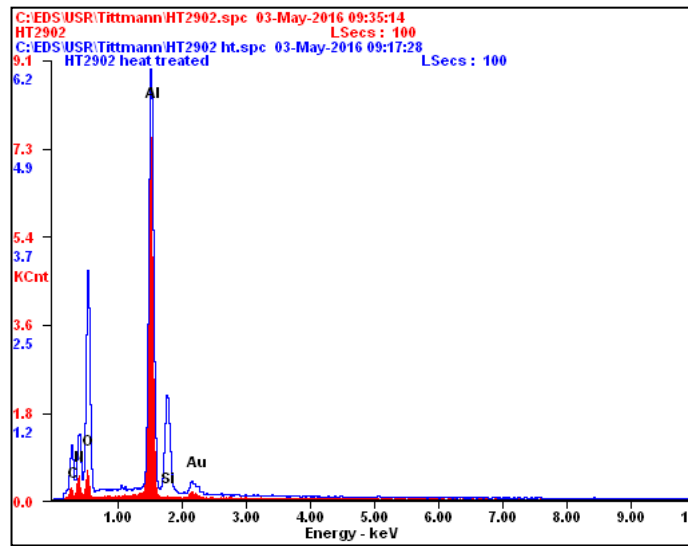


Figure #2.38: Comparison of EDS graphs of HT-2902 (non-heat treated: red; heat treated: blue)

As seen in the EDS plots (Figures #2.36, #2.37, and #2.38), the silicon, oxygen, and gold content on the surface of the HT-2902 piezoelectric element increased after the heat treatment. Potential explanations for these occurrences are as follows: the oxygen content increased because the heat treatment occurred in a non-inert environment with temperatures reaching $>550\text{ }^{\circ}\text{C}$ therefore oxidation reactions may have occurred. The silicon content increased because the Aremco binder that is used as a coupling is silicon-based and a residue may have remained on the surface of the element. Finally, the gold content increased because either the sample was gold-plated when it underwent a previous SEM inspection or the previously introduced gold-aluminum interactions may have occurred, causing a change in the color of the crystal. The gold-aluminum interaction in aluminum nitride hypothesis is unlikely given the dearth of literature on the subject. Nevertheless, the change in color remains a mystery at this point.

From the SEM images of the surface of the crystal (Figures #2.32, #2.33, #2.34, and #2.35), there does seem to be a physical difference between the non-heat treated and heat treated crystal. It almost appears to be a sort of nucleation process that has occurred and made the asymmetries of the crystal surface more defined. These asymmetries could explain the degradation of the performance of the transducer overnight.

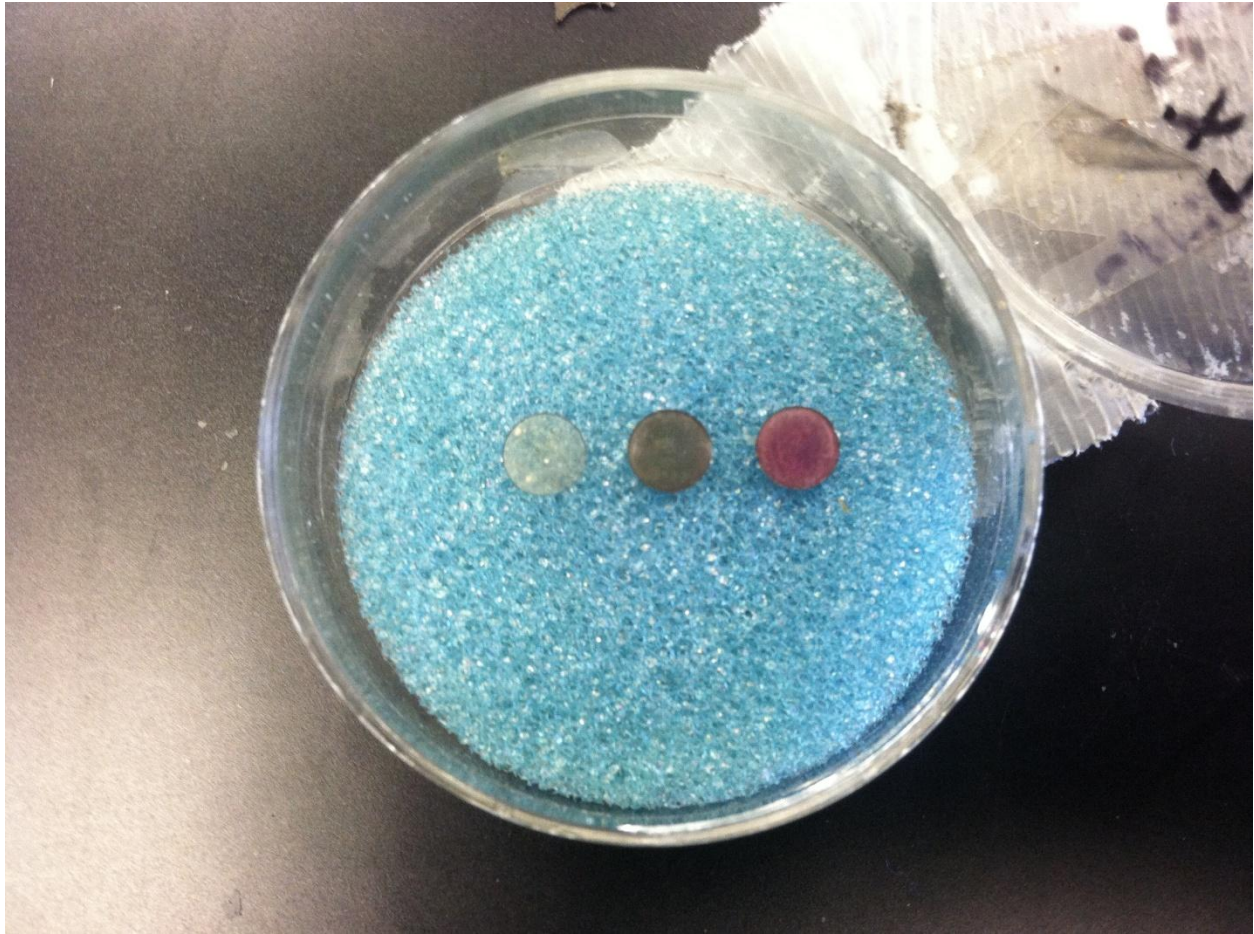


Figure #2.39: HT samples post heat treatment; (from left) HT-2412, HT-2572, HT-2902

An attempt was made to ascertain the reason(s) for the lack of performance of HT-2412 and HT-2572 by verifying that their d_{33} measurements had not been compromised by either the cutting process or the heat treatment. This inquiry produced inconclusive results into discovering why the samples had failed. The d_{33} measurement of HT-2412 came out to be 3.85 pC/N while that of HT-2572 came out to be 3.9 pC/N. A check on the working sample, HT-2902, was also made and the d_{33} measurement came out to be 3.95 pC/N. Each sample showed very little difference in d_{33} value from their pre-cut, pre-heat treated state, therefore ruling it out as a cause of failure.

2.3 Analysis/Conclusions

2.3.1 Bismuth Titanate Analysis

As seen in the plots throughout section 2.1, we can see that the performance of the K15 sodium-modified transducer remained sufficiently steady throughout the period of the test. A vast majority of the test was spent at or above the initial, pre-test acoustic response of the transducer, except for the near-short condition approximately two-thirds of the way through the experiment. Table #2.1 below shows the relative amplitude data (amplitude data relative to the initial signal amplitude data) analysis for the K15 transducer.

K15 Bismuth Titanate	Minimum	Maximum	End	Average
Relative Amplitude	0.15 = 15%	1.17 = 117%	0.95 = 95%	0.95 = 95%

Table #2.1: Relative amplitude signal values for the K15 sodium-modified bismuth titanate transducer during the course of the high temperature endurance test

As can be seen above, the transducer had a net acoustic signal degradation of approximately 5% from the pre-test signal which, when considering the temperature conditions of the test, as shown in Table #2.2, is a rather encouraging result.

K15 Bismuth Titanate	Minimum	Maximum	Average
Temperature	18 °C	546 °C	365 °C

Table #2.2: Minimum, maximum, and average temperature values from the high temperature endurance test on the K15 sodium-modified bismuth titanate transducer

The K15 transducer had a maximum recommended operating temperature of around 450 °C, so seeing that it was capable of functional data collection at a maximum operating temperature of 546 °C gives great confidence in the ability of sodium-modified bismuth titanate to operate as a high temperature capable transducer as required.

A Fast Fourier transform analysis was performed on the final received signal from the K15 transducer and the result can be seen in Figure #2.40 below.

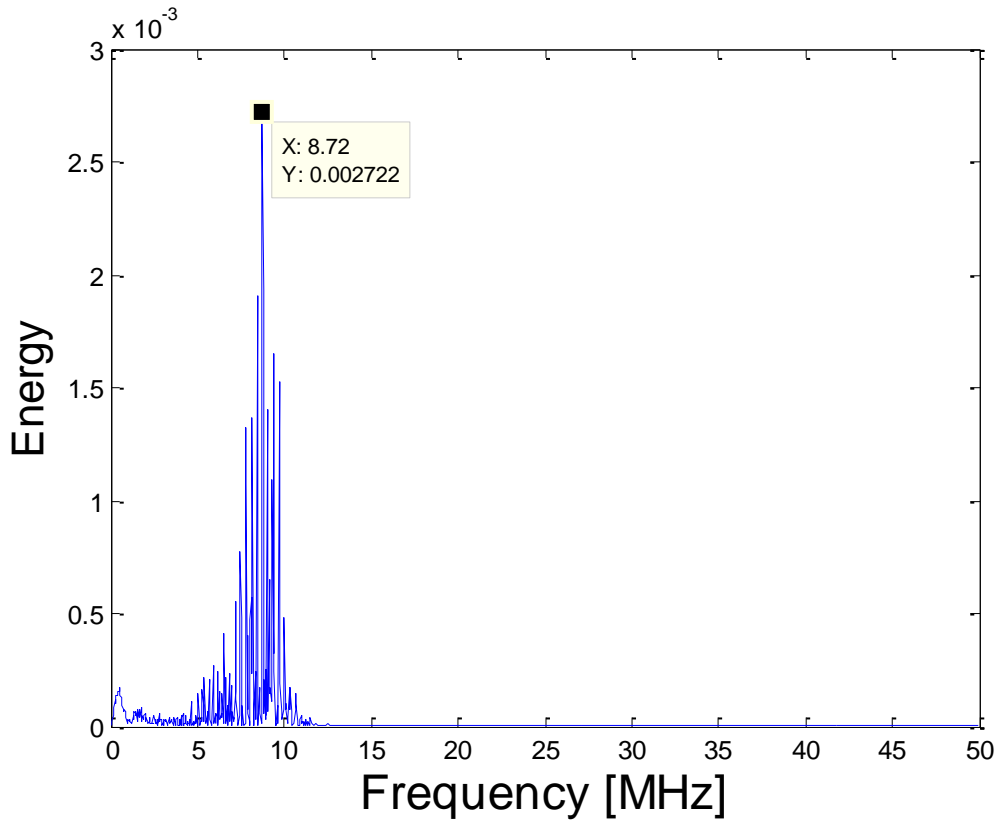


Figure #2.40: Plot of the resonance peak from the FFT analysis of the final signal received from the K15 transducer

In this FFT analysis, there is only one definitive resonance peak from the transducer signal which corresponds more closely to the resonance peak measured at an arrival time of 2.6 μ s from FFT analysis of the initial transducer signal in Figure #2.9. In Table #2.3, a relative resonance frequency shift analysis is performed.

Final Resonance = 8.72 MHz	Relative Frequency (correlated to initial)
Initial Resonance 1 = 9.48 MHz	0.08 = 8%
Initial Resonance 2 = 8.8 MHz	0.009 = 0.9%

Table #2.3: Relative resonant frequency shift from the initial K15 transducer signal to the final transducer signal

It is in the author's opinion that the resonance peak measured at an arrival time of 2.6 μs from the initial FFT analysis is the true resonance while the resonance peak measured at an arrival time of 2.7 μs is an anti-resonance.

2.3.2 Aluminum Nitride Analysis

Unlike the bismuth titanate high temperature endurance test, the aluminum nitride test was not without issues during the course of the experiment. An initial degradation of the aluminum nitride signal came down to a problem with the electronics connected to the device. The signal degradation that occurred near the end of the test was caused by the breakdown of the carbon-carbon backing material in the high temperature, non-inert environment. All in all, however, the test was a tremendous success as can be seen by the relative amplitude results in Table #2.4 below.

Aluminum Nitride	Minimum	Maximum	End	Average
Relative Amplitude	0.03 = 3%	1.38 = 138%	0.89 = 89%	1.11 = 111%

Table #2.4: Relative amplitude signal values for the aluminum nitride transducer during the course of the high temperature endurance test

The signal reached a minimum during the degradation caused by the loss of triggering in the signal. The aluminum nitride transducer performance actually saw a net increase of around 11% over the course of the experiment; a rather encouraging result for even longer term high temperature exposure. In Table #2.5, the temperature conditions that the aluminum nitride transducer underwent are shown.

Aluminum Nitride	Minimum	Maximum	Average
Temperature	18 °C	556 °C	441 °C

Table #2.5: Minimum, maximum, and average temperature values from the high temperature endurance test on the aluminum nitride transducer

The ability to perform in temperature conditions as high as 556 °C and an average temperature of 441 °C over the course of the test is solid verification of aluminum nitride as a

high temperature capable transducer; not only displaying performance in a satisfactory manner, but in a manner where the performance increases as temperature increases and as time goes on.

A Fast Fourier transform analysis of the final signal is performed on the final signal received from the aluminum nitride transducer and the plot can be seen in Figure #2.41 below.

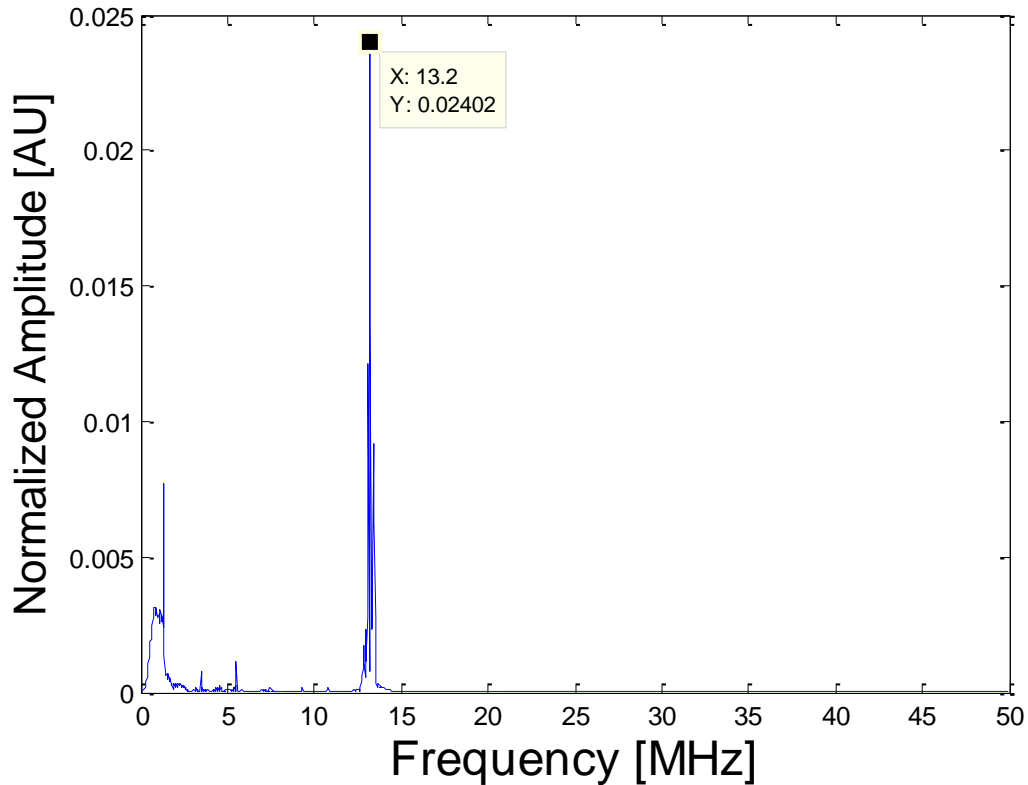


Figure 2.41: Plot of the resonance peak from the FFT analysis of the final signal received from the aluminum nitride transducer

A relative frequency shift analysis is performed and the result is displayed in Table #2.6 below.

Final Resonance = 13.2 MHz	Relative Resonance (correlated to initial)
Initial Resonance = 12.9 MHz	0.02 = 2%

Table #2.6: Relative resonant frequency shift from the initial aluminum nitride transducer signal to the final transducer signal

There is found to be a relative frequency shift of approximately 2% from the initial signal to the final signal. This is likely due to the compression of the piezoelectric element by the thermal expansion of the other material components within the transducer.

3 High Temperature Effects and Irradiation Effects Comparison

Having gathered the data from the high temperature endurance tests, it is time to make the comparison of the high temperature data against data collected from the ULTRA irradiation experiment to gain a better understanding of the effects of temperature on the single crystal transducer system.

3.1 High Temperature Endurance Testing Results

The main results of the high temperature endurance testing on sodium-modified bismuth titanate and aluminum nitride are as follows:
First, the plot of the pulse-echo amplitude versus temperature over time of the sodium-modified bismuth titanate transducer is shown in Figure 3.1.

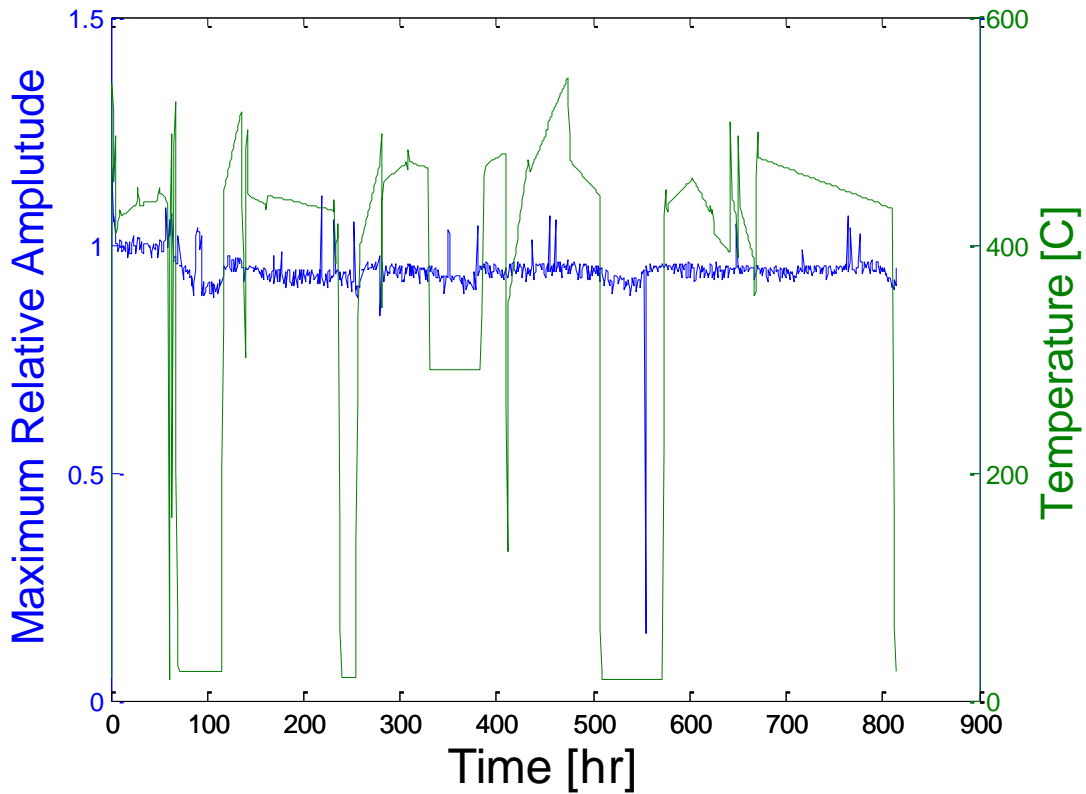


Figure #3.1: Plot of maximum relative amplitude (blue) and temperature [°C] (green) versus time [hr] for the K15 sodium-modified bismuth titanate transducer high temperature endurance test

Next, several important relative amplitude results are included in Table #3.1 below.

K15 Bismuth Titanate	Minimum	Maximum	End	Average
Relative Amplitude	0.15 = 15%	1.17 = 117%	0.95 = 95%	0.95 = 95%

Table #3.1: Relative amplitude signals from the K15 bismuth titanate high temperature endurance test

Then, the plot of the pulse-echo amplitude versus temperature over time of the aluminum nitride transducer is shown.

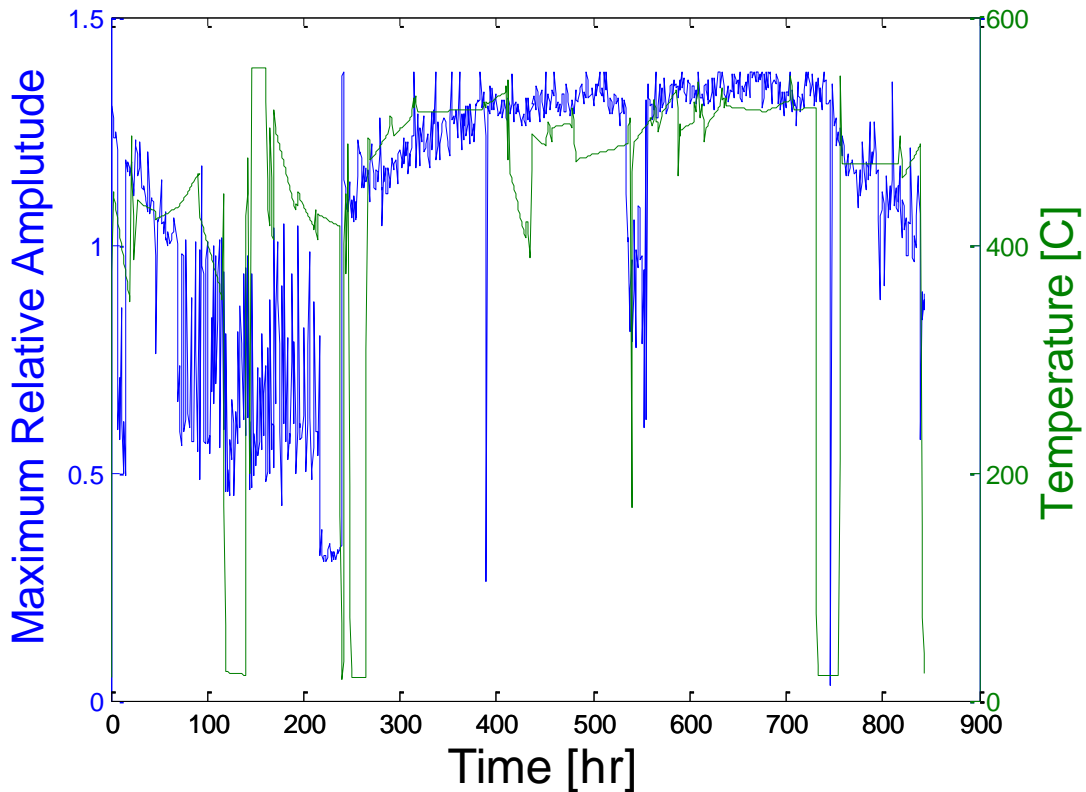


Figure #3.2: Plot of maximum relative amplitude (blue) and temperature [°C] (green) versus time [hr] for the aluminum nitride high temperature endurance test

Finally, several important relative amplitude results are included in Table #3.2 below.

Aluminum Nitride	Minimum	Maximum	End	Average
Relative Amplitude	0.03 = 3%	1.38 = 138%	0.89 = 89%	1.11 = 111%

Table #3.2: Relative amplitude signals from the aluminum nitride high temperature endurance test

3.2 ULTRA Irradiation Results

A little background into the ULTRA irradiation is necessary to better understand the results that follow. After determining the radiation tolerance of aluminum nitride in Penn State’s Breazeale Reactor [23] (Parks & Tittmann 2011), a literature search was performed to find materials of similar properties and structure to aluminum nitride in order to supplement its use in a larger scale irradiation test in the Massachusetts Institute of Technology’s test reactor (MITR).

These additional materials were chosen based on the notion and fact that their piezoelectric properties were superior to that of aluminum nitride and potentially could possess similar radiation tolerant characteristics. These materials were bismuth titanate and zinc oxide. Bismuth titanate has been introduced earlier on and zinc oxide will be looked at in further detail later on.

The main objectives of the MITR irradiation include identifying potential radiation tolerant piezoelectric active elements, designing and building a radiation tolerant ultrasonic sensor capsule, testing the aforementioned piezoelectric active elements in a nuclear reactor that mimics commercial reactor conditions, and demonstrate the viability of making in-situ acoustic measurements within these conditions.

The important results of the irradiation testing include the first ever implemented lead test of bismuth titanate and zinc oxide in a nuclear reactor, the highest neutron and gamma exposure ever for aluminum nitride, bismuth titanate, and zinc oxide, the determination of a limiting radiation dose for bismuth titanate, and validated the operation of aluminum nitride at fast fluence levels above 8×10^{20} n/cm².

The full ULTRA irradiation took place over the course of 458 days, so this will merely be a small sample of the irradiation used for comparison to the high temperature endurance runs. The results and methodology of the ULTRA experiment shall be fully disclosed, hopefully, in two scientific journal articles within the next year or so. Over the course of the first month plus of the ULTRA irradiation, the accumulated fluence can be modeled as a quadratic of the form:

$$\textit{Accumulated Fluence} = 7.1(10^{13})t^2 - 1.7(10^{16})t - 1.9(10^{18}) \quad \textbf{(Eqn. 3.1)}$$

where t is the time of the each fluence data point; fluence data was taken approximately every half hour,

While the accumulated fluence after approximately day 13 can be modeled as a linear function of the form:

$$\textit{Accumulated Fluence} = 1.5(10^{17})t + 2(10^{19}) \quad \textbf{(Eqn. 3.2)}$$

Where t is the same as above

The total accumulated fluence value over the course of the beginning stage of the ULTRA irradiation is 1.49×10^{20} n/cm². The accumulated fluence in addition to the neutron

power of the reactor can be seen plotted against time at the start of the ULTRA irradiation in Figure #3.3.

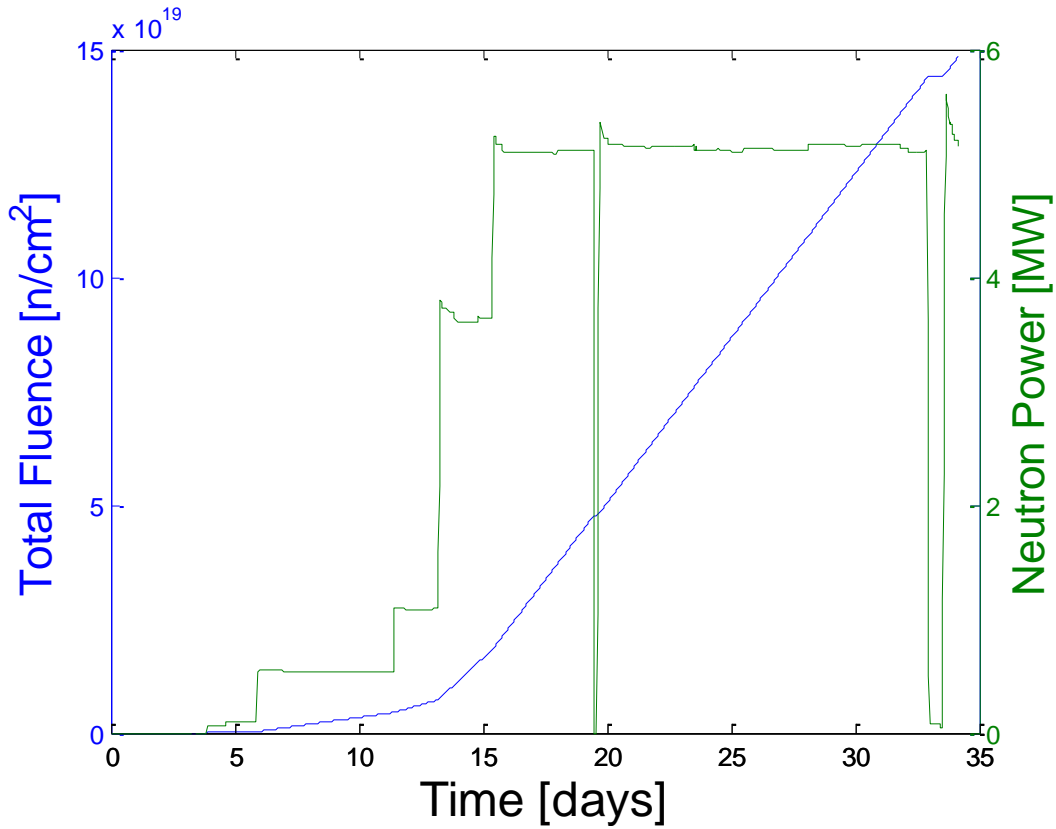


Figure #3.3: Plot of accumulated fluence (blue) and neutron power (green) against time during the beginning stage of the ULTRA irradiation

First, an examination of bismuth titanate as function of fluence will take place. Figure #3.4 displays the plot of the relative amplitude signal from the bismuth titanate transducer against accumulated fluence.

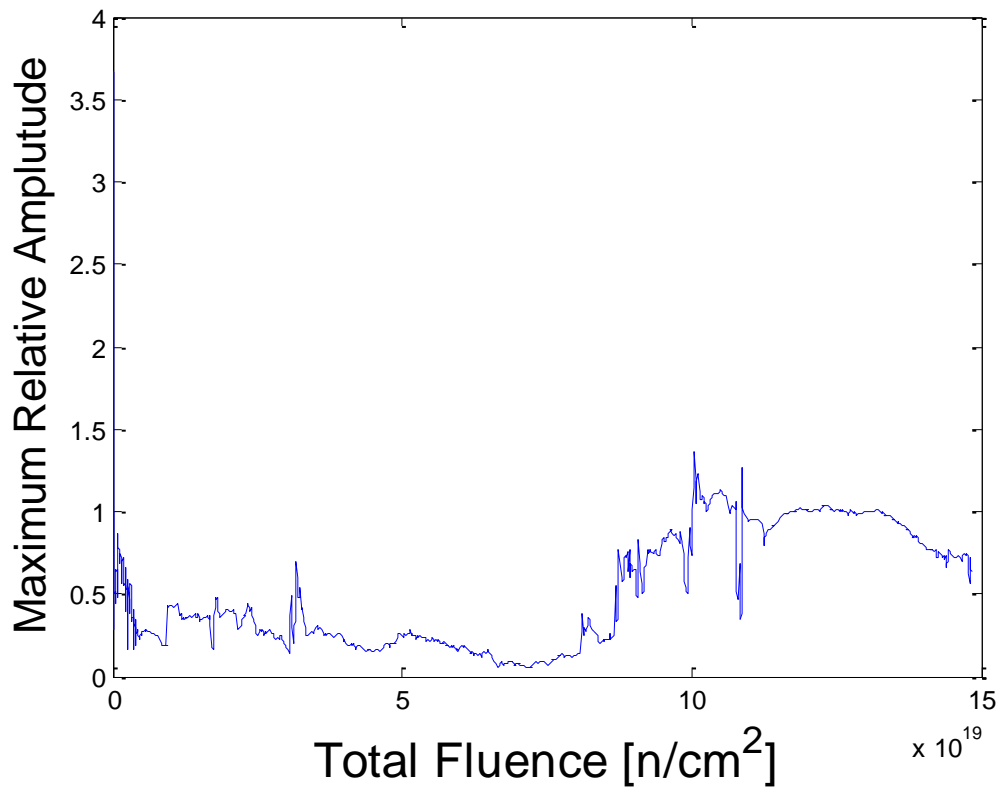


Figure #3.4: Plot of relative amplitude versus total fluence during the beginning of the ULTRA irradiation of the bismuth titanate transducer

Below, Figure #3.5 displays essentially the same plot as Figure #3.4, except the accumulation of fluence over time is highlighted along with performance of the transducer over time.

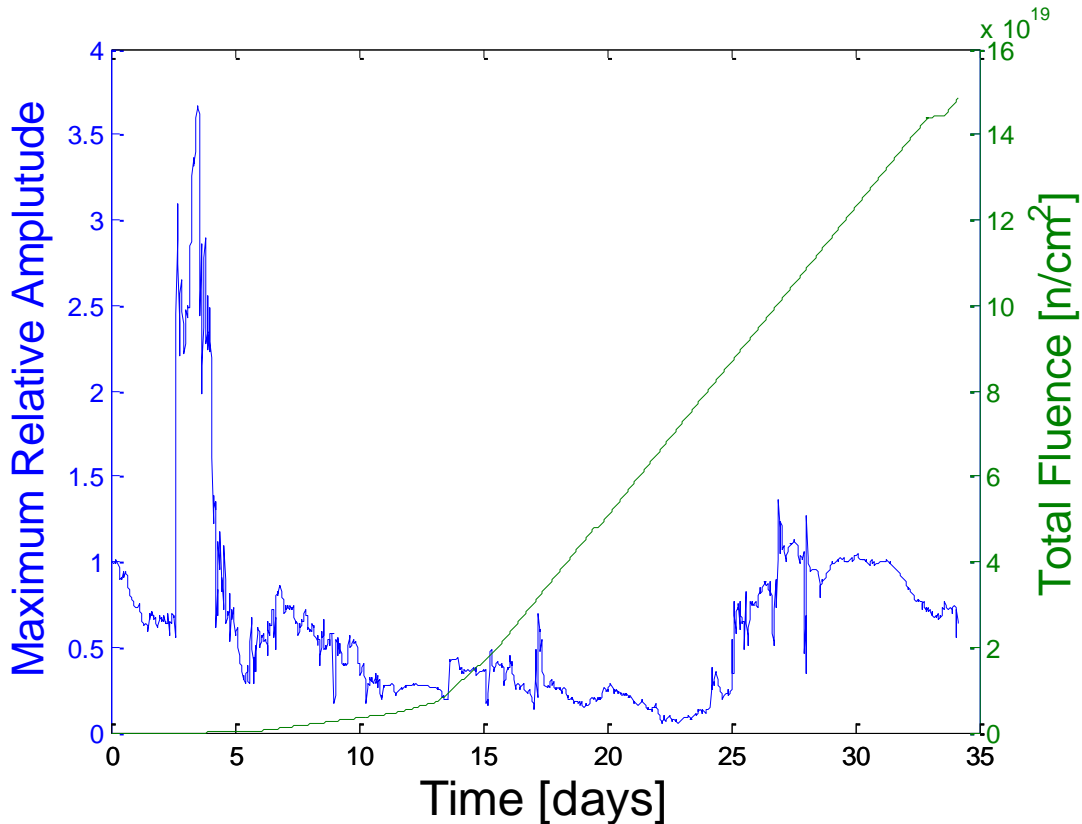


Figure #3.5: Plot of relative amplitude (blue) and total fluence (green) versus time during the beginning of the ULTRA irradiation of the bismuth titanate transducer

Bismuth Titanate	Minimum	Maximum	End	Average
Relative Amplitude	0.06 = 6%	3.67 = 367%	0.63 = 63%	0.62 = 62%

Table #3.3: Relative amplitude signal values for the bismuth titanate transducer during the course of the beginning stage of the ULTRA irradiation

The first thing one might notice is the massive spike in relative amplitude just prior to the irradiation beginning. The reactor itself was in a nearly off state when this spike occurred. There currently is no clear explanation as to why this spike happened; it could be a result of a thermal spike, as recorded on one of the thermocouples, near the beginning, just prior to irradiation. The signal returned to normal by the start of the irradiation and, from there, gradually degraded for the most part. Near the end of the opening stage of the irradiation, an increase in relative amplitude can be observed. The bismuth titanate transducer can be said to work at over 60% efficiency at an accumulated fluence level of approximately $1.5(10^{20}) \text{ n/cm}^2$.

Next, an examination of aluminum nitride as a function of fluence will take place. Below in Figure #3.6, a plot of the relative amplitude signal from the aluminum nitride transducer against the total accumulated fluence in the reactor environment is displayed.

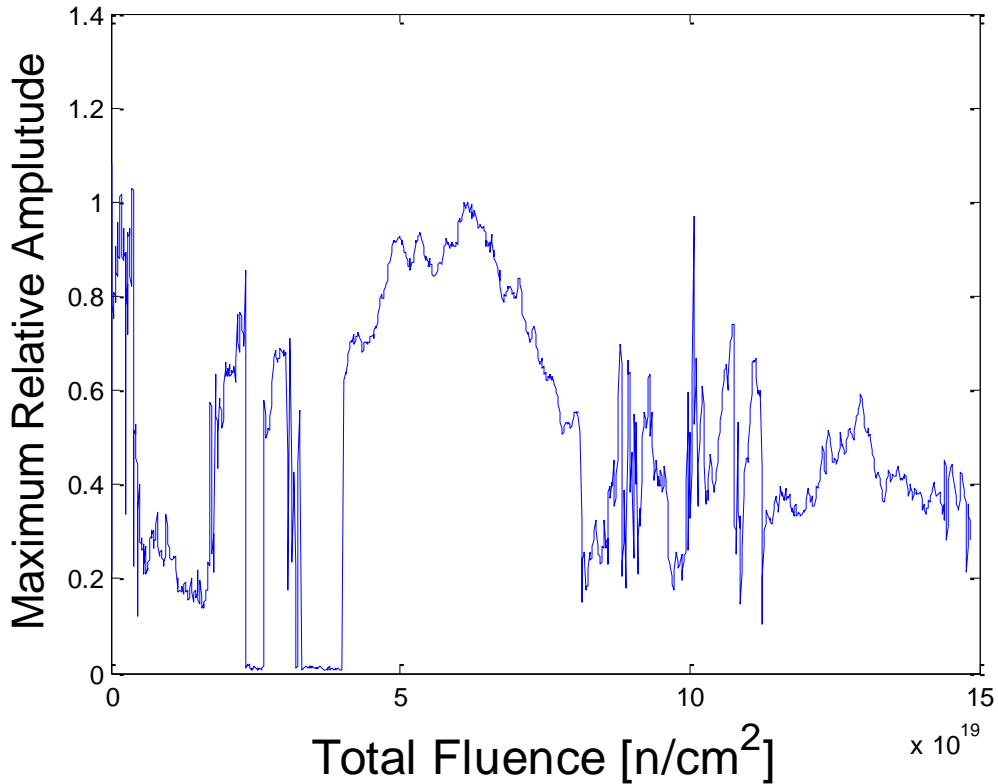


Figure #3.6: Plot of relative amplitude versus total fluence during the beginning of the ULTRA irradiation of the aluminum nitride (ALN-2) transducer

Figure #3.7 below displays the performance of the transducer as well as accumulated fluence over the beginning stages of the ULTRA irradiation.

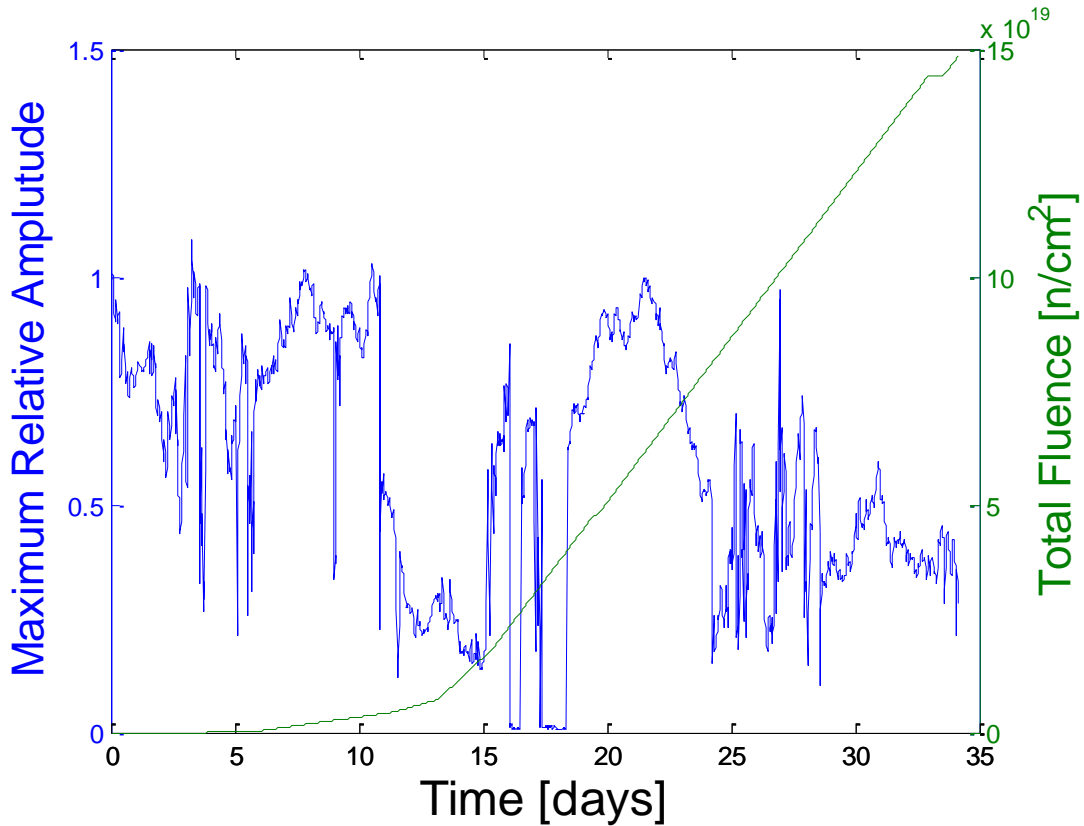


Figure #3.7: Plot of relative amplitude (blue) and total fluence (green) versus time during the beginning of the ULTRA irradiation of the aluminum nitride (ALN-2) transducer

Aluminum Nitride	Minimum	Maximum	End	Average
Relative Amplitude	0.01 = 1%	1.08 = 108%	0.28 = 28%	0.58 = 58%

Table #3.4: Relative amplitude signal values for the aluminum nitride transducer during the course of the beginning stage of the ULTRA irradiation

There can be seen a rather large amount of signal variation in the relative amplitude of the aluminum nitride transducer. There were a couple of sections near the middle of the startup that seemed to show a short in the aluminum nitride signal; however, these potential issues worked themselves out and the signal returned stronger than ever. It can be said that the aluminum nitride transducer works at slightly less than 60% efficiency at an accumulated fluence level of approximately $1.5 \times 10^{20} \text{ n/cm}^2$.

The temperature environment also cannot be overlooked as having an effect on the performance of the transducers. Below in Figure #3.8, the measured temperature from the two

thermocouples alongside the transducers is displayed over the time of the opening stage of the ULTRA irradiation.

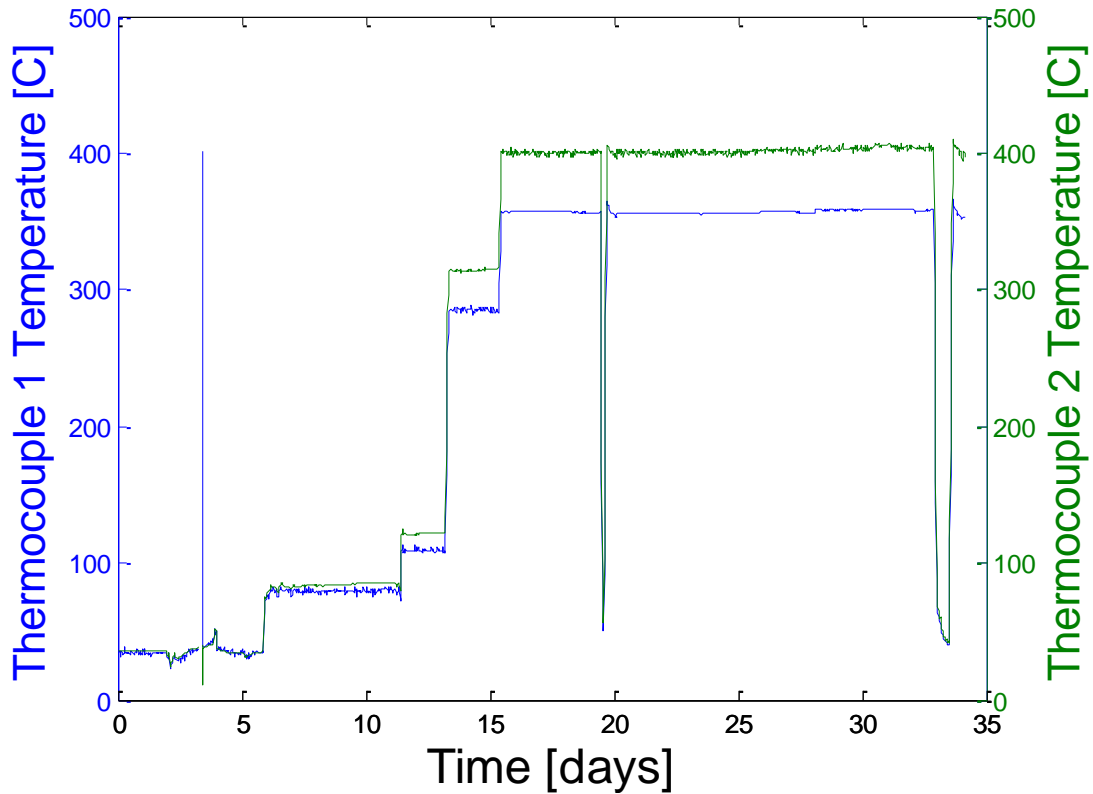


Figure #3.8: Temperature environment of the reactor core, measured on two thermocouples TC1 (blue) and TC2 (green) versus time at the beginning of the ULTRA irradiation

Thermocouple 1 Maximum Temperature [C]	Thermocouple 1 Thermal Spike Temperature [C]	Thermocouple 2 Maximum Temperature [C]
360	401	411

Table #3.5: Maximum temperature recorded by each thermocouple and temperature of the thermal spike recorded by TC1

There can be made a correlation between the temperature environment reaching its highest point and the transducers reaching their relative highest efficiency during irradiation. Both aluminum nitride and bismuth titanate can be seen to show their highest respective relative amplitude values during irradiation after the temperature reaches its peak level.

3.3 Comparison/Conclusions

Sections 3.1 and 3.2 established and displayed the experimental data and analysis from the ULTRA irradiation experiment and the high temperature endurance runs. The research was focused on two particular piezoelectric materials and their performance in these adverse conditions. The main data analysis sets used in comparison are displayed below in Table #3.6.

Material	High Temperature Efficiency	Irradiation Efficiency
Bismuth Titanate	95%	62%
Aluminum Nitride	111%	58%

Table #3.6: Comparison of bismuth titanate and aluminum nitride acoustic transmission efficiencies in high temperature and irradiated conditions

In high temperature conditions, both piezoelectric materials performed well, seeing either only a minimal decrease in acoustic transmission efficiency or a marked increase in efficiency. In irradiated conditions (with some temperature effects), both piezoelectric materials saw their acoustic transmission performance cut by nearly half. It must be noted that the efficiency of bismuth titanate in irradiated conditions is slightly misleading due to the massive jump in performance prior to the start of the first power cycle. It is likely that the bismuth titanate transducer would have fared worse overall than the aluminum nitride transducer under the irradiation, given their relative performances in a high temperature environment as well as the orientation of their crystal structure. The relative efficiency difference for each material is displayed below in Table #3.7.

Material	Relative Efficiency Difference
Bismuth Titanate	35%
Aluminum Nitride	48%

Table #3.7: Relative efficiency differences of selected piezoelectric materials between high temperature and irradiated test conditions

As one might expect, the efficiency of the transducer performance was markedly higher in high temperature conditions as compared to the efficiency of their performance in irradiated

conditions. One might not necessarily expect the dramatic difference in efficiency given the relatively limited time of exposure to each condition. Although it was a limited exposure to flux in the reactor core, the transducer system was still subject to fluence levels on the order of 10^{20} n/cm² which are higher than previously reported levels for both aluminum nitride [23] (Parks & Tittmann, 2011) and bismuth titanate [24] (Kažys, et al., 2007). Therefore, it can be concluded that the performance of aluminum nitride is nearly 50% greater in a high temperature environment compared to that in an irradiated environment while the performance of bismuth titanate is at least 35% greater in a high temperature environment in comparison to that in an irradiated environment.

4 Future Work

There are many exciting possibilities of study that can be further explored based on the results that these experiments have provided. The main works that the author chooses to enumerate are materials optimization of the bulk single crystal transducer system, high temperature endurance testing with zinc oxide single crystal piezoelectric element, and inert environment high temperature endurance testing.

4.1 Materials Optimization

As mentioned in the introduction of this thesis, there would be a preliminary search done in the realm of materials to facilitate an optimization of the current bulk single crystal transducer design. The main property that will be emphasized in this materials search will be the acoustic impedance of the materials in question. Acoustic impedance is vitally important to the transmission and reception of acoustic and ultrasonic waves in the bulk single crystal transducer system.

$$Z = \rho c \quad (\text{Eqn. 4.1})$$

Where Z is the (specific) acoustic impedance of a material, ρ is the density of a material, and c is the speed of sound through a material.

In understanding the relationship of acoustic impedance to the reflection and transmission coefficients, one must come to an understanding of impedance as well as impedance matching. Acoustic impedance is a measure of the resistance or opposition that a material poses to the propagation of an acoustic wave given an acoustic pressure applied to a material system. For example, the acoustic impedance of air is only around 420 Rayl (Pascal*second/meter) whereas the acoustic impedance of water is 1.5 MRayl, making it a far better acoustic transmitter since nearly all condensed phases (liquids and solids) possess high values of acoustic impedance. On that note, impedance matching is the process by which one chooses materials in order to facilitate either acoustic transmission through a boundary between two materials or acoustic reflection at a boundary between two materials.

$$R = \frac{Z_1 - Z_2}{Z_1 + Z_2} \quad \text{(Eqn. 4.2)}$$

Where R is the reflection coefficient of a boundary between two materials, Z_1 is the acoustic impedance of the material from which the acoustic wave propagates, and Z_2 is the acoustic impedance of the material into which the acoustic wave is attempting to propagate.

The transmission coefficient can be derived from the reflection coefficient by the relationship: $T = 1 - R$.

$$T = \frac{2Z_1}{Z_1 + Z_2} \quad \text{(Eqn. 4.3)}$$

Where T is the transmission coefficient of a boundary between two materials and Z_1 and Z_2 are the same as above.

An important introduction that must be made is the acoustic impedances of our chosen piezoelectric materials (AlN, BiT, ZnO) as a reference for this materials optimization operation.

Material	Density (g/cm ³)	Acoustic Wave Speed (m/s)	Acoustic Impedance (MRayl)
Aluminum Nitride	3.26	10127	33.01
Bismuth Titanate	7.2 (K15) - 7.95 (BiT)	4165	29 (K15) – 33 (BiT)
Zinc Oxide	5.676	6350	36.04

Table #4.1: Selected piezoelectric material properties for determination of acoustic impedance

The backing material for the bulk single crystal transducer has been of particular interest. In terms of acoustic impedance, it is important for the backing material to reduce back scattering of the acoustic pulse as much as possible; therefore, a material with an acoustic impedance that is nearly equivalent to that of the acoustic impedance of the piezoelectric material is ideal. The transmission coefficient of the piezoelectric/backing material boundary should be maximized as possible because best efficiency is achieved when energy is transmitted rather than reflected.

For many years, the ENCC lab has employed carbon-carbon composite in this capacity due to its porosity, retention of mechanical properties at high temperatures, and low electrical and thermal conductivities. Prior to carbon-carbon composite, high purity aluminum foil, compressed into a cylinder, was used as a backing material. However, in non-inert conditions, the use of carbon-carbon becomes problematic. Therefore, it is necessary to explore the possibility of replacing carbon-carbon composite as the preferred backing material for the bulk single crystal transducer system. In the work of Amini, Sinclair, and Coyle [25], they introduced the idea of porous ceramics as a backing material. One material in particular was preferred: zirconium oxide or zirconia as it is typically referred to. Zirconia is one of the most studied ceramics and is most commonly seen in its cubic phase as a diamond stimulant, due to the fact that it shares a nearly identical visual appearance. However, at high temperatures, zirconia goes through problematic phase changes where the volumetric expansions between phases induce large stresses on the crystal structure which leads to cracking upon cooling. Therefore, pure zirconia would be unsuitable as a high temperature backing material. However, when doped with certain other oxide materials, these destructive phase changes stabilize. The dopant of choice was yttrium oxide or yttria due to the fact that yttria eliminates the destructive phase changes completely. This yttria-stabilized zirconia is commercially available, but does not come in a porous ceramic form. Therefore, an additive of polyethylene polymer microspheres is necessary in addition to pressing and sintering the compound. The sintering process burns out the polymer

spheres, leaving the compound in the desired porous ceramic form. This is a ceramic compound that will see viability studies in the future.

The idea is to compare these three materials: carbon-carbon composite, aluminum foil, and the yttria-stabilized zirconia ceramic compound in terms of their acoustic impedances to determine which might be the most effective material for reducing back scatter in the bulk single crystal transducer system.

Material	Density (g/cm ³)	Acoustic Wave Speed (m/s)	Acoustic Impedance (MRayl)
Aluminum 1100 (foil)	2.7	6420	17.33
Carbon-carbon composite	1.3-1.8	4815	6.26-7.31
Yttria-stabilized Zirconia	6.05	3802	23

Table #4.2: Selected backing material properties for determination of acoustic impedance

Upon initial viewing of table #4.2, one would be led to believe that the yttria-stabilized zirconia compound is the immediate and clear choice as best possible backing material from those selected as it provides the closest possible impedance match to the selected piezoelectric materials. The calculations of the transmission coefficient will back up this initial hypothesis.

Material	Acoustic Impedance (MRayl)	Transmission Coefficient
Aluminum 1100 (foil)	17.33	0.69 (AlN); 0.75 (K15) – 0.69 (BiT); 0.65 (ZnO)
Carbon-Carbon Composite	6.26-7.31	0.32-0.36 (AlN); 0.36-0.40 (K15) – 0.32-0.36 (BiT); 0.30-0.34 (ZnO)
Yttria-stabilized Zirconia	23	0.82 (AlN); 0.89 (K15) – 0.82 (BiT); 0.78 (ZnO)

Table #4.3: Transmission coefficients for selected backing materials

After making the calculations of the transmission coefficients of the selected backing materials, it is clear to see that the yttria-stabilized zirconia does provide the best impedance match between itself and each piezoelectric element. However, there are other factors that must go into consideration when crafting the ideal bulk single crystal transducer system. Although the math does not make for good reading about the carbon-carbon composite, it has numerous other advantages that still lend itself to a proper backing material. When the energy from an acoustic

wave is transmitted into a backing material, reflections from the backing material will appear in an amplitude scan unless the sound is attenuated by the material. Carbon-carbon is a natural attenuator of sound due to its defined porosity in the structure. When one goes through the process of pressing and sintering the yttria-stabilized zirconia with polymer microspheres additives to the mixture, you will supposedly attain the porous matrix necessary for sound attenuation and, in theory, possess a more efficient backing material than carbon-carbon for high temperature applications.

There are a number of other factors that need to be addressed when selecting the best backing material for high temperature applications, but as mentioned before, this is a preliminary materials optimization search. One of these other factors is the fact that the backing material needs to be coupled well to the piezoelectric element for the highest possible quality factor.

Next, a preliminary evaluation of waveguide materials for acoustic transmission shall take place. The four selected waveguide materials chosen for this evaluation are: aluminum 6061, kovar, 304 stainless steel, and 316 stainless steel. Much like the backing material, a high transmission coefficient of the piezoelectric element/waveguide boundary is an important factor in determining the best candidate material.

Material	Density (g/cm ³)	Acoustic Wave Speed (m/s)	Acoustic Impedance (MRayl)
Aluminum 6061	2.7	6420	17.33
Kovar	8.36	4200	35.11
304 Stainless Steel	8.03	4990	40.07
316 Stainless Steel	7.99	4915	39.27

Table #4.4: Selected waveguide material properties for determination of acoustic impedance

An initial look at Table #4.4 shows that kovar is the closest match to each of the candidate piezoelectric materials. The calculations of the transmission coefficients will provide confirmation of the initial hypothesis.

Material	Acoustic Impedance (MRayl)	Transmission Coefficient
Aluminum 6061	17.33	0.69 (AlN); 0.75 (K15) – 0.69 (BiT); 0.65 (ZnO)
Kovar	35.11	0.97 (AlN); 0.91 (K15) – 0.97 (BiT); 0.99 (ZnO)
304 Stainless Steel	40.07	0.90 (AlN); 0.84 (K15) – 0.90 (BiT); 0.95 (ZnO)
316 Stainless Steel	39.27	0.91 (AlN); 0.85 (K15) – 0.91 (BiT); 0.96 (ZnO)

Table #4.5: Transmission coefficients for selected waveguide materials

Although the selected materials do provide an excellent impedance match to the chosen piezoelectric elements, the impedance match would amount to very little without proper coupling.

There are a number of coupling methods that can be employed to connect the piezoelectric element and the waveguide. The three main coupling techniques are: dry coupling, liquid coupling, and solid coupling as introduced by [7] (Kažys, et al., 2008). Dry coupling is based on high pressure keeping the air gap between piezoelectric and waveguide as small as possible on the order of $<0.01 \mu\text{m}$. However, since it is a technique based on acoustic transmission through air, the acoustic energy entering the waveguide is substantially reduced. A highly polished and flat surface provides the best possible conditions for dry coupling. Typically, a metal foil is employed to facilitate the dry coupling method. $\lambda/2$ and λ matching layers of metal foil have not been shown to be successful due to bending of the foil under pressure. Therefore, a $\lambda/4$ matching layer is ideal for the dry coupling method. Liquid coupling is rather impractical for use with metals due to corrosive issues, with piezoelectric materials due to flow caused by vibrations of the piezoelectric element, and in high temperature conditions due to evaporation. Solid coupling has several viable techniques that have seen use in high temperature environments: soldering, diffusion bonding, ultrasonic welding, cement, and epoxy bonding. A silver-based solder with a melting point around $500 \text{ }^\circ\text{C}$ has been used with lithium niobate piezoelectric sensors. Gold-to-gold diffusion bonding has been used in bismuth titanate sensors in high temperature applications while sensors with lithium niobate piezoelectric elements have used copper diffusion bonding to operate at temperatures up to $350 \text{ }^\circ\text{C}$. Epoxy bonding, using an Aremco inorganic silver-based epoxy, is being used in the development of aluminum nitride and gallium phosphate piezoelectric wafer transducers which possess both high temperature and harsh environment capabilities. Since there is not any single solid coupling technique that works

universally for high temperature applications, sol-gel and chemical vapor deposition (CVD) methodologies have been employed to tailor the ceramic for specific applications.

The ENCC Lab has used dry coupling, employing either aluminum or gold foil, and solid coupling, employing an inorganic epoxy, in the development and construction of high temperature, harsh environment ultrasonic transducers. In addition, the ENCC lab also previously used a sol-gel process for fabrication of bismuth titanate spray-on transducers, but moved away from this process in recent years in order to reduce chemical waste.

As stated prior, this is a first step at materials optimization of the bulk single crystal transducer design. There are more factors than simply optimizing the impedance match between materials, but it is an important step to take towards improving the efficiency of acoustic transmission between elements within the transducer.

4.2 Zinc Oxide Testing

As of this writing, we had only just obtained the promised single crystal zinc oxide for high temperature endurance testing. ZnO had shown promise in previous high temperature tests, but failed to meet expectations when introduced into an irradiated environment. The main reason we felt that the ZnO transducer had failed is that the crystal itself lacked the necessary purity to facilitate proper transmission in the test conditions. The hope is to obtain high purity crystals for best performance in long term high temperature and harsh environment endurance testing. Typically, when ZnO is exposed to high temperature conditions, it will change color from clear to yellow and return to clear when cooled to room temperature. However, in previous high temperature work done in the ENCC lab, this was not the case. Much the same situation occurred in the reactor test, the hypothesis being that the color change was caused by the presence of zinc interstitials within the crystal lattice as seen in the work of Gomi, et al [26]. Therefore, it has been determined that ZnO deserves another chance to establish itself as a viable high temperature and harsh environment piezoelectric element.

Zinc oxide possesses the wurtzite crystal structure much like aluminum nitride. Zinc oxide is a quite common material even found in household cleaners. Zinc oxide is a viable material for high temperature applications because it does not undergo any phase transformations all the way up to its melting temperature of 1975 °C. Since zinc oxide is typically formed

through oxidation processes, it does not readily oxidize in its single crystal form. The main reaction that occurs in zinc oxide in an oxygen environment is a thermochromic reaction at approximately 800 °C, where the clear zinc oxide crystal turns yellow due to a loss of oxygen and reverts to clear upon cooling. Zinc oxide sees a decrease of around 30% in its dipole density/polarization in the 3-direction (e_{33}) and an increase of around 30% in the 1-direction (e_{31}) due to changes in its spontaneous polarization over a temperature range of 0-400 °C, in part due to the shape of its wurtzite structure [27] (Hill and Waghmare, 2000). It has the strongest piezoelectric electromechanical coupling coefficient among the tetrahedrally bonded semiconductors such as gallium nitride and aluminum nitride [28] (Dal Corso, et al, 1994). It is also thought to possess a strong resistance to amorphization due to strong ionic bonding between atoms [29] (Trachenko, 2004).

Material	Elastic Modulus (GPa)	Density (g/cm ³)	Thermal Expansion (m/m/°C)	Piezoelectric Sensitivity (d_{33}) (pC/N)	Coupling Coefficient (k_{33})	Curie Temperature (°C)	Melting Temperature (°C)	Oxidation Temperature (°C)
ZnO	229	5.676	2.9-4.75(10^{-6})	10.6	0.41	n/a	1975	800 (Thermochromic reaction)

Table #4.6: Mechanical, thermal, and acoustic properties of zinc oxide

While single crystals of ZnO are piezoelectric, polycrystalline (ceramic) ZnO with randomly oriented grains do not exhibit the piezoelectric effect. Since it is not ferroelectric, polycrystalline ZnO cannot be poled like barium titanate or lead zirconate titanate (PZT). Ceramics and polycrystalline thin films of ZnO may exhibit macroscopic piezoelectricity only if the ceramic or thin film is textured i.e. the grains are preferentially oriented, such that the piezoelectric responses of all individual grains do not cancel. This is a process readily accomplished in polycrystalline thin films.

In nuclear reactor applications, there might be risk of transmutations occurring in zinc oxide. Callister and Rethwisch [30] state that zinc can transmute into several different atoms depending on the amount of neutrons present within the nucleus (zinc-64 transmutes into copper-65, zinc-68 transmutes into gallium-69, and zinc-70 transmutes into gallium-71). They also state that the oxygen within the crystal lattice can also transmute (oxygen-18 transmutes into fluorine-19).

4.3 More Inert Environment Testing

Due to constraints in terms of time and resource availability (furnace, inert gas, gas hookup, etc), the experiments as enumerated above were performed under non-inert (oxygen atmosphere) environment conditions. This meant that the components of the transducer were more likely to undergo the process of oxidation which adversely affects their ability to transmit and receive acoustic waves. In particular, the backing material, made of carbon-carbon composite, was most adversely affected by the non-inert conditions, with the carbon burning out of the matrix and leaving behind the carbon fibers. However, it was an excellent verification of the performance of the transducers at high temperature in a non-inert environment. In comparison to an inert environment, the conditions are harsher on the material components in a non-inert environment, therefore, making it a valuable test nonetheless.

In the future, it will be vital for best correlation between results to perform the high temperature endurance tests in inert conditions to better simulate the environment of a nuclear reactor sans radiation. This plan for future work is written, a furnace with the capability to facilitate an inert environment has become available. It is likely that the inert environment, high temperature endurance test results shall be seen in the near future assuming that all preparations continue smoothly.

5 Conclusion

The main thrust of this thesis was to investigate the effect of temperature on the performance of ultrasonic piezoelectric transducers by comparing the results of high temperature endurance testing to results provided by the ULTRA project where ultrasonic transducers, with the same piezoelectric element as in the high temperature tests, underwent long term exposure to the environment within a nuclear reactor core. Another, more minor point was a preliminary push towards the optimization of the bulk single crystal transducer system in order to facilitate the best acoustic transmission and reception capabilities and to establish a means of tailoring the system for a given application, whether it is high temperature or harsh environment.

The results of the high temperature endurance testing performed on piezoelectric materials aluminum nitride and bismuth titanate showed that their performance at elevated

temperatures was comparable (and even better in the case of aluminum nitride) to their performance at room temperature. Aluminum nitride displayed an 11% increase in performance over the course of 35 days in temperatures reaching over 550 °C (556 °C) and within an average temperature environment of approximately 441 °C. Aluminum nitride also saw a slight shift in resonant frequency, 2% from 12.9 MHz to 13.2 MHz due to the compression of the piezoelectric element as it was acted upon by the thermal expansion of the other elements that made up the transducer construction. Three more crystals of aluminum nitride underwent high temperature viability studies. HT-2902 is the most promising of the three as HT-2412 and HT-2572 failed to reach the desired temperature level before failure. HT-2902 underwent an as yet unexplained crystal color change from brown to pink-purple when exposed to a high temperature environment of 550 °C. Bismuth titanate displayed a 5% decrease in performance over 34 days in temperature reaching nearly 550 °C (546 °C) and within an average temperature environment of approximately 365 °C.

The ULTRA irradiation results of the performance of aluminum nitride and bismuth titanate in the reactor core made for an interesting comparison. The ultrasonic transducers, over the first 34 days of the irradiation, were exposed to $1.5(10^{20})$ n/cm² of total fluence within the reactor core. Aluminum nitride saw a decrease of over 40% (42%) in its performance in these high fluence levels. Bismuth titanate displayed an average performance that was 38% lower than its performance at the time of insertion. This number is slightly misleading as there was a massive and unexplained increase in signal amplitude received from the bismuth titanate transducer in the beginning stages of the first neutron and thermal power cycle. It should be stated that the performance of both transducers improved when the temperature of the reactor core was recorded as rising near 400 °C. When the comparison is made between the results from the high temperature endurance testing and the ULTRA irradiation, it is quite clear which conditions have the largest effect on the performance of the single crystal piezoelectric transducers. The performance of aluminum nitride was 48% higher in high temperature conditions than in an irradiated environment while the performance of bismuth titanate was 35% higher. These results are not wholly unexpected as there are more known failure mechanisms, as well as a higher chance of failure, within an irradiated environment.

The beginning stages of a materials optimization process were undertaken. The primary property focused on within the optimization process was the acoustic impedance of the candidate

materials. The acoustic impedance of the waveguide and backing materials should match that of the piezoelectric element as closely as possible for best acoustic transmission. The candidate backing materials were aluminum foil, carbon-carbon composite (the incumbent), and a new porous ceramic, yttria-stabilized zirconia. When a calculation of transmission based on the acoustic impedance match between backing and piezoelectric materials was performed, it was found that the yttria-stabilized zirconia porous ceramic would provide the best acoustic transmission for each of the candidate piezoelectric materials. There are several other factors that go into the selection of a proper backing material such as the ability to attenuate sound effectively and proper coupling to the piezoelectric element for a high quality factor, but this is a step in the right direction particularly if more applications require non-inert environment high temperature conditions. The candidate waveguide materials were aluminum 6061, kovar (the incumbent), 304 stainless steel, and 316 stainless steel. The same calculation of transmission coefficient as performed for the backing materials was done for the candidate waveguide materials. It was found that kovar matched impressively and the most closely to each of the piezoelectric materials. As with the selection of the right backing material, the selection of the waveguide also depends on several other factors besides impedance matching and high transmission coefficients such as the right matching layer, typically $\lambda/4$, to facilitate the transmission of the acoustic energy from piezoelectric crystal into the waveguide and proper coupling between the waveguide and piezoelectric material.

These are the final conclusions drawn from the writing of this thesis. It has been a journey, long and arduous, but rewarding in many ways.

References

- [1] D. A. Parks, Tittmann, B. T., and Kropf M. M., “Aluminum Nitride as a High Temperature Transducer”, *AIP Conference Proceedings*, Vol. 1211, pp. 1029-1034, 2010.
- [2] V. Giurgiutiu, *Structural Health Monitoring*, Academic Press (Elsevier), Burlington, MA, 2008.
- [3] “Piezoelectric Principle.” *Metra Mess- Und Frequenztechnik in Radebeul* E.K. Manfred Weber, n.d. (http://www.new.mmf.de/piezoelectric_principle.htm)
- [4] “Piezoelectric Effect.” *PC Control Learning Zone*. Pc-control.co.uk, n.d. (http://www.pc-control.co.uk/piezoelectric_effect.htm)
- [5] “About NDT.” *NDT Resource Center*. NDE Education, n.d. (<https://www.nde-ed.org/AboutNDT/aboutndt.htm>)
- [6] F. K. Chang, Prosser, W. H., and Schulz, M. J., *Structural Health Monitoring*, Vol. 1, pp. 3-4, 2002.
- [7] R. Kažys, Voleišis, A., and Voleišienė, B., “High temperature ultrasonic transducers: review”, *Ultragarsas Journal*, Vol. 63, No. 2, pp. 7-17, 2008.
- [8] J. H. Lee, Lee, M. R., Kim, J. T., Luk, V., and Jung Y. H., “A study of the characteristics of the acoustic emission signals for condition monitoring of check valves in nuclear power plants”, *Nuclear Engineering and Design*, Vol. 236, No. 13, pp. 1411-1421, 2006.
- [9] J. F. Villard and Schyns, M., “Innovations for in-pile measurements in the framework of the CEA-SCK-CEN Joint Instrumentation Laboratory”, *Advancements in Nuclear Instrumentation Measurement Methods and their Applications (ANIMMA) Proceedings*, pp. 1-8, 2009.
- [10] K. K. Phani, Sanyal, D., and Sengupta, A. K., “Estimation of elastic properties of nuclear fuel material using longitudinal ultrasonic velocity – A new approach”, *Journal of Nuclear Materials*, Vol. 366, No. 1-2, pp. 129-136, 2007.
- [11] J. L. Rempe, Knudson, D. L., Daw, J. E., Condie, K. G., and Curtis Wilkins, S., “New Sensors for In-Pile Temperature Measurement at the Advanced Test Reactor National Scientific User Facility”, *Nuclear Technology*, Vol.175, No. 3, pp. 681-691, 2011.
- [12] A. O. Niedermayer, Voglhuber-Brunnmaier, T., Sell, J., and Jakoby, B., “Methods for the robust measurement of the resonant frequency and quality factor of significantly damped resonating devices”, *Measurement Science and Technology*, Vol. 23, No. 8, pp. 1-11, 2012.
- [13] T. Yano, Inokochi, K., Shikama, M., Ukai, J., Onose, S., and Maruyama, T., “Neutron irradiation effects on isotope tailored aluminum nitride ceramics by a fast reactor up to 2×10^{26} ”, *Journal of Nuclear Materials*, Vol. 329-333, Part B, pp. 1471-1475, 2004.

- [14]Y. Ito, Yasuda, K., Ishigami, R., Sasase, M., Hatori, S., Ohashi, K., Tanaka, S., and Yamamoto, A., “Radiation Damage of Materials Due to High Energy Ion Irradiation”, *Nuclear Instruments and Methods in Physics Research*, Vol. 191, No. 1-4, pp. 530-535, 2002.
- [15]H. S. Shulman, Testorf, M., Damjanovic, D., and Setter, N., “Microstructure, Electrical Conductivity, and Piezoelectric Properties of Bismuth Titanate”, *Journal of the American Ceramic Society*, Vol. 79, No.12, pp. 3124-3128, 1996.
- [16]E. Aksel and Jones, J. L., “Advances in Lead-Free Piezoelectric Materials for Sensors and Actuators”, *Sensors*, Vol. 10, pp. 1935-1954, 2010.
- [17]T. Takenaka, and Nagata, H., “Sodium Bismuth Titanate-Based Ceramics”, *Lead Free Piezoelectrics*, pp. 255-290, 2012.
- [18]L. M. Manocha, “High performance carbon-carbon composites”, *Sadhana*, Vol. 28, No. 1 & 2, pp. 349-358, 2003.
- [19]R. Luo, Liu, T., Li, J., Zhang, H., Chen, Z., and Tian, G., “Thermophysical properties of carbon/carbon composites and physical mechanism of thermal expansion and thermal conductivity”, *Carbon*, Vol. 42, No. 14, pp. 2887-2895, 2004.
- [20]J. Chłopek, Błażewicz, S., and Powroźnik, A., “Mechanical properties of carbon-carbon composites”, *Ceramics International*, Vol. 19, No. 4, pp. 251-257, 1993.
- [21]M. Hansen, *Constitution of Binary Alloys*, pp. 69. McGraw-Hill, New York, 1958.
- [22]E. Philofsky, “Intermetallic Formation in Gold-Aluminum Systems”, *Solid-State Electronics*, Vol. 13, pp. 1391-1399. Pergamon Press, Great Britain, 1970.
- [23]D. A. Parks and Tittmann, B. T., “Radiation Tolerance of Piezoelectric Bulk Single-Crystal Aluminum Nitride”, *IEEE Transactions on Ultrasonics, Ferroelectrics, and Frequency Control*, Vol. 61, No. 7, pp. 1216-1222, 2011.
- [24]R. Kažys, Voleišis, A., Šliteris, R., Voleišienė, B., Mažeika, L., and Abderrahim, H. A., “Research and development of radiation resistant ultrasonic sensors for quasi-image forming systems in a liquid lead-bismuth,” *Ultragarsas Journal*, Vol. 62, No. 3, pp. 7-15 2007.
- [25]M. Amini, Sinclair, T., and Coyle, T., “A new high temperature ultrasonic transducer for continuous inspection”, *IEEE Transactions on Ultrasonics, Ferroelectrics, and Frequency Control*, Vol. 63, No. 3, pp. 448-455, 2016.
- [26]M. Gomi, Oohira, N., Ozaki, K., and Koyano, M., “Photoluminescent and Structural Properties of Precipitated ZnO Fine Particles”, *Japanese Journal of Applied Physics*, Vol. 42, Part 1, No. 2A, pp. 481-485, 2003.
- [27]N. Hill and Waghmare, U., “First-principles study of strain-electronic interplay in ZnO: Stress and temperature dependence of the piezoelectric constants”, *Physical Review B*, Vol. 62, No. 13, pp. 8802-8810, 2000.

- [28]A. Dal Corso, Posternak, M., Resta, R., and Baldereschi, A., “*Ab initio* study of piezoelectricity and spontaneous polarization in ZnO”, *Physical Review B*, Vol. 50, No. 15, pp.10715-10721, 1994.
- [29]K. Trachenko, “Understanding resistance to amorphization by radiation damage”, *Journal of Physics: Condensed Matter*, Vol. 16, No. 49, pp. 1491-1515, 2004.
- [30]W. D. Callister and Rethwisch, D. G., *Materials science and engineering: an introduction*, Vol. 7, pp. 665-715, 2007.

Bibliography

- E. Aksel and Jones, J. L., "Advances in Lead-Free Piezoelectric Materials for Sensors and Actuators", *Sensors*, Vol. 10, pp. 1935-1954, 2010.
- M. Amini, Sinclair, T., and Coyle, T., "A new high temperature ultrasonic transducer for continuous inspection", *IEEE Transactions on Ultrasonics, Ferroelectrics, and Frequency Control*, Vol. 63, No. 3, pp. 448-455, 2016.
- W. D. Callister and Rethwisch, D. G., *Materials science and engineering: an introduction*, Vol. 7, pp. 665-715, 2007.
- F. K. Chang, Prosser, W. H., and Schulz, M. J., *Structural Health Monitoring*, Vol. 1, pp. 3-4, 2002.
- J. Chłopek, Błażewicz, S., and Powroźnik, A., "Mechanical properties of carbon-carbon composites", *Ceramics International*, Vol. 19, No. 4, pp. 251-257, 1993.
- A. Dal Corso, Posternak, M., Resta, R., and Baldereschi, A., "Ab initio study of piezoelectricity and spontaneous polarization in ZnO", *Physical Review B*, Vol. 50, No. 15, pp. 10715-10721, 1994.
- J. Daw, Tittmann, B., Reinhardt, B., Kohse, G., Ramuhalli, P., Montgomery, R., Chien, H.-T., Villard, J.-F., Palmer, J., and Rempe, J., "Irradiation Testing of Ultrasonic Transducers", *IEEE Transactions on Nuclear Science*, Vol. 61, No. 4, pp. 2279-2284, 2014.
- J. H. Edgar, Gu, Z., Taggart, K., Chaudhuri, J., Nyakiti, L., Lee, R. G., and Witt, R., "Oxidation of Aluminum Nitride for Defect Characterization", *Materials Research Society Symposium Proceedings*, Vol. 892, 2006.
- Y. Geng and Norton, M. G., "Early stages of oxidation for aluminum nitride", *Journal of Materials Research*, Vol. 14, No.7, pp. 2708-2711, 1999.
- V. Giurgiutiu, *Structural Health Monitoring*, Academic Press (Elsevier), Burlington, MA, 2008.
- M. Gomi, Oohira, N., Ozaki, K., and Koyano, M., "Photoluminescent and Structural Properties of Precipitated ZnO Fine Particles", *Japanese Journal of Applied Physics*, Vol. 42, Part 1, No. 2A, pp. 481-485, 2003.
- M. Hansen, *Constitution of Binary Alloys*, pp. 69. McGraw-Hill, New York, 1958.
- N. Hill and Waghmare, U., "First-principles study of strain-electronic interplay in ZnO: Stress and temperature dependence of the piezoelectric constants", *Physical Review B*, Vol. 62, No. 13, pp. 8802-8810, 2000.
- Y. Ito, Yasuda, K., Ishigami, R., Sasase, M., Hatori, S., Ohashi, K., Tanaka, S., and Yamamoto, A., "Radiation Damage of Materials Due to High Energy Ion Irradiation", *Nuclear Instruments and Methods in Physics Research*, Vol. 191, No. 1-4, pp. 530-535, 2002.

- R. Kažys, Voleišis, A., Šlitteris, R., Voleišienė, B., Mažeika, L., and Abderrahim., H. A., "Research and development of radiation resistant ultrasonic sensors for quasi-image forming systems in a liquid lead-bismuth," *Ultragarsas Journal*, Vol. 62, No. 3, pp. 7-15 2007.
- R. Kažys, Voleišis, A., and Voleišienė, B., "High temperature ultrasonic transducers: review", *Ultragarsas Journal*, Vol. 63, No. 2, pp. 7-17, 2008.
- J. Kim, Grisso, B. L., Kim, J. K., Ha, D. S., and Inman, D. J., "Electrical Modeling of Piezoelectric Ceramics for Analysis and Evaluation of Sensory Systems", *IEEE Sensor Applications Symposium*, pp. 122-127, 2008.
- J. H. Lee, Lee, M. R., Kim, J. T., Luk, V., and Jung Y. H., "A study of the characteristics of the acoustic emission signals for condition monitoring of check valves in nuclear power plants", *Nuclear Engineering and Design*, Vol. 236, No. 13, pp. 1411-1421, 2006.
- J. W. Lee, Radu, I., and Alexe, M., "Oxidation behavior of AlN substrate at low temperature", *Journal of Material Science: Materials in Electronics*, Vol. 13, pp. 131-137, 2002.
- R. Luo, Liu, T., Li, J., Zhang, H., Chen, Z., and Tian, G., "Thermophysical properties of carbon/carbon composites and physical mechanism of thermal expansion and thermal conductivity", *Carbon*, Vol. 42, No. 14, pp. 2887-2895, 2004.
- L. M. Manocha, "High performance carbon-carbon composites", *Sadhana*, Vol. 28, No. 1 & 2, pp. 349-358, 2003.
- K. L. McAughey, Burrows, S. E., Edwards, R. S., and Dixon, S., "Investigation into the use of Bismuth Titanate as a High Temperature Piezoelectric Transducer", *18th World Conference on Nondestructive Testing*, 2012.
- A. O. Niedermayer, Voglhuber-Brunnmaier, T., Sell, J., and Jakoby, B., "Methods for the robust measurement of the resonant frequency and quality factor of significantly damped resonating devices", *Measurement Science and Technology*, Vol. 23, No. 8, pp. 1-11, 2012.
- D. A. Parks and Tittmann, B. T., "Radiation Tolerance of Piezoelectric Bulk Single-Crystal Aluminum Nitride", *IEEE Transactions on Ultrasonics, Ferroelectrics, and Frequency Control*, Vol. 61, No. 7, pp. 1216-1222, 2011.
- D. A. Parks, Tittmann, B. T., and Kropf M. M., "Aluminum Nitride as a High Temperature Transducer", *AIP Conference Proceedings*, Vol. 1211, pp. 1029-1034, 2010.
- D. A. Parks, Zhang, S., and Tittmann, B. T., "High-Temperature (>500 °C) Ultrasonic Transducers: An Experimental Comparison Among Three Candidate Piezoelectric Materials", *IEEE Transactions on Ultrasonics, Ferroelectrics, and Frequency Control*, Vol. 60, No. 5, pp. 1010-1015, 2013.

- D. Parks, "Development of a Piezoelectric Ultrasonic Array Sensor for Nuclear Reactor Applications", Ph.D. Dissertation, Pennsylvania State University, 2012.
- K. K. Phani, Sanyal, D., and Sengupta, A. K., "Estimation of elastic properties of nuclear fuel material using longitudinal ultrasonic velocity – A new approach", *Journal of Nuclear Materials*, Vol. 366, No. 1-2, pp. 129-136, 2007.
- E. Philofsky, "Intermetallic Formation in Gold-Aluminum Systems", *Solid-State Electronics*, Vol. 13, pp. 1391-1399. Pergamon Press, Great Britain, 1970.
- B. Reinhardt, Tittmann, B., and Suprock, A., "Nuclear Radiation Tolerance of Single Crystal Aluminum Nitride Ultrasonic Transducer", *International Congress on Ultrasonics: Physics Procedia*, Vol. 70, pp. 609-613, 2015.
- J. L. Rempe, Knudson, D. L., Daw, J. E., Condie, K. G., and Curtis Wilkins, S., "New Sensors for In-Pile Temperature Measurement at the Advanced Test Reactor National Scientific User Facility", *Nuclear Technology*, Vol.175, No. 3, pp. 681-691, 2011.
- H. S. Shulman, Testorf, M., Damjanovic, D., and Setter, N., "Microstructure, Electrical Conductivity, and Piezoelectric Properties of Bismuth Titanate", *Journal of the American Ceramic Society*, Vol. 79, No.12, pp. 3124-3128, 1996.
- T. Takenaka, and Nagata, H., "Sodium Bismuth Titanate-Based Ceramics", *Lead Free Piezoelectrics*, pp. 255-290, 2012.
- K. Trachenko, "Understanding resistance to amorphization by radiation damage", *Journal of Physics: Condensed Matter*, Vol. 16, No. 49, pp. 1491-1515, 2004.
- J. F. Villard and Schyns, M., "Innovations for in-pile measurements in the framework of the CEA-SCK·CEN Joint Instrumentation Laboratory", *Advancements in Nuclear Instrumentation Measurement Methods and their Applications (ANIMMA) Proceedings*, pp. 1-8, 2009.
- T. Windhorst and Blount, G., "Carbon-carbon composites: a summary of recent developments and applications", *Materials & Design*, Vol. 18, No. 1, pp. 11-15, 1997.
- T. Yano, Inokochi, K., Shikama, M., Ukai, J., Onose, S., and Maruyama, T., "Neutron irradiation effects on isotope tailored aluminum nitride ceramics by a fast reactor up to 2×10^{26} ", *Journal of Nuclear Materials*, Vol. 329-333, Part B, pp. 1471-1475, 2004.
- "About NDT." *NDT Resource Center*. NDE Education, n.d. (<https://www.nde-ed.org/AboutNDT/aboutndt.htm>)
- "An Introduction to Transducer Crystals." *Piezoelectric Components*. Boston Piezo-Optics, n.d. (<http://www.bostonpiezooptics.com/intro-to-transducer-crystals>)
- "Fundamentals of Piezo Technology." *Technology // Fundamentals*. PI Ceramic, n.d. (<http://www.piceramic.com/piezo-technology/fundamentals.html>)

“Limitations of Piezo Ceramic Materials.” *Technical Ceramics*. Morgan Advanced Materials, n.d. (<http://www.morgantechnicalceramics.com/products/product-groups/piezo-ceramic-components/piezo-ceramic-tutorials/limitations>)

“Piezoelectric Effect.” *PC Control Learning Zone*. Pc-control.co.uk, n.d. (http://www.pc-control.co.uk/piezoelectric_effect.htm)

“Piezoelectric Principle.” *Metra Mess- Und Frequenztechnik in Radebeul E.K.* Manfred Weber, n.d. (http://www.new.mmf.de/piezoelectric_principle.htm)